Universitá degli Studi di Napoli Federico II

Study of the $pp \rightarrow Z + \text{jets} \rightarrow \mu^+\mu^- + \text{jets}$ channel with the CMS detector at LHC

Facoltá di scienze MM.FF.NN.
Corso di Laurea Magistrale in Fisica
Tesi di Laurea Magistrale
A.A. 2007/2008

Relatori:
Ch.mo Prof. C. Sciacca
Dott. L. Lista

Studente:
Alberto Orso Maria Iorio
Matricola 358/026

"Considerate la vostra semenza:
fatti non foste a viver come bruti,
ma per seguir virtute e canoscenza"
Dante Alighieri, Inferno XXVI 118-120

Contents

Introduction

The present thesis is a study of the production of the Z boson in association with jets at the CMS(Compact Muon Solenoid) experiment, focusing on processes where the Z decays in a muon-antimuon pair. The CMS experiment will collect collision data produced at the LHC (Large Hadron Collider) machine, built at CERN (Centre Europeen pour la Rescherche Nucleaire). The LHC is a proton-proton collider designed to accelerate proton beams up to an energy $\sim$ 7 TeV per beam, resulting in a maximum energy in the center of mass available for $p-p$ interactions of $\sqrt{s} = 14$ TeV. The scheduled full regime luminosity at LHC is $\mathcal{L} = 10^{34}\mathrm{cm}^{-2}\mathrm{s}^{-1}$. Both the center of mass energy and luminosity at LHC are unparalleled in history of particle accelerators. The purposes for LHC are the study of Standard Model and the search for new physics at the TeV energy scale.

Standard Model of electroweak interactions is in excellent agreement with the experimental results up to the energy scales experimentally accessible up to now. Direct experimental evidence has been found for all elementary particles predicted by Standard Model, except for the predicted Higgs Boson, which plays a crucial role for the generation of particles masses. LHC will verify the validity of Standard Model with the search for the Higgs boson and with the test of Standard Model predictions for the physics of elementary particles at the TeV scale.

Several theories of physics beyond Standard Model predict the existence of new particles whose mass will be in the reach of LHC.

Given the large energy available in the center of mass, the LHC will generate a great abundance of Z particles: the inclusive cross section for Z production in the $\mu^+\mu^-$ channel is ≈ 1.7 nb, which means that at full luminosity about 170 millions Z decaying into muon-antimuon pairs will be produced in a year of data taking. The provided statistics will therefore be sufficient to separately study the exclusive $Z(\mu^+\mu^-) + n$ jets processes. The study of the $Z+$ jets channel is of great interest for several reasons:

- The cross section for Z production channels is known from the theory, therefore cross section measurements, in particular in the $Z + 0$ jets channel, can be used to control the difference between nominal and effective luminosity of the machine.

- The measurement of Standard Model strong coupling constant at the TeV energy scale can be made by comparing the cross section of channels with different number of jets.

- Many new physics signatures contain a lepton pair in the final state associated with jet production, therefore $Z+$ jets processes provide an important background for such events.

In this thesis a systematic analysis of $Z + n$ jets exclusive channels is performed on a sample of fully simulated data. A study of muons and jets kinematic variables was performed in order to provide a signal selection with a good background rejection. A background subtraction procedure was then developed and applied in order to estimate the number of signal events in the different channels. This subtraction method is data-driven, in the sense that it does not rely on informations taken from Monte Carlo and can be performed directly on data. The number of events can be used to estimate the cross section of the processes. A study is also performed using informations from Monte Carlo to associate the jets observed in the detector with the gluons and quarks in the elementary processes. Chapter 1 offers a review of the theoretical framework of the Standard Model .
Chapter 2 gives an overview on the LHC machine and describes the CMS detector in the detail.
In Chapter 3 the physics program at LHC is presented and a brief review of physics channels of interest is given.
Chapter 4 treats the Monte Carlo tools used to simulate data and the reconstruction algorithms implemented at CMS.
In Chapter 5 the analysis performed on simulated data is described, and the results of the work are shown.
The present thesis work provides a preliminary study on simulated data for the measurement of $Z+$ jets cross section, and it can be performed on the early data taken at CMS after the LHC startup.

Chapter 1

The Standard model

The purpose of particle physics is to identify the fundamental components matter and to understand the interactions between them. The most accurate model that describes particle physics is known as the Standard Model. The Standard Model is a quantum field theory that treats both matter and force fields with the same formalism, since interactions are themselves regarded as mediated by particles.
Fundamental matter particles in Standard Model are categorized as either quarks or leptons, which are grouped in three generations each. A generation (or family) is a doublet of particles associated to an isospin quantum number. All quark generations contain a particle with +2/3 charge and a particle with charge −1/3, while lepton generations include a particle with charge −1 (e.g. the electron) and a neutral particle, named neutrino.
The quantum numbers of all quarks and leptons are listed in table 1. The Standard Model describes three fundamental interactions: electromagnetic, weak and strong interaction. Each interaction is associated to a boson multiplet, whose components are referred to as mediators for the interaction, and to an absolutely conserved quantum number, which is the charge in the case of electromagnetism. Mediator bosons are listed in table 1. The dynamics equations for the Standard Model are obtained from a gauge principle[1]: the

Table 1.1: Fermion quantum numbers

Particles				Spin	Charge
Leptons	$\binom{\nu_e}{e^-}$	$\binom{\nu_\mu}{\mu^-}$	$\binom{\nu_\tau}{\tau^-}$	1/2	0 -1
Quarks	$\binom{u}{d}$	$\binom{c}{s}$	$\binom{t}{b}$	1/2	$\frac{2}{3}$ $-\frac{1}{3}$

Table 1.2: Mediator bosons and fundamental interactions

Interaction	Particles	Spin	Charge
Electromagnetic	γ	1	0
Weak	W^+, W^-, Z^0	1	1, -1, 0
Strong	8 gluons	1	0

free particle Lagrangian is requested to be invariant under a local (gauge) transformation from the symmetry group:

$$SU(3)_{col} \otimes SU(2)_{is} \otimes U(1)_y. \tag{1.1}$$

The number of the mediator bosons for an interaction is determined by the symmetry group associated with it. The $SU(3)_{col}$ group is the symmetry that generates the strong interaction. Its conserved quantum number is the color, which is the equivalent of electromagnetic charge for strong interactions, with the difference that three possible colors are present. Strong interaction is mediated by an octet of vector bosons, the gluons. Those gluons are colored particles themselves, while the photon, for instance, doesn't carry electromagnetic charge.

The $SU(2)_{is} \otimes U(1)_y$ group is the symmetry that generates both the Electromagnetic and Weak interactions into an unified theory known as the Glashow-Salam-Weinberg model[2][3][4]. The mediators generated by this symmetry are the vector bosons $W^{\pm}, Z$ and γ. It is noteworthy that while the photon is massless, all mediators from weak interactions are massive particles.

In order to produce a mass term for $W^{\pm}$ and Z that does not destroy the gauge invariance for the Standard Model Lagrangian, the spontaneous symmetry breaking mechanism is introduced. This mechanism predicts the presence of a scalar particle, the Higgs boson[15], whose couplings with the vector bosons allow the presence of the required mass term. At present state, no experimental evidence of the Higgs boson has been found, and its discovery is one of the main tasks experimental physics has to accomplish.

1.1 The Quantum Electrodynamics

The Quantum Electrodynamics is the simplest example of a realistic quantum field theory obtained from the imposition of a gauge invariance. The symmetry group involved in this case is U (1).

The Lagrangian density for the Dirac equation describing a spin 1/2 fermion can be written as:

$$\mathcal{L}_D = i\bar{\psi}\gamma^\mu\partial_\mu\psi - m\bar{\psi}\psi, \tag{1.2}$$

which comprises a kinetic term and a mass term, where m is the fermion mass, γ^μ are the Dirac gamma matrices and $\psi(\bar{\psi})$ is the spinor field for the fermions (its adjoint), namely:

$$\psi = \begin{pmatrix} \psi_R \\ \psi_L \end{pmatrix}. \tag{1.3}$$

The kinematic Lagrangian term for a photon is introduced as:

$$\mathcal{L}_\gamma = -\frac{1}{4}F^{\mu\nu}F_{\mu\nu}, \tag{1.4}$$

where $F^{\mu\nu}$ is the tensor field:

$$F_{\mu\nu} = \partial_\mu A_\nu - \partial_\nu A_\mu \tag{1.5}$$

and A_μ is the 4-vector electromagnetic field. So, the free (non interacting) Lagrangian for a fermion field and an electromagnetic field is:

$$\mathcal{L}_D + \mathcal{L}_\gamma = i\bar{\psi}\gamma^\mu\partial_\mu\psi - m\bar{\psi} - \frac{1}{4}F^{\mu\nu}F_{\mu\nu}. \tag{1.6}$$

The dynamics equations obtained from 1.6 do not couple the fermion field ψ and the electromagnetic field A_μ, so that an additional interaction term is needed in which both the fermion and the photon fields are involved. This term is obtained using a gauge invariance principle. As a first step, one can notice that the Lagrangian of (1.6) is invariant under a global U (1) gauge transformation,

$$\psi \to \psi' = e^{i\theta}\psi, \tag{1.7}$$

where θ is a real constant number. However the invariance does not extend to local U (1) transformations of the type:

$$\psi \to \psi' = e^{i\theta(x)}\psi, \tag{1.8}$$

where $\theta(x)$ has now a dependance from the space-time point. The gauge principle consists in imposing this local U (1) invariance. The covariant derivative operator is defined:

$$D_\mu = \partial_\mu + iqA_\mu, \tag{1.9}$$

where A_μ has the following transformation rule:

$$A_\mu \rightarrow A'_\mu = A_\mu - \frac{1}{q}\partial_\mu \theta. \tag{1.10}$$

By replacing the usual derivative operator with the covariant derivative in 1.6 one obtains the Quantum Electrodynamics (QED) Lagrangian:

$$\mathcal{L}_{QED} = i\bar{\psi}\gamma^\mu \partial_\mu \psi - m\bar{\psi} - \frac{1}{4}F^{\mu\nu}F_{\mu\nu} - q\bar{\psi}\gamma^\mu A_\mu \psi. \tag{1.11}$$

The additional term that represents the electromagnetic interaction is:

$$\mathcal{L}_{int} = -q\bar{\psi}\gamma^\mu \psi A_\mu \equiv -J^\mu A_\mu \tag{1.12}$$

where q is the charge of the particle and represents the strength of the coupling. The quantity J^μ is interpreted as the charge current, that is the probability current of the particle multiplied by its charge. The interaction term is then used to obtain the amplitude for all electromagnetic processes; it is also possible define a diagram for any electromagnetic process that is associated with its amplitude. Those diagrams are also known as Feynman diagrams.

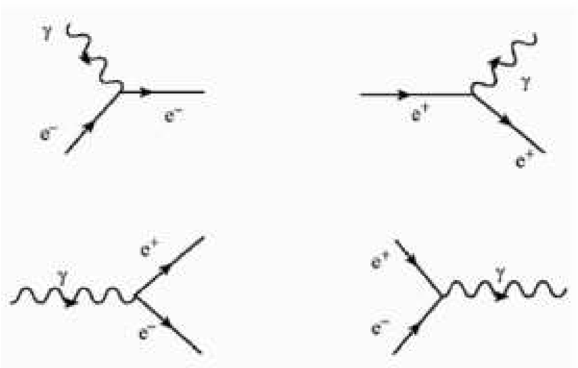

Figure 1.1: Feynman graphs for electromagnetic vertices

1.2 The ElectroWeak theory

1.2.1 The GSW model

The relevant symmetry group for Weak interactions is $SU(2)_L$, where the "L" subscript means that only the left-handed chiral components of the fields are involved in the interaction. The choice of this group is suggested by the kind of transitions this interaction produces: six families (doublets) of weak isospin can be identified and weak interactions produce a transition between the members of those doublets. Since the fundamental representation of SU (2) is generated by Pauli matrices, it is possible to adopt the usual formalism of the angular momentum for weak isospin. By naming t the weak isospin quantum number and t_3 its observed component one can define:

$$\begin{array}{l} t_3 = +1/2 \\ t_3 = -1/2 \end{array} \qquad \begin{pmatrix} \nu_e \\ e^- \end{pmatrix}_L \qquad \begin{pmatrix} \nu_\mu \\ \mu^- \end{pmatrix}_L \qquad \begin{pmatrix} \nu_\tau \\ \tau^- \end{pmatrix}_L \tag{1.13}$$

for lepton pairs, and:

$$\begin{array}{l} t_3 = +1/2 \\ t_3 = -1/2 \end{array} \qquad \begin{pmatrix} u \\ d' \end{pmatrix}_L \qquad \begin{pmatrix} c \\ s' \end{pmatrix}_L \qquad \begin{pmatrix} t \\ b' \end{pmatrix}_L \tag{1.14}$$

for quark pairs, where the d', s' and b' quarks are quantum mechanical superpositions of d,s and b which are classified by their strong quantum numbers[1]. A local $SU(2)_L$ transformation acting on the isospin doublets will therefore take the form:

$$\begin{pmatrix} \nu_e \\ e^- \end{pmatrix}_L' = e^{-\frac{i}{2}\vec{\alpha}(x)\cdot\vec{\tau}} \begin{pmatrix} \nu_e \\ e^- \end{pmatrix} \tag{1.15}$$

where $\vec{\tau}$ the vector of Pauli matrices and $\vec{\alpha}\ (x)$ is a vector of three real parameters and it depends from the space-time point. The right-handed chiral component of the particles does not enter the interaction, so it has the properties of an $SU(2)_L$ singlet. By imposing the gauge invariance one can obtain three vector fields: two of them correspond to charged bosons named $W^{\pm}$, while the third corresponds to a neutral boson named W^0. This model for weak interactions is then expanded by successfully unifying both weak and electromagnetic interactions within a common quantum field theory. In the Standard Model the relevant symmetry group for electroweak interactions is therefore:

$$SU(2)_L \otimes U(1)_Y \tag{1.16}$$

---

[1] The matrix of coefficients that decompose d, s, b in terms of s', s', b' is called Cabibbo-Kobayashi-Maskawa (CKM) matrix[13][14]

This symmetry group therefore requires the presence of 3 + 1 gauge fields. The relevant quantum numbers, and the conserved quantities of the interaction are the hypercharge y and the weak isospin T. The following relation allows to define the electromagnetic charge of a particle from the electroweak quantum numbers:

$$eQ = e(t_3 + y/2) \tag{1.17}$$

where t_3 is the third component of weak isospin. The covariant derivative operator that makes the free lagrangian invariant under an $SU(2)_L \otimes U(1)_Y$ transformation takes the following form:

$$D_\mu = \partial_\mu + ig\frac{\overrightarrow{\tau}}{2} \cdot W_\mu + ig'yB_\mu \tag{1.18}$$

The mass terms for fermions and bosons will be discussed later in this chapter. Not considering the mass terms for now, the Lagrangian for electroweak interactions will include a Dirac term for the fermions modified with the covariant derivative:

$$\mathcal{L}_{fermions} = \sum_f \bar{\psi}\gamma^\mu D_\mu \psi, \tag{1.19}$$

and a gauge term for the boson fields

$$\mathcal{L}_{gauge} = -\frac{1}{4}W_i^{\mu\nu}W^i_{\mu\nu} - \frac{1}{4}B^{\mu\nu}B_{\mu\nu}, \tag{1.20}$$

where $W^i_{\mu\nu}$, $B_{\mu\nu}$ are the tensor fields:

$$\begin{aligned} B_{\mu\nu} &= \partial_\mu B_\nu - \partial_\nu B_\mu, \\ W^i_{\mu\nu} &= \partial_\mu W^i_\nu - \partial_\nu W^i_\mu, \end{aligned} \tag{1.21}$$

and W_μ is a three component vector field. The complete Lagrangian for the electroweak processes will therefore be:

$$\begin{aligned} \mathcal{L}_{EW} =& - i\psi_L(\partial_\mu + ig\frac{\overrightarrow{\tau}}{2} \cdot W_\mu + ig'yB_\mu)\psi_L + \\ & - i\psi_R(\partial_\mu + ig'yB_\mu)\psi_R + \\ & - \frac{1}{4}W_i^{\mu\nu}W^i_{\mu\nu} - \frac{1}{4}B^{\mu\nu}B_{\mu\nu}, + \mathcal{L}_{WWV} + \mathcal{L}_{WWVV} \end{aligned} \tag{1.22}$$

where ψ_L and ψ_R are the left and right handed chiral components of the particles, and the $\mathcal{L}_{WWV}$, $\mathcal{L}_{WWVV}$ terms describe the three- and four- point self interactions of the vector bosons[12] that arise because of the non-Abelian nature of the SU(2) group.

The four gauge fields can be combined to produce the physical vector fields for $W^{\pm}$, Z and photon:

$$W^{\pm}_{\mu} = \frac{1}{\sqrt{2}}(W^1_{\mu} \mp W^2_{\mu}) \tag{1.23}$$

$$Z_{\mu} = \cos\theta_w W^3_{\mu} - \sin\theta_w B_{\mu} \tag{1.24}$$

$$A_{\mu} = \cos\theta_w B_{\mu} + \sin\theta_w W^3_{\mu} \tag{1.25}$$

where θ_w is the Weinberg angle defined as:

$$\cos\theta_w = \frac{g}{\sqrt{g^2 + g'^2}}, \text{ and } \sin\theta_w = \frac{g'}{\sqrt{g^2 + g'^2}}. \tag{1.26}$$

The electromagnetic charge is now:

$$q = g' \cos\theta_w = g \sin\theta_w. \tag{1.27}$$

1.2.2 The Higgs mechanism

The gauge principle allows to successfully describe the interactions between particles; however, all fields produced by imposing the gauge invariance are strictly massless. A mass term of the form $mA_{\mu}A^{\mu}$ for a boson field is not invariant under an $SU(2) \otimes U(1)$ transformation, nevertheless it is established that the vector bosons $W^{\pm}$, Z have a consistently non zero mass, which gives weak interactions their short-range characteristics. $W^{\pm}$, Z mass has been measured in 1983 thanks to the UA1 and UA2 collaborations[11] It is therefore necessary to introduce a new term that coherently represents the masses of the particles, while at the same time it must preserve the gauge principle. The spontaneous symmetry breaking mechanism allows to generate such terms by postulating the existence of a new scalar particle: the Higgs[16] boson. The Higgs boson field is written as a SU (2) doublet with two scalar components:

$$\Phi = \begin{pmatrix} \phi^+ \\ \phi^0 \end{pmatrix} = \begin{pmatrix} \phi_1 + i\phi_1 \\ \phi_3 + i\phi_4 \end{pmatrix}. \tag{1.28}$$

The Lagrangian for such boson includes a potential which is responsible of the symmetry breaking mechanism:

$$\mathcal{L}_H = (D^{\mu}\Phi)^{\dagger} D_{\mu}\Phi - V(\Phi) = (D^{\mu}\Phi)^{\dagger} D_{\mu}\Phi - \mu^2 \Phi^{\dagger}\Phi - \lambda(\Phi^{\dagger}\Phi)^2. \tag{1.29}$$

By requiring that $\mu^2 < 0$ and $\lambda > 0$, the minimum of the potential is not unique anymore, but its located on a continuous ring on a complex plane (Figure 1.2).

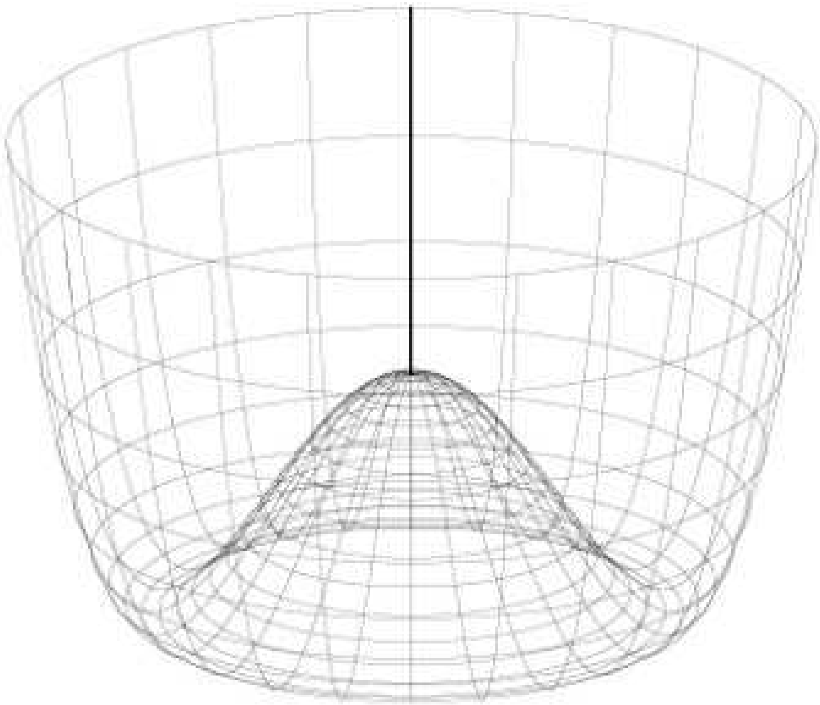

Figure 1.2: Higgs potential described from the last two terms of Equation 1.29 with $\mu^2 < 0$ and$\lambda > 0$. The potential minimum is located on a continuous ring.

There is therefore a degree of freedom for the choice of higgs vacuum state. It can also be written so that only one of its components is non-zero:

$$\Phi = \begin{pmatrix} 0 \\ v + h(x) \end{pmatrix}, \tag{1.30}$$

where

$$v = \sqrt{-\mu^2/\lambda}. \tag{1.31}$$

In an $SU(2)\otimes U(1)$ theory the kinetic term of Higgs Lagrangian can therefore be written by imposing the form of the covariant derivative from 1.18, namely:

$$D_\mu = \partial_\mu + ig\frac{\vec{\tau}}{2} \cdot W_\mu + ig'yB_\mu.$$

So one obtains:

$$\begin{aligned}(D^\mu\Phi)^\dagger D_\mu\Phi = &\frac{1}{2}\partial_\mu h\partial^\mu h + \\ &\frac{1}{8}(v+h)^2 g^2 (W^1_\mu + iW^2_\mu)(W^{1\mu} - iW^{2\mu}) + \\ &\frac{1}{8}(v+h)^2 (g'B_\mu - gW^3_\mu)(g'B^\mu - gW^{3\mu})\end{aligned} \tag{1.32}$$

The Lagrangian of the sector consisting of the gauge fields and the Higgs is:

$$\begin{aligned}&\mathcal{L}_{G\Phi} = \mathcal{L}_{gauge} + \mathcal{L}_H = (D^\mu\Phi)^\dagger D_\mu\Phi - V(\Phi) = \\ &(D^\mu\Phi)^\dagger D_\mu\Phi - \mu^2\Phi^\dagger\Phi - \lambda(\Phi^\dagger\Phi)^2 - \frac{1}{4}W^{\mu\nu}_i W^i_{\mu\nu} - \frac{1}{4}B^{\mu\nu}B_{\mu\nu}\end{aligned} \tag{1.33}$$

Switching to the physical Z and A fields from (1.24), (1.25) and keeping only the quadratic terms, (1.33) can be written as:

$$\begin{aligned}
\mathcal{L}_{G\Phi} = &\frac{1}{2}\partial_\mu h\partial^\mu h - \mu^2 h^2 \tag{1.34}\\
&-\frac{1}{4}(\partial_\mu W_{1\nu} - \partial_\nu W_{1\mu})(\partial_\mu W^\nu_1 - \partial_\nu W^\mu_1) + \frac{1}{8}g^2v^2W_{1\nu}W^\nu_1 \tag{1.35}\\
&-\frac{1}{4}(\partial_\mu W_{2\nu} - \partial_\nu W_{2\mu})(\partial_\mu W^\nu_2 - \partial_\nu W^\mu_2) + \frac{1}{8}g^2v^2W_{2\nu}W^\nu_2 \tag{1.36}\\
&-\frac{1}{4}(\partial_\mu Z_\nu - \partial_\nu Z_\mu)(\partial_\mu Z^\nu - \partial_\nu Z^\mu) + \frac{1}{8}(g^2 + g'^2)v^2 Z?\nu Z^\nu \tag{1.37}\\
&-\frac{1}{4}F^{\mu\nu}F_{\mu\nu} \tag{1.38}
\end{aligned}$$

where (1.38) is the tensor field for the photon as in (1.5) the second term in (1.35) and (1.35) has exactly the form of a mass term for the $W_{1,2}$ fields and one therefore can define the w mass as:

$$m_W = \frac{1}{2} g v, \tag{1.39}$$

while the second term from (1.37) is the a mass term for the Z, so that:

$$m_Z = \frac{1}{2} v \sqrt{g^2 + g'^2} = \frac{m_W}{\cos\theta_w} \tag{1.40}$$

The Higgs terms not included in (1.33) represent the interaction terms between the Higgs boson and the W and Z.

1.2.3 The fermion masses

The Fermion mass term, $-m\bar{\psi}\psi$, first introduced in 1.2 can be written in terms of left and right-handed spinors, i.e. for the electron,

$$m_e \bar{\psi}_e \psi_e = m_e(\bar{e}_R e_L + \bar{e}_L e_R). \tag{1.41}$$

However, this term is not gauge invariant because e_L is a component of an SU (2) doublet while e_R is an SU (2) singlet. It is possible to produce a gauge invariant mass term by introducing a Yukawa coupling between the fermions and the higgs field:

$$\mathcal{L}_Y = g_f(\bar{\psi}_L \Phi \psi_R - \bar{\psi}_R \Phi^\dagger \psi_L), \tag{1.42}$$

where ψ_L and ψ_R are the left SU (2) doublet and the right SU (2) singlet, g_f is the Yukawa coupling constant and at $\Phi = \Phi^0$ 1.42 becomes (i.e. for leptons):

$$\mathcal{L}_{Hf} = \frac{g_f}{\sqrt{2}} \left[(\,\nu_l \; l_L\,) \begin{pmatrix} 0 \\ v+h \end{pmatrix} l_R + l_R (\,0 \;\; v+h\,) \begin{pmatrix} \nu_l \\ l_L \end{pmatrix} \right] \tag{1.43}$$

$$= \frac{g_f}{\sqrt{2}} (v+h)(l_L l_R + l_R l_L), \tag{1.44}$$

so that the constant coefficient of $(l_L l_R + l_R l_L)$ from 1.44 is:

$$m_f = \frac{g_f \cdot v}{\sqrt{2}}. \tag{1.45}$$

The mass term for the up components of the SU (2) doublets is obtained by using the adjoint field of Φ:

$$\tilde{\Phi} = \frac{1}{\sqrt{2}} \begin{pmatrix} v+h \\ 0 \end{pmatrix}, \tag{1.46}$$

thus the coupling Lagrangian becomes:

$$\mathcal{L}_{Hf} = \frac{g_f}{\sqrt{2}} \left[\left(u_{i,L},\ d_{i,L} \right) \begin{pmatrix} v+h \\ 0 \end{pmatrix} u_{i,R} + u_{i,R} \left(v+h,\ 0 \right) \begin{pmatrix} u_{i,L} \\ d_{i,L} \end{pmatrix} \right] \tag{1.47}$$

$$= \frac{g_f}{\sqrt{2}} (v+h)(u_{i,L} u_{i,R} + u_{i,R} u_{i,L}), \tag{1.48}$$

where $u_i = (u, c, t)$ and $u_i = (d, s, b)$ and the mass term has the same form as in (1.45). Even if this kind of Yukawa coupling solves the problem of fermions' masses, it does not arise from a gauge principle and it is purely phenomenological. In order for it to be justified an important step would be the discovery of the Higgs boson and the measurement of its branching fractions.

1.3 Quantum Chromodynamics

Quantum Chromodynamics (QCD)[20] is the theory of strong interactions. As for electromagnetic and weak interactions it is formulated thanks to the imposition of a gauge principle, with the difference that now the symmetry group is $SU(3)_C$, where the C subscript refers to a new degree of freedom called color. Strong interactions only involve quarks, which are present in three color eigenstates. The free quark lagrangian is now:

$$\mathcal{L}_{Free} = \bar{\psi}_\alpha \gamma_\mu \partial^\mu \psi_\alpha - m \bar{\psi}_j \psi_j, \tag{1.49}$$

where $\alpha = 1,\ 2,\ 3$ (B, R, G) is the color index. The SU (3) transformation takes the form:

$$\psi \rightarrow \psi' = e^{-\frac{i}{2} g_s \theta_a(x) \lambda_a} \psi, \tag{1.50}$$

where λ_a are the eight Gell Mann matrices and are the generators of SU (3), $g_s = \sqrt{4\pi\alpha_s}$, and α_s is the coupling constant for strong interactions.
Their commutation rules are:

$$\left[\frac{\lambda_a}{2}, \frac{\lambda_b}{2} \right] = i f_{abc} \frac{\lambda_c}{2} \tag{1.51}$$

where f_{abc} are the structure constants of the groups and the indices run from 1 to 8. Gauge invariance under the 1.50 requires a covariant derivative such as:

$$D_\mu = \partial_\mu + i \frac{g_s}{2} \lambda_a G^a_\mu, \tag{1.52}$$

where G^a_μ are the 8 gluon fields that transform as:

$$G^a_\mu \rightarrow G'^a_\mu = G^a_\mu + \partial_\mu + i g_s f^{abc} \theta_b(x) G_{\mu,c} \tag{1.53}$$

The complete QCD Lagrangian then becomes:

$$\mathcal{L}_{QCD} = \bar{\psi}\gamma^{\mu}\partial_{\mu}\psi - m\bar{\psi}\psi - ig_s\bar{\psi}\gamma^{\mu}\lambda_a\psi G^b_{\mu} - \frac{1}{4}G^{\mu\nu}_a G^a_{\mu\nu} \tag{1.54}$$

with $G^{\mu\nu}_a$ the gluon tensor field defined as:

$$G^a_{\mu\nu} = \partial_{\mu}G^a_{\nu} - \partial_{\nu}G^a_{\mu} - g_s f^{abc}G_{\mu,b}G_{\nu,c} \tag{1.55}$$

The last term in (1.55) is quadratic in the gluon fields and produces a self-interaction between the gluon fields. Such a term does not arise in QED and is due to the non-Abelian character of the SU (3) symmetry group

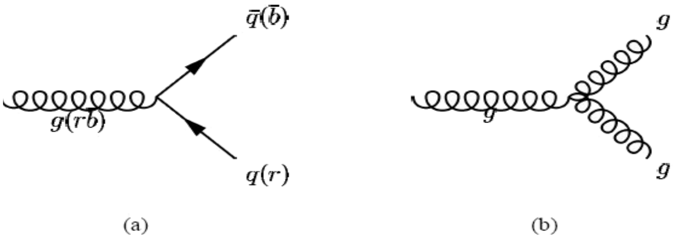

(a)

(b)

Figure 1.3: Example diagrams of strong interaction showing production of a quark-antiquark pair from a gluon(a) and gluon self coupling(b).

Asymptotic freedom and color confinement

Quantum Chromodynamics as the theory for strong interactions has to explain its fundamental characteristics.

Strong force is responsible for the inter-quark interactions that bind them together, forming hadrons. However, no color multiplicity of mass degenerate hadrons is observed, so stable states can only be color singlets. This property is known as color confinement. The study of bound states in QCD presents several difficulties, due to the strength of the coupling that makes a perturbative approach to calculations impossible. Still all experimental results show that, for sufficiently high energy processes, quarks inside protons behave as free particles. This property is known as asymptotic freedom and it can be qualitatively explained thanks to the renormalization of QCD theory [17]. The renormalization process starts from the fact that the physical coupling constant is not actually the g_s that appears in the lagrangian, but the real parameter takes into the account all the loop corrections of the theory at any perturbative order. This happens because in nature particles are cannot be separated from interactions even when they are propagating in the void, meaning that the physic Lagrangian is the one that includes the interaction terms. Thus a particle at any space-time point produces virtual couples that modify the charge distribution around the particle itself. This causes the actual coupling constant in any process to assume a dependance from the transferred 4-momentum q:

$$\alpha_s(|q^2|) = \frac{\alpha_s(\mu^2)}{[1 + \alpha_s(\mu^2)\frac{(33-2N_f)}{12\pi}ln(|q^2|/\mu^2)]} \tag{1.56}$$

where $N_f = 6$ is the number of fermions capable of strong interactions (6 quarks) and μ is a scale parameter for the strength of the coupling. So, the value of the coupling constant decreases as the transferred 4-momentum increases, making it possible to apply perturbative calculation. Equivalently, α_s is a growing function of the distance between the two interacting particles, and the critical value set by the μ scale is approximately 1 fm, which is also the proton radius. This result shows that QCD is consistent with the fact that no calculation can be made at perturbative level for hadronic states[18]; on the other hand, progresses have been made for studies of bound states thanks to Lattice Field Theories.

1.4 The quark-parton model

It is possible to realize a model of the internal structure of a nucleon as an incoherent superposition of quarks and gluons, called partons. Each parton carries a fraction x of the nucleon momentum, and the probability distributions of this variable is called Parton Distribution Function (PDF). Those functions are determined thanks to inelastic scattering experiments of nucleon-electron

and nucleon-neutrino. PDFs of u and d quarks have a valence contribution, due to quarks in the bound state, and a sea contribution, due to virtual $\bar{q}q$ pairs. Other quarks, as well as gluons and anti-quarks have only the sea contribution.
PDFs depend from the transferred momentum Q^2: their values tend to be shifted at low values of x as Q^2 increases.

1.4.1 The Drell-Yan process

The quark-parton model allows to interpret processes involving nucleons in terms of fundamental processes between their point-like components. Considering only the photon exchange contribution in the s channel, the Drell-Yan[19] process is:

$$PP \to \mu^+\mu^- + X \tag{1.57}$$

One can see this process as the interaction between partons, took in any combination of momentum and flavor. The cross section for the fundamental electrodynamics scattering $\bar{q}q \to \mu^+\mu^-$ is

$$\hat{\sigma}_{\bar{q}q\to\mu^+\mu^-} = \frac{4\pi\alpha^2 e_q^2}{3q^2}, \tag{1.58}$$

where $q^2 = q^\mu q_\mu$ and q^μ is the transferred 4-momentum. Considering every possible combination of momenta x_1 and x_2 one has:

$$\sigma_{pp\to\mu^+\mu^-} = \frac{4\pi\alpha^2}{9q^2}\sum_q \int e_q^2(f_q(x_1)\bar{f}_q(x_2) + \bar{f}_q(x_1)f_q(x_2))dx_1 dx_2 \tag{1.59}$$

where $\bar{f}_a(x)$ is the anti-particle PDF. However, since particles PDFs are color-independent, the initial state includes 9 possible combinations of quarks colors, of which only the three color-anticolor combinations can annihilate. So, a factor 3/9 has been introduced to take color into account[2]. This cross section is correct for a purely electrodynamic process, in which only a photon can be exchanged. This happens to become a realistic case when the center of mass energy is low enough that the Z boson exchange can be neglected. Actual Drell-Yan processes at high energies ($\gtrsim m_Z c^2$) happen through the exchange of a virtual photon γ or a Z boson. The differential cross section for the elementary (parton-parton) process, including the Z term, becomes:

$$\frac{d\sigma}{d\cos\theta} = \frac{\pi\alpha}{2s}\left[(1+\cos^2\theta)A\cos\theta B\right]. \tag{1.60}$$

---

[2] The presence of this 1/3 coefficient in the Drell-Yan cross section measurements provided one of the first evidences for the existance of the color quantum number

where A and B are are functions that depend on the weak isospin and charge of the incoming quarks and the $\mu^+\mu^-$ invariant mass:

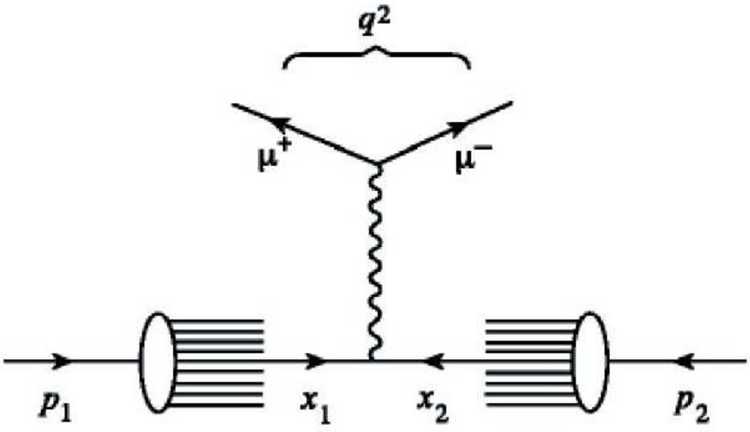

Figure 1.4: The Drell-Yan process, as explained with the parton model.

Chapter 2

The CMS experiment at LHC

The high energy experiments have provided confirmation of the Standard Model predictions up to the $\sim$ TeV energy scale. However, despite the outstanding agreement between experimental results and the predictions of the theory, no evidence has been found of the existence of the Higgs boson. Without the Higgs sector to explain the particles' masses, the SM would be a phenomenological, though accurate, explanation of particle interactions at the currently accessible energy scale (up to few TeV). The Large Hadron Collider (LHC) is a machine built to explore particle physics up to the design energy of 14 TeV. The main tasks for experiments at LHC will be the test of the SM behavior at the high energy frontier, the search for the Higgs boson and new physics beyond Standard Model.

2.1 The LHC collider

The Large Hadron Collider[21] is a 27 km circumference particle accelerator built at CERN (European Centre for Nuclear Research)[22], spanning the Swiss-French border. It is located about 100 m underground in the former LEP[23] collider cave. The machine is built to accelerate two proton beams up to an energy of 7 TeV each, which will be brought to collision in 4 interaction points (IP). The bunch crossing frequence is 40 MHz, which corresponds to a time interval between two bunches of 25 ns. Each bunch will contain about $3 \cdot 10^{34}$ protons. LHC comprehends high field (up to 8.4 T) dipole magnes to deflect particles and keep them on track, and relies on 400 MHz radiofrequency cavities for particles acceleration. The pre-acceleration system for LHC uses pre-existent accelerating structures at CERN: the Linac, the Booster, the PS (Proto Synchrotron) and the SPS (Super Proto Synchrotron). An hydrogen source provides the protons. The Linac accelerates protons up to 50 MeV, then Booster, PS and SPS boost the particles to 1.4, 25 and 450 GeV respectively, before they are finally injected into the LHC.

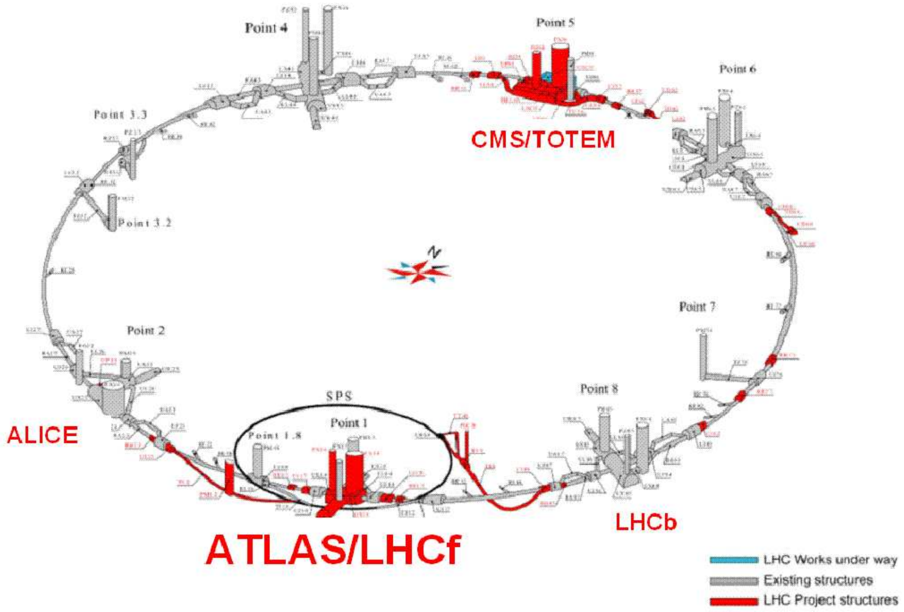

Figure 2.1: Overview of the LHC machine.

The luminosity for an hadron collider is given by:

$$\mathcal{L} = \frac{\gamma f k_B N_p^2}{4\pi\epsilon_n\beta^*}F, \tag{2.1}$$

where γ is the lorentz factor of the proton, f is the revolution frequency. k_B is the number of bunches, N_p is the number of protons per bunch, ϵ_n normalized transverse emittance (whose design value is 3.75μm), β^* is the betatron function at the IP and F is the reduction factor due to the crossing angle. The design luminosity for LHC is $\mathcal{L} = 10^{+}34\text{cm}^{-2}\text{s}^{-1}$, leading to around 1 billion proton-proton interaction per second. Parameters for LHC beams are given in table . Since two beams of particles with the same charge must be accelerated in opposite directions, two independent magnetic pipes are needed. They are however housed in the same yoke and cryostat system. The magnet coil are operated at 1.9^o K with a current of 15000 A, and have to withstand forces of some hundred of tons per meter during ramp up of the

Table 2.1: The machine parameters relevant for the LHC detectors

Variable		pp	HI	
Energy per nucleon	E	7	2.76	TeV
Lorentz factor	γ	~ 7000	2750	
Dipole field at 7 TeV	B	8.33	2.76	T
Design Luminosity	$\mathcal{L}$	10^{34}	10^{27}	$\mathrm{cm}^{-2}\mathrm{s}^{-1}$
Bunch separation		25	100	ns
Number of bunches	k_B	2808	592	
Number of particles per bunch	N_P	1.15×10^{11}	7.0×10^{7}	
β-value at IP	β^*	0.55	0.5	m
RMS	σ^*	16.7	15.9	μm
Luminosity lifetime	τ_L	15	6	hr
Number of collisions/crossing	n_C	~ 20		

magnetic fields. The LHC will consist of 1232 main dipoles and 392 main quadrupoles. Four experiments are located at the interaction points: CMS (Compact Muon Solenoid), ATLAS (A Toroidal LHC ApparatuS), LHCb[1] (Large Hadron Collider Beauty experiment) and ALICE[2] (A Large Ion Collider Experiment).

2.2 The CMS detector

The Compact Muon Solenoid (CMS)[28] experiment takes its name from the compact and homogeneous detector. CMS's main feature is the high magnetic field (4 T), which allows a compact design of the apparatus. CMS detector is composed of cylindrical layers coaxial to the beam pipe, called barrel layers, and two endcaps that ensure hermitical closure of the detector. Starting nearest to the beam interaction point, the constituent sub-detectors are the Tracker (which composes of the Pixel detector and the Silicon Strip Tracker), the Electromagnetic Calorimeter (ECAL), the Hadronic Calorimeter (HCAL) and the superconducting solenoidal magnet, followed by layers of Muon Chambers interspersed with iron Return Yoke. Characterisation

---

[1] LHCb does not work within the PP center of mass system, in order to investigate CP violation. One of the interacting beams comes directly from SPS

[2] ALICE is actually a ion-ion collision experiment

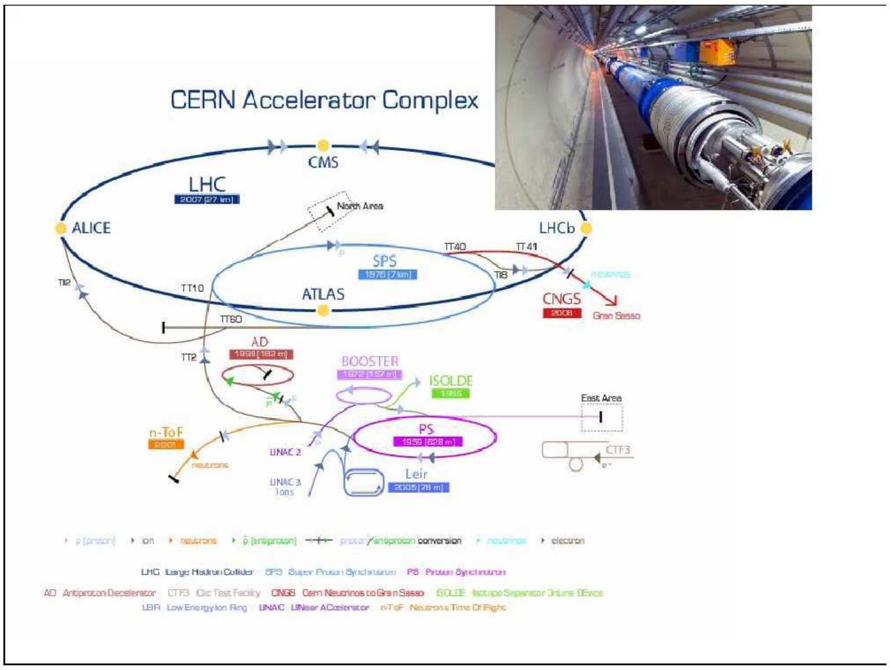

Figure 2.2: LHC structures and experiments locations.

of particles is achieved by examining their interaction with different sub-detectors. The main CMS Sub-detectors are illustrated in Figure (2.3) All electrically charged particles leave a trail of ionisation in the central silicon tracker, and photons/electrons and hadrons deposit all of their energy in the ECAL and HCAL respectively. Muons, which have low energy loss in the calorimeters, are identified by the muon tracking system at high radius; the magnetic field acts in opposite direction outside the solenoid hence the muon tracks bend in opposite directions in the tracker and in the muon detectors.

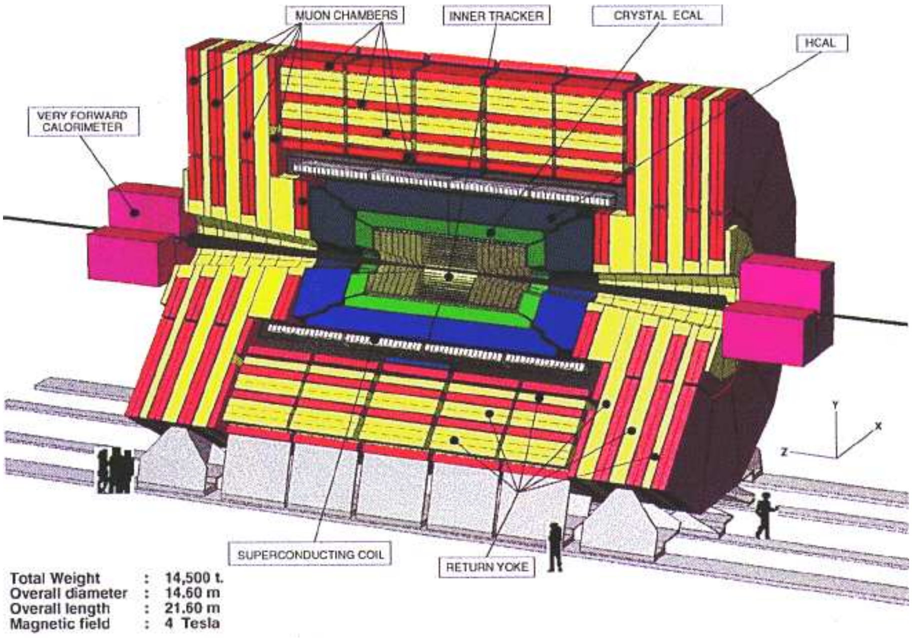

Figure 2.3: Overview of the CMS experiment.

The coordinate frame

The coordinate frame is centered at the nominal interaction point, the z axis is coaxial with the beam pipe and the $x - y$ plane is therefore orthogonal to the beam, with the x axis pointed towards the center of LHC and the y axis pointing upwards. Since the detector has a cylindrical symmetry around the z axis, a pseudo-angular reference is used: r is the radial distance from the z axis, ϕ is the azimuthal angle measured from the x axis and η is the pseudorapidity, defined as $\eta = -\ln\tan(\theta/2)$, where θ is the polar angle

measured from the z axis.
Physical observables of interest are the particles transverse momentum p_T and transverse energy E_T. The overall missing transverse momentum $\not{p}_T$ and the overall missing transverse energy $\not{E}_T$ are important observables for Beyond Standard Model physics processes.

Experimental challenges and design choices

LHC's characteristics pose several experimental challenges for the CMS detector.
The nominal time interval between two bunch-crossings is 25 ns and the foreseen event rate is about 10^9 events/s. The trigger system must filter this rate down to about 100 events/s, that is the maximum sustainable frequency for writing on the mass storage system. To achieve this goal, the trigger logic was designed around the short bunch-crossing time interval.
Moreover, the number of events per crossing is:

$$N_{BC} = \frac{number of events/s}{number of bunches/s} = \frac{10^9}{40 \cdot 10^6} = 25. \tag{2.2}$$

In this scenario two or more particles from different collisions of the same bunch-crossing may be revealed in the same sector of a sub-detector. In the same way, if the detector's response (or the readout electronics) is slower than 25 ns, hits from different bunches may overlap. Products from different processes of the same bunch or even different bunches can therefore "pile up" on the same detector channel, thus making the information on the event incorrect. This problem can be solved thanks to a high granularity, that is high spatial and temporal resolution, of the detector. Another problem is that all sub-detector parts must withstand constantly high radiation doses for a long amount of time without a decrease of the performances. Also, requests are made for the resolution on physical observables of interest:

Muons : Muons must be reconstructed in the range $|\eta| < 2.5$ with correct charge up to transverse momentum scale of $p_T \approx 1\,\mathrm{TeV}/c$. Good resolution on the invariant mass of muons pairs is crucial (1% at $100\,\mathrm{GeV}/c^2$).

Photons and Electrons : Photons and electrons energy reconstruction must be excellent in the $|\eta| < 2.5$ range. Mass resolution of order of 1% at $100\,\mathrm{GeV}/c^2$ for photon and electron pairs is required for background rejection.

Jets and missing energy : Jets must be reconstructed with accurate transverse energy in a large angular interval ($|\eta| < 5$) in order to estimate the missing transverse energy $\not{E}_T$.

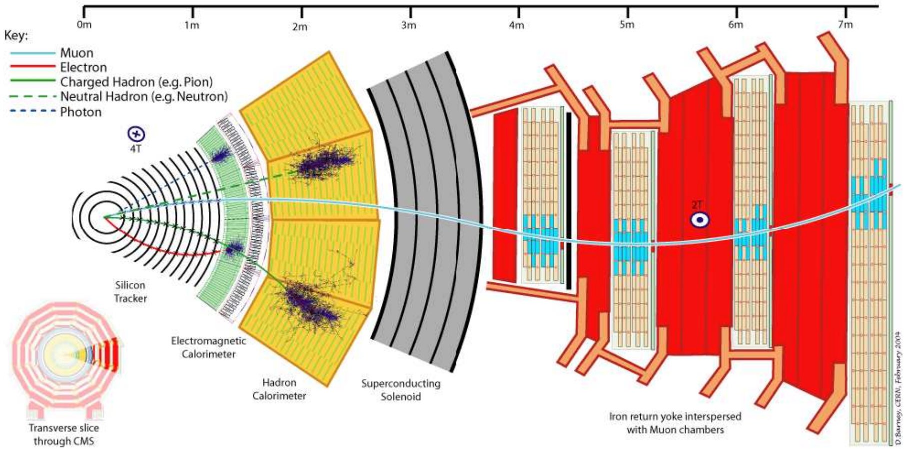

Figure 2.4: A muon passing through the CMS detector.

Tracks : Robust track identification and good p_T resolution is required for all selection criteria. Vertex reconstruction in the proximity of the interaction point is fundamental for τ and b-tagging.

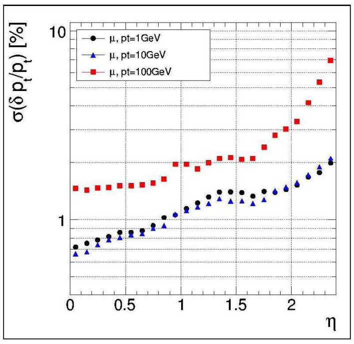

Figure 2.5: Resolution of muons p_T at three different scales.

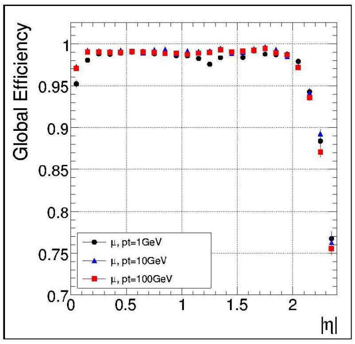

Figure 2.6: Muon track global reconstruction efficiency at three different p_T scales.

CMS requirements for sub-detectors are therefore high granularity, radiation hardness and hermiticity. The design of sub-detectors had to take into account all the mentioned problems and requests. The choices for the sub-detectors have been the following[29]:

Tracker $r < 1.2\,\mathrm{m}$, $|\eta| < 2.5$; consists of a high resolution pixel vertex detector and a silicon strip tracker with an active area of 200 m^2.

Electromagnetic Calorimeter (ECal) $1.2 < r < 1.8\,\mathrm{m}$, $|\eta| < 3.0$; consists of 61 200 lead tungstate crystals for photon and electron identification.

Hadronic Calorimeter (HCal) $1.8 < r < 2.9\,\mathrm{m}$, $|\eta| < 5.0$; consists of plastic scintillators and brass absorbers to identify jet position and jet transverse energy.

Magnet $2.9 < \mathrm{r} < 3.8$ m, $|\eta| < 1.4$; 4 T magnetic field supplied by a superconducting solenoid

Muon System $4.0 < \mathrm{r} < 7.4$ m, $|\eta| < 2.4$; drift tubes and cathode strip chambers to detect muons and their sign up to a transverse momentum of ≈ 1 TeV. Resistive plate chamber detectors with excellent time resolution are used to correctly identify the bunch crossing of the event.

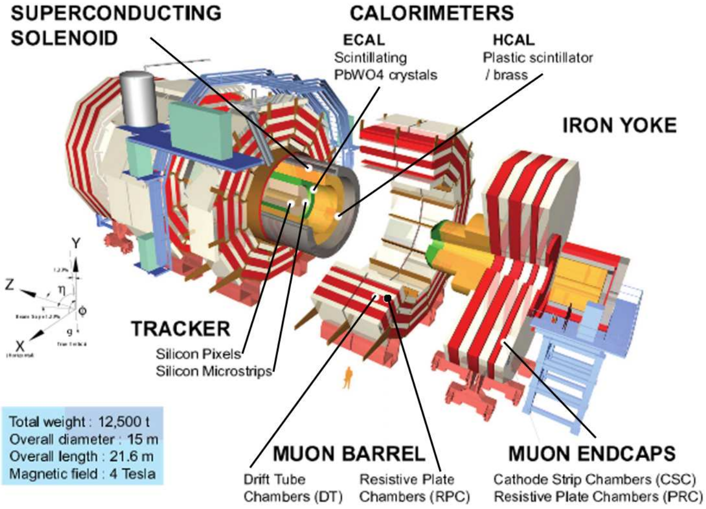

Figure 2.7: Overview of the CMS sub-detectors.

2.2.1 The Tracking system

The CMS tracker[31][32] should provide robust and accurate tracking and vertexing information for charged particles. It is the closest sub-detector to the interaction point. Due to the high radiation environment it has to be ensured that the detectors and their parts are sufficiently radiation hard to guarantee their operation over the full data taking period of the experiment. To better solve the pattern recognition problem, the tracker is designed to fulfill two basic properties: low cell occupancy and large hit redundancy. CMS has decided to build the entire tracking sub-detector of silicon pixel and silicon microstrip detectors, with a structural support made of carbon fibre composite. To reach sufficient radiation hardness and limit the leakage current of the devices, the whole tracker volume has to be cooled down to -10^o C. The layout of the CMS Tracker is shown in Figure (2.8). The outer radius of the CMS tracker extends to nearly 110 cm, and its total length is approximately 540 cm. Close to the interaction vertex, in the barrel region, there are 3 layers of hybrid pixel detectors at radii of $4.4, 7.3,$ and10.2 cm. In the barrel region, the silicon microstrip detectors are placed at r between 20 and 110 cm. The total area of the pixel detector is $\approx 1\,\mathrm{m}^2$, while that of the silicon strip detectors is $\approx 200\,\mathrm{m}^2$, providing coverage for $|\eta| < 2.4$. The inner tracker comprises 66 million pixels and 9.6 million silicon strips. With these features the inner tracker is able to reconstruct single leptons with an efficiency close to 100% and with a momentum resolution better than 3% within $|\eta| < 2.0$ or single muons momenta, as shown in Figure (2.5).

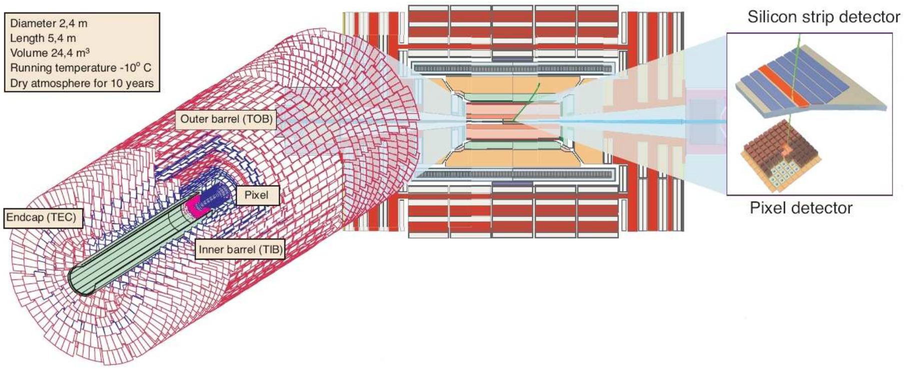

Figure 2.8: Overview of the CMS Tracker.

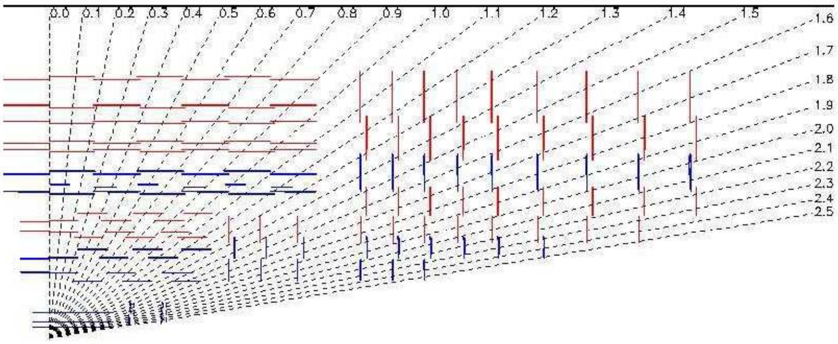

Figure 2.9: A sketch of the tracker layout in the longitudinal plane. Red lines represent single-sided modules and blue lines represent double-sided modules which have two sensors mounted back to back.

Pixel tracker

The pixel detector is a fundamental device for b and τ-tagging studies and track impact parameter measurements. It is also important as a starting point in reconstructing charged particle tracks. It consists of 3 barrel layers with 2 endcap disks on each side. The 3 barrel layers are located at mean radii of 4.4 cm, 7.3 cm and 10.2 cm, and have a length of 53 cm. The two end disks, extending from 6 to 15 cm in radius, are placed on each side at $|z| = 34.5$ cm and $|z| = 46.5$ cm, so that the entire region with $|\eta| < 2.4$ is covered. At high luminosity conditions, the inner barrel layer will be substituted by an outer layer placed at $r = 13$ cm to improve resolution and limit radiation damage. In order to achieve the optimal vertex position resolution, a design with pixel shape with a surface of $100 \times 150\,\mu\text{m}^2$ and a thickness of $300\,\mu\text{m}^2$. The barrel comprises 768 pixel modules arranged into half-ladders of 4 identical modules each. The large Lorentz effect (Lorentz angle is 23^o) improves the (r, ϕ) resolution. The endcap disks are assembled in a turbine-like geometry with blades rotated by 20^o to also benefit from Lorentz effect. The endcap disks comprise 672 pixel modules with 7 different modules in each blade. The spatial resolution is measured to be about 10μm for the (r, ϕ) measurement and about 20μm for the z measurement. The detector readout uses approximately 16 000 chips, which are bump-bonded to the detector modules. The life time at full luminosity is 2, 5 and 10 years for the inner, middle and outer layers respectively.

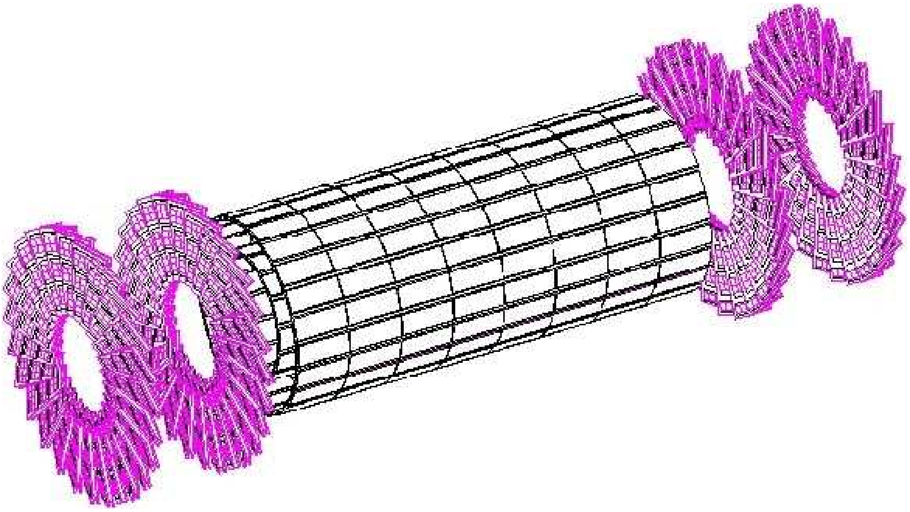

Figure 2.10: Overview of the CMS Pixel detector.

Silicon strip tracker

The barrel region is divided into 2 parts: a TIB (Tracker Inner Barrel) and a TOB (Tracker Outer Barrel). The TIB is made of 4 layers and covers up to $|z| < 65$ cm, using silicon sensors with a thickness of $320\,\mu$m and a strip pitch which varies from 80 to $120\,\mu$m. The first 2 layers are made with stereo modules in order to provide a measurement in both $r-\phi$ and $r-z$ coordinates. A stereo angle of 100 mrad has been chosen. This leads to a resolution between $23-34\,\mu$m in the $r-\phi$ direction and $230\,\mu$m in the z direction. The TOB comprises 6 layers with a half lenght of $|z| < 110$ cm As the radiation levels are smaller in this region, thicker silicon sensors ($500\,\mu$m) can be used to mantain a good signal to noise ratio for longer strip length and wider pitch. The strip pitch varies from 80 to $120\,\mu$m. Also for the TOB, the first 2 layers provide a "stereo" measurement in both $r-\phi$ and $r-z$ coordinates, again with a stereo angle of 100 mrad. This leads to a resolution between $35-52\,\mu$m in the $r-\phi$ direction and $530\,\mu$m in the z direction.

The endcaps are divided into the TEC (Tracker End Cap) and TID (Tracker Inner Disks). Each TEC comprises 9 disks that extend into the region 120 cm $< |z| <$ 280 cm , and each TID comprises 3 small disks that fill the gap between the TIB and TEC. Both TEC and TID modules are arranged in rings, centered on the beam line, and have strips that point toward the beam line. The first 2 rings of the TID and the innermost 2 rings and the

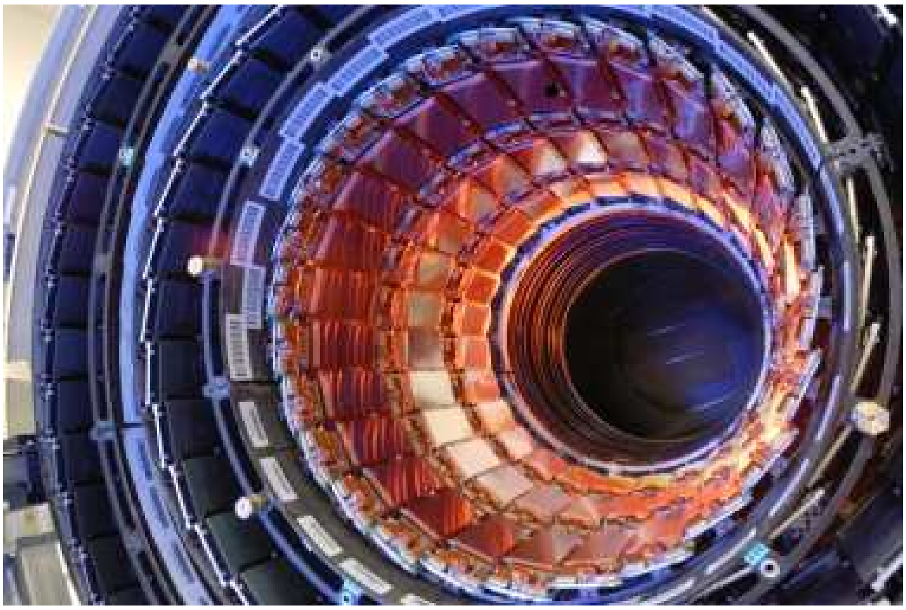

Figure 2.11: The barrel of CMS Silicon Strip Tracker.

fifth ring of THE TEC have stereo modules. The thickness of the sensors is 320 μm for the TID and the 3 innermost rings of the TEC and 500 μm for the rest of the TEC. The entire silicon strip detector consists of almost 15 400 modules, which are mounted on carbon-fibre structures and housed inside a temperature controlled outer support tube. The operating temperature will be around -20 Â°C.

2.2.2 The Electromagnetic Calorimeter

A high performance electromagnetic calorimeter is a fundamental requirement for CMS, as precise measurements on electrons and photons are required. In particular, since for $M_H < 135$ GeV the main discovery channel for the Higgs boson is $gg \rightarrow H \rightarrow \gamma\gamma$, the invariant mass resolution of photon pairs should be of order of 1% to enhance the significance of a possible signal. The CMS collaboration has chosen an hermetic, homogeneous electromagnetic calorimeter (ECAL)[33] comprising 61200 lead tungstate ($PbWO_4$) crystals mounted in the central barrel part and 7342 crystals in each of the 2 endcaps (Figure 2.12). The lead tungstate crystals have a short scintillation decay time ($\tau \simeq 10$ ns) that allows to collect 85% of the light in the 25 ns interval between two crossings. The small Moliere radius of 21.9 mm and radiation length ($X_0 = 8.9$ mm) permits the shower containment in a limited

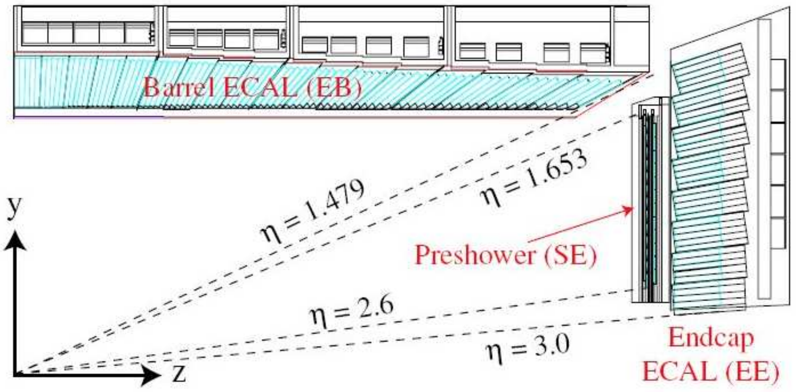

Figure 1.17: Longitudinal view of the Electromagnetc Calorimeter.

Figure 2.12: A longitudinal view of CMS ECAL.

space resulting in a compact calorimeter design. The barrel section (EB) has an inner radius of 129 cm. It is structured as 36 identical "supermodules", each covering half of the barrel length and corresponding to a pseudorapidity interval of $0 < |\eta| < 1.479$. The crystals are quasi-projective (the axes are tilted of 3^o with respect to the line from the nominal vertex position) and cover an angular aperture of 0.0174 rad(i.e. 1^o) in $\Delta\phi$ and $\Delta\eta$. The barrel crystals have a front face of about $22 \times 22\,\mathrm{mm}^2$, which matches well the Moliere radius of 21.9 mm. To limit fluctuations on the longitudinal shower leakage of high energy electrons and photons the crystals were chosen with a total thickness of 25.8 radiation lengths, corresponding to a crystal length of about 23 cm. An R&D programme has shown that radiation does not affect either the scintillation mechanism or the uniformity of the light yield along the crystal. Radiation only affects the transparency of the crystals through the formation of color centers. This light loss will be monitored by a light-injection system. The endcaps (EE) are situated at a distance of 314 cm from the vertex and covering a pseudorapidity range $1479 < |\eta| < 3.0$. Endcaps are structured as 2 "Dees", consisting of semi-circular aluminium plates on which are mounted structural units of 5×5 crystals, known as supercrystals. The endcap crystals, like the barrel crystal, are displaced with respect to the nominal vertex position, and they are arranged as blocks with regular geometry in the $x - y$ coordinates, rather than in $\eta - \phi$ coordinates. They are all identical with a face of $28.6 \times 28.6\,\mathrm{mm}^2$ and a lenght of 220 mm(24.7

X_0). A preshower device is placed in front of the crystal calorimeter over much of the endcap pseudorapidity range to help in neutral pions identification and to improve the electron tagging against minimum ionising particles. The preshower detector is a sampling calorimeter with 2 layers: lead radiators initiate electromagnetic showers from incoming photons/electrons whilst silicon strip sensors placed after each radiator measure the energy deposited and the transverse shower profiles.

The performance of a supermodule was measured in a test beam. Representative results on the energy resolution as a function of beam energy are shown in Figure (2.13). The energy resolution, measured by fitting a Gaussian function to the reconstructed energy distributions, has been parametrised as a function of energy:

$$\left(\frac{\sigma}{E}\right)^2 = \left(\frac{S}{\sqrt{E}}\right)^2 + \left(\frac{N}{E}\right)^2 + C^2 \tag{2.3}$$

where S is the stochastic term, N the noise and C the constant term. The values of the parameters are listed in the figure.

2.2.3 The Hadronic Calorimeter

The Hadronic Calorimeter (HCAL)[34] plays an essential role in the identification and measurement of quarks, gluons, and neutrinos by measuring the energy and the direction of jets and the missing transverse energy flow in events. Missing energy is a crucial signature for new particles search, like the supersymmetric ones. For good missing energy resolution, an hermetic calorimetry coverage up to $|\eta| < 5$ is required. The HCAL will also aid the identification of electrons, photons and muons in conjunction with the tracker, the ECAL and muon system. The design of HCAL is strongly influenced by the choice of magnet parameters since most of the CMS calorimetry is located inside the magnet coil and surrounds the ECAL system. An important requirement of HCAL is to minimize the non-Gaussian tails in the energy resolution and to provide good containment and hermiticity for the $\not{E}_T$ measurement. Hence, the HCAL design maximizes material inside the magnet coil in term of interaction lengths. This is complemented by an additional layer of scintillators, referred to as the Hadron Outer Calorimeter (HO), lining the outside of the coil. The hadron barrel (HB) and hadron endcap (HE) calorimeters (Figure 2.14) are sampling calorimeters with 50 mm thick copper absorber plates which are interleaved with 4 mm thick scintillator sheets.

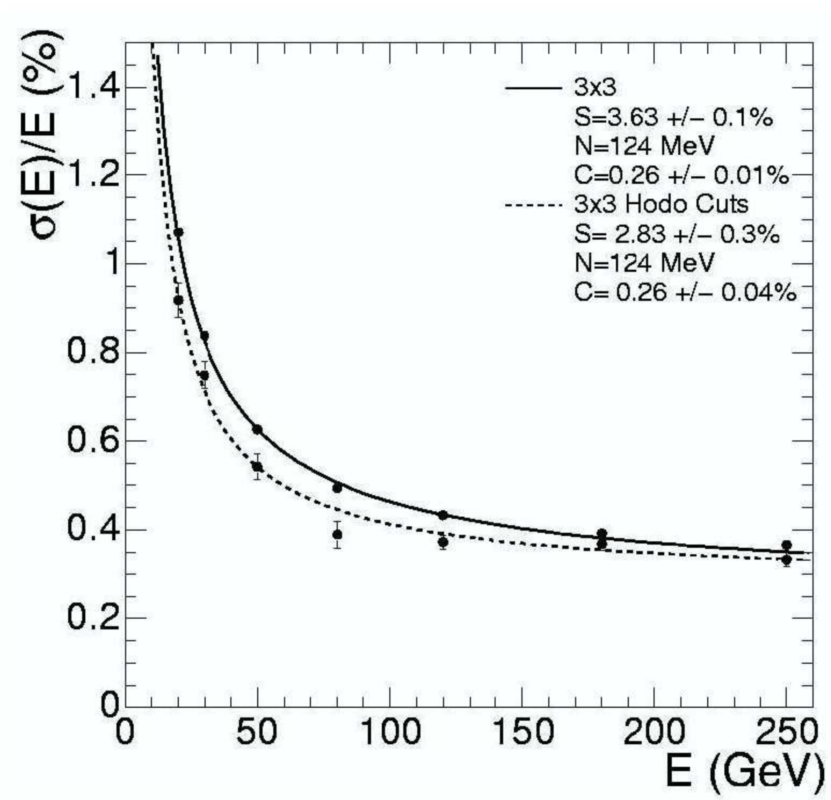

Figure 2.13: ECAL energy resolution.

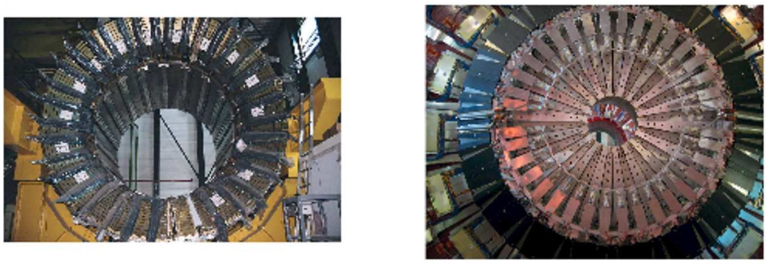

Figure 2.14: The HCAL barrel(left) and endcap(right).

Copper has been selected as the absorber material because of its density. The HB is constructed of two half-barrels each of length 4.3 m. It consists of 32 towers covering the pseudorapidity region $-1.4 < |\eta| < 1.4$, resulting in 2304 towers with a segmentation $\Delta\eta \times \Delta\phi = 0.087 \times 0.087$. The HB is read out as a single longitudinal sampling. There are 15 brass plates, each with a thickness of about 5 cm, plus 2 external stainless steel plates for mechanical strength. The Hadron Outer Calorimeter (HO) contains 10 mm thick scintillators, which line the outside of the outer vacuum tank of the coil and cover the region $-1.26 < |\eta| < 1.26$. The tiles are grouped in sectors with a 30^o aperture each, matching the ϕ segmentation of the drift tube chambers of the muon detector. They sample the energy from penetrating hadron showers leaking through the rear of the calorimeters and serve as "tail catcher" after the magnet coil. They increase the effective thickness of the hadron calorimetry to over 10 interaction lengths, thus reducing the tails in the energy resolution function. The HO also improves the $\not{E}_T$ resolution of the calorimeter. The HE are two large structures, situated at both ends of the barrel detector and within the region of high magnetic field. Each hadron endcap contains 14 towers along the η coordinate, covering the pseudorapidity region $1.3 < |\eta| < 3.0$. The 6 outermost towers (at smaller η) cover ranges of 0.087 along the η coordinate, and are segmented by steps of 5^o along the ϕ coordinate. For the remaining towers the ϕ segmentation is 10 and the η range varies from 0.09 to 0.35 at the highest η. To read the HCAL the blue violet light emitted from the tiles is absorbed by the wave shifting fibres which fluoresce in the green, then the waveshifted light is conveyed via clear fibre waveguides to hybrid photodiodes (HPDs). There are two Hadronic Forward Calorimeters (HFC), one located at each end of the

CMS detector, which complete the HCAL Coverage to $|\eta| = 5$. The HFC detector is situated in a region where radiation field is coarse and is built of steel absorber plates. Radiation-resistant quartz fibers are inserted into the absorber plates. The energy of jets is measured from the Cherenkov light signals produced as charged particles pass through the quartz fibers. These signals result mainly from the electromagnetic component of showers, which results in good directional information for jet reconstruction. The front face is located at 11.2 m from the interaction point. The depth of the absorber is 1.65 m. The the diameter of the quartz fibers is 0.6 mm and they are placed 5 mm apart in a square grid. The quartz fibers are parallel to the beam line and have two different lengths (1.43 and 1.65 m) which are inserted into grooves, creating 2 effective longitudinal samplings. There are 13 towers in $|\eta|$, all with a size given by $\Delta\eta \approx 0.175$, except for the lowest-η tower with a $\Delta\eta \approx 0.1$ and the highest-η tower with a $\Delta\eta \approx 0.3$. The ϕ segmentation of all towers is 10 except for the highest-η tower which have $\Delta\phi = 20$. This leads to 900 towers and 1800 channels in the 2 HF modules. Fiber optics convey the Cherenkov signals to photomultiplier tubes which are located in radiation shielded zones. The performance of the HCAL is obtained comparing the simulated single particle energy response with test beam data from all 3 geographic parts of the HCAL. However, HCAL's performances were optimized to obtain the best possible jet energy resolution and $\not{E}_T$ resolution. The granularity of the sampling in HCAL has been chosen such that the energy resolution, as a function of E_T, is similar in all 3 parts of the detector (Figure 2.15).

2.2.4 The Magnet

The compact design of CMS requires a very strong magnetic field in order to produce a sensible bending of the charged particle trajectories so that the momentum of high energy particles can be measured. The basic design goal was to be able to reconstruct 1 TeV muons with about $10\% p_T$ resolution. p_T resolution also scales with $1/B$, where B is the strength of the magnetic field. The bending of tracks with different momenta in a 4 Tesla field is illustrated in Figure (2.16). At this field strength, trajectories of charged particles with $P_T > 0.7$ GeV reach the ECAL front surface (in the absence of tracker material), and muons with $p_T > 4$ GeV extend through the muon chambers. The magnetic field is created by a superconducting coil situated just outside the calorimeters at a radius of 2.9 m, and returned by 3 layers

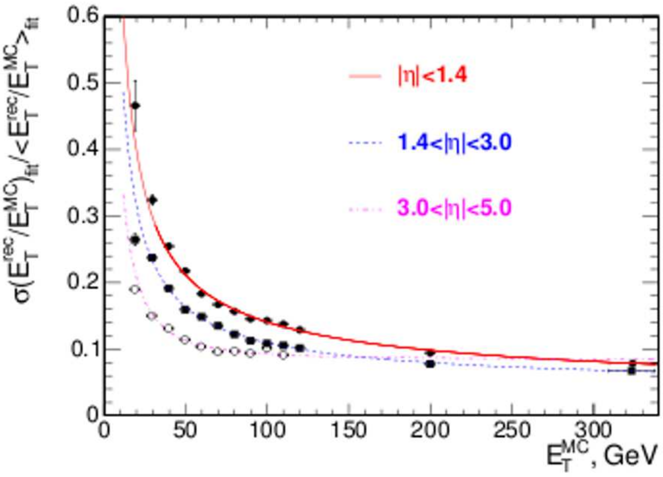

Figure 2.15: HCAL energy energy resolution.

of iron yokes with a combined thickness of 1.55 m in the barrel and 1.45 m in the endcaps.

2.2.5 The Muon Detector

The CMS detector is a general purpose detector specifically optimized for muon measurement. Three types of gaseous detectros are used to identify and measure muons[35]. The choice of the detector technologies has been driven by the very large surface to be covered and by the different radiation environments. In the barrel region ($|\eta| < 1.2$), where the neutron induced background is small, the muon rate is low and the residual magnetic field in the chambers is low, drift tube (DT) chambers are used. In the two endcaps, where the muon rate and the neutron induced background is high, catode strip chambers (CSC) are deployed and cover the region up to $|\eta| = 2.4$. In addition to these, resistive plate chambers (RPC) are used both in the barrel and the endcap regions. The layout of one quarter of the CMS muon sysyem for initial low luminosity running is shown in Figure (2.17). In the Muon Barrel (MB) region, 4 stations of detectors are arranged in cylinders interleaved with the iron yoke. The segmentation along the beam direction follows the 5 wheels of the yoke (labelled from YB-2 to YB+2 following the z axis direction). In each of the endcaps, the CSCs and RPCs are arranged in

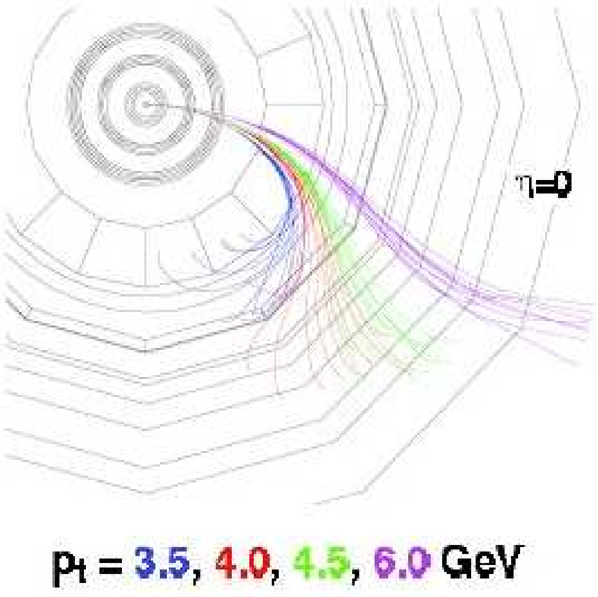

Figure 2.16: Horizontal view of muon tracks of different p_T bending in the magnetic field.

4 disks (labeled from the innermost to the outermost along the z axis ME1-4 perpendicular to the beam, and in concentric rings: 3 rings in the innermost station, 2 in the others(labeled from the innermost to the outermost in the radial direction). The muon system contains order of 25 000 m^2 of active detection planes total, and nearly 1 million electronic channels. The Barrel Detector consists of 250 chambers organized in 4 layers (labelled MB1-4 from the innermost to the outermost) inside the magnet return yoke at radii of approximately 4.0, 4.9, 5.9 and 7.0 m from the beam axis. Each of the 5 wheels of the Barrel Detector is divided into 12 sectors, each covering a 30 azimuthal angle. The MB1, 2 and 3 chambers consist of 12 planes of aluminium drift tubes; 4 $r - \phi$ measuring planes in each of the 2 outermost "superlayers", separated by about 20 cm and sandwitching a z-superlayer comprising 4 z-measuring planes (Figure 2.18). The MB4 station does not contain the z-measuring planes. The maximum drift lenght is 2.0 cm and the single-point resolution is $\approx 200\,\mu$m. Each station is designed to give a muon vector three-momentum in space, with ϕ precision better than $100\,\mu$m in position and about 1 mrad in angle. Each DT chamber has 1 or 2 RPCs coupled to it before installation, depending on the station. In stations MB1 and MB2 each package consists of 1 DT chamber sandwitched between 2

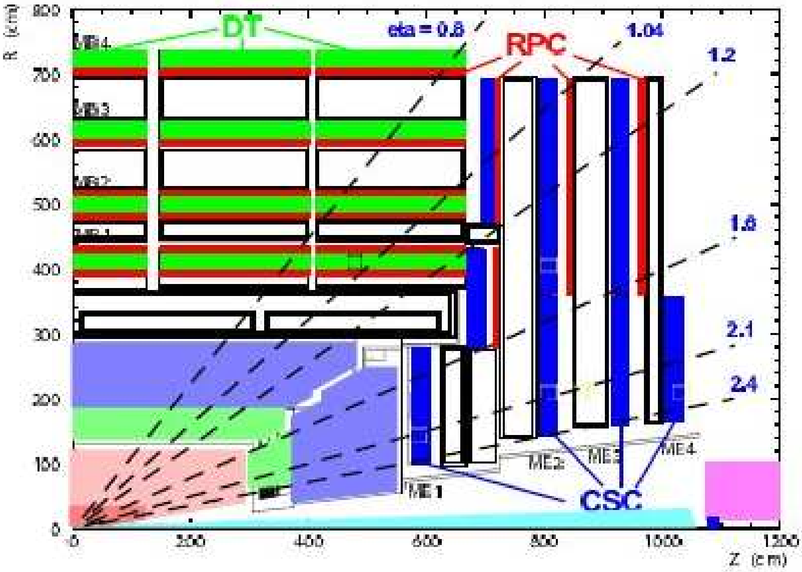

Figure 2.17: Layout of one quarter of the CMS muon system, in a configuration where the RPC system is limited to $|\eta| < 6$, and only the inner ring of the ME4 chambers has been deployed. This configuration will be deployed for low-luminosity scenario.

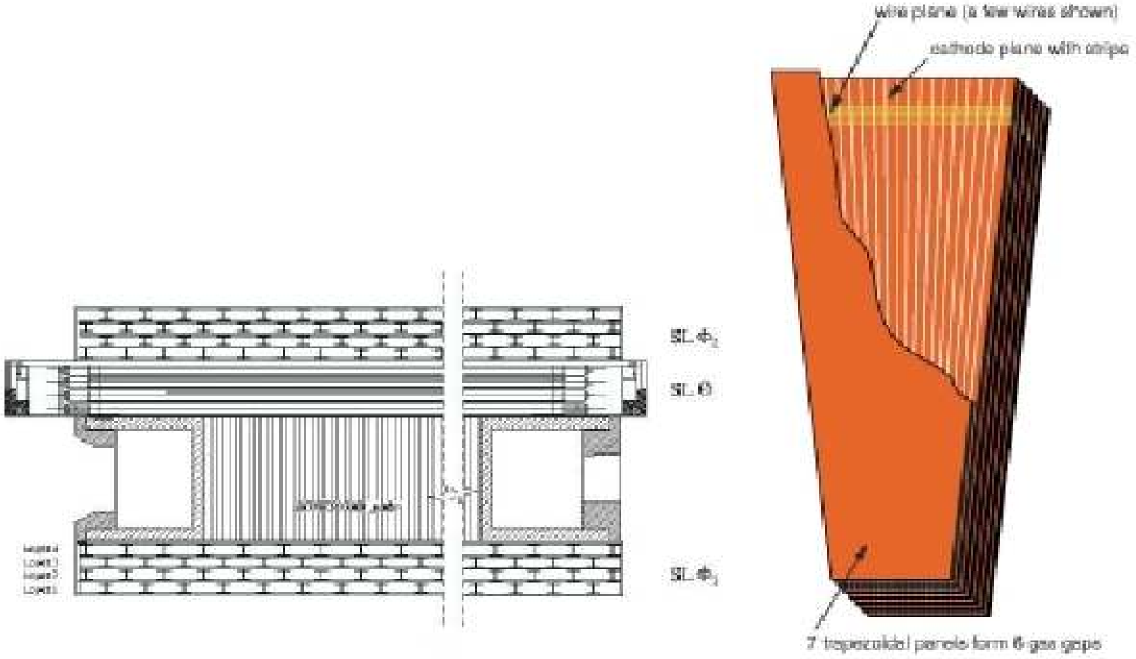

Figure 2.18: Left: the layout of a DT chamber inside a muon barrel station. Right: schematic view of a CSC chamber

RPCs. In stations MB3 and MB4 each package consists of 1 DT chamber and 1 RPC, which is placed on the innermost side of each station. A high p_T muon thus crosses up to 6 RPCs and 4 DT chambers, producing up to 44 measured pointsin the DT system from which a muon-track candidate can be built. The muon Endcap (ME) system comprises 468 CSCs arranged in 2 endcaps. Each endcap is divided into four stations, labeled ME1-4 from the innermost to the outermost, where the CSCs are arranged in rings centered on the beam axis. Each station contains 3 rings, labeled ME1/1-3 from the closest to the beam axis to the farthest. CSCs are multiwire proportional chambers with segmented cathode readout. High precision coordinate along the wire is obtained by extrapolation of charges induced on several adjacent cathode strips. The strip width varies from 3.2 to 16 mm. Offline resolution is in the range between 80μm and 450μm for one layer. CSC chambers have trapezoidal shape and one chamber consists of six detecting layers. The Layers are separated by 16 mm thick polycarbonate plastic honeycomb panels. In each layer the strip are run radially. In angular units the strip width $\Delta\phi$ varies from 2.0 to 4.3 mrad and the lenght $\Delta\eta$ from 0.35 to 0.60. The combined off line resolution of six layers opproaches 50 μm. The wires are perpendicular to the strips, except in ME1/1 where the wires are tilted by 25, in order to compensate the Lorentz effect due to the intense magnetic field. RPC chambers are located both in the barrel and in the endcaps. These RPCs are operated in avalanche mode to ensure good operation at high rates (up to $10KHz/\text{cm}^2$) and have double gaps with a gas gap of 2 mm. RPCs provide a fast response with good time resolution (order of ns) at the cost of a coarse position resolution and can unambiguously identify the correct bunch crossing. Centrally produced muons tracks are measured 3 times: in the inner tracker, after the coil and in the return flux. Measurement of the momentum of muons using only the muon system is essentially determined by the muon bending angle at the exit of the 4 T coil, taking the interaction point (which will be known to $\approx 20\,\mu$m) as the origin of the muon. The resolution of this measurement is dominated by multiple scattering in the material before the first muon station up to p_T values of 200 GeV/c, when the chamber spatial resolution starts to dominate. For low momentum muons the resolution of muons reconstructed in the inner tracker is better by an order of magnitude. However, when multiple scattering and energy loss can be neglected, the muon trajectory beyond the return yoke can be extrapolated back to the beam line, taking into account the inversion of track curvature before and after the coil. This can be used to improve the momentum resolution at high p_T scales when combining the inner tracker and muon detector measurements.

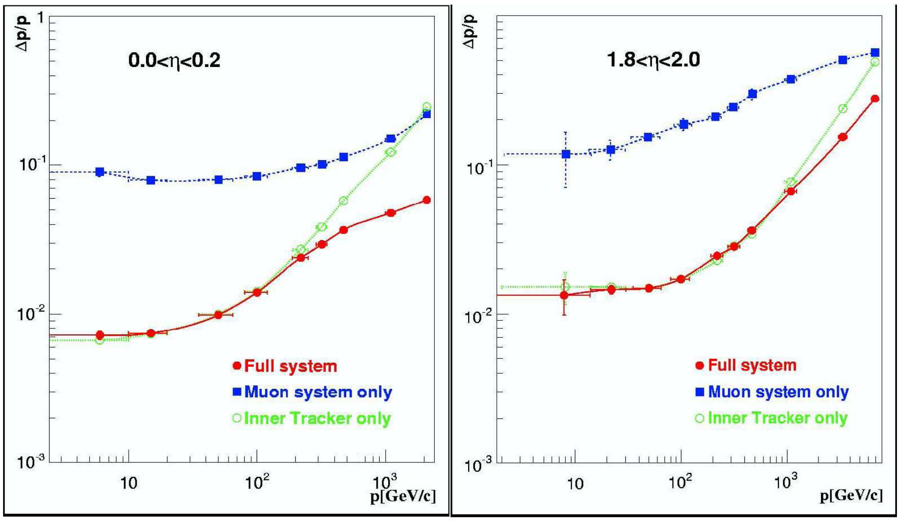

Figure 2.19: The muon momentum resolution versus p using the muon system only, the inner tracker only, or both ("full system") for: a) barrel, $|\eta| < 0.2$; b) endcap, $1.8 < |\eta| < 2.0$,

2.2.6 The Trigger system

The pre-selection of events and reduction of the data volume is carried out online by the trigger and the Data Acquisition (DAQ) system. Twenty inelastic p-p collisions occur every 25 ns at full LHC luminosity. However, only a small fraction of them are hard scattering interactions containing events with an interesting signature, and the rest are mostly minimum bias (MB) events, generally containing soft jets of hadrons. The CMS detector generates 1 MByte of data per bunch crossing, which amounts to an overall data rate beyond the available online processing power and storage capability to enable full analysis of each event. At CMS, these issues are managed by filtering the events in two stages: a Level-1 trigger (L1)[36] and High-Level Triggers (HLT)[37]. The L1 triggers first reduce the event rate from 40 MHz to 100 kHz (50 kHz at low luminosity), discarding any low p_T events, then the HLT further reduce the rate to 100 Hz, performing more detailed reconstruction of objects. The L1 trigger uses custom electronics with programmable chips, which will be located inside the counting room next to the underground interaction hall, whereas the HLT analysis is carried out in a filter farm with 1000 commercial computers. Algorithms used for HLT run within the same framework used for the offline analysis. Most of the physics channels considered by the CMS experiments can be characterised by the observation of high p_T stable leptons (electrons/muons) and high p_T jets in the central region of the detector, whereas the minimum bias events mostly contain soft jets distributed at high rapidity. These leptons are often accompanied by corresponding neutrinos from the decay of W bosons, which give rise to a large $\not{E}_T$ in the system. High p_T photons and hadronic decays of τ leptons (τ-jets) are important signatures of Higgs boson decays in the low mass scenario ($H \rightarrow \gamma\gamma$, $H \rightarrow \tau\tau$). Hence, the trigger decisions are made based upon the identification of the following physics objects,

- muons
- electrons/photons
- jets
- missing transverse energy

where each object is reconstructed in a specific detector sub-system or with combined information.

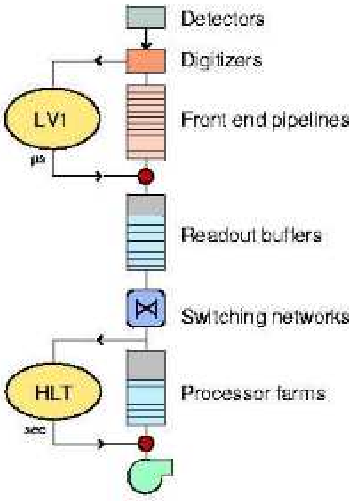

Figure 2.20: Data flow in the Trigger/DAQ system.

Level-1 Trigger

The Level-1 trigger decision has to be made every 25 ns, without deadtime, while full data are stored temporarily in pipeline memories in the front-end electronics of the sub-detectors. Due to this time restriction, and the number of channels and complexity of the reconstruction involved, the central tracking system is not used in the L1 trigger decision. The calorimeter objects (electrons, photons,τ-jets and jets) and muons are reconstructed by the corresponding sub-systems, each system producing four highest p_T candidate objects of each kind. The L1 Global trigger then sorts the trigger objects and makes a decision based on the kinematics of the individual object. The triggered objects are then passed to the subsequent DAQ system and HLT for further reconstruction and selection.

High level Trigger

The role of the HLT is to further reduce the data rate to ~100 Hz using a more detailed information and sophisticated reconstruction algorithms, and to make the final selection of events to be stored for offline analyses. The HLT is carried out on one event per processor basis. The data from ~700 front-end electronics are collected, synchronised, sorted and stored in a random access memory to be used for the event reconstruction. A processing time of ~40 ms for each bunch crossing is envisaged during the early runs (up to 1 second for high luminosity runs). The reconstruction and selection at the HLT is staged in two main sub-levels; objects which are identified irrelevant at each stage are discarded immediately to save processing time, while retaining sufficient information about rejected events for monitoring purposes. Typically, "Level-2" objects are the refined L1 candidates using full detector granularity. At "Level-3" information from the central tracking system is incorporated. A stand-alone full reconstruction of tracks and vertices are carried out in parallel and used for imposing isolation criteria and tagging of τ-jets and b-jets.

Chapter 3

The LHC Physics Program

3.1 The physics processes at LHC

LHC will be an unique experiment: both the amount of effort devolved into it and the effective size of the experiment itself are unparalleled in particle physics history. The reason is that LHC's expectations are also very ambitious: the machine will allow to explore a new and untested energy scale for particle physics, eventually reaching the limits at which the perturbative approach of the Standard Model fails. The physics program of LHC therefore includes tests and studies of the Standard Model, the search for the Higgs Boson and searches for new physics beyond Standard Model. LHC is a machine designed for discovery: it can reach high energies because of the reduced synchrotron radiation for protons, while in an e^+e^- machine the electron and positron bremsstrahlung limits the center of mass energy the accelerator can reach[1]. However, hadron colliders like LHC are not best suited for high precision measurements: hadron fragments after the collision (referred to as Underlying Event) create several experimental difficulties. Also, although the proton collision energy is 14 TeV, the maximum parton energy available for physics will be reduced to $\sqrt{x_1 x_2 s}$ where x_1 and x_2 are the momentum fraction of proton's momentum carried by each parton and $\sqrt{s}$ is the center of mass energy. On the other hand e^+e^- colliders provide a cleaner environment where all the initial state energy is available for the elementary.

---

[1] This is true assuming that the machine is a circular accelerator. The formula for the radiated power from a relativistic particle of charge e is:

$$P \propto e^2 \gamma^4 m_e/m,$$

where γ, m are the relativistic factor and the mass of the particle and m_e is the electron mass.

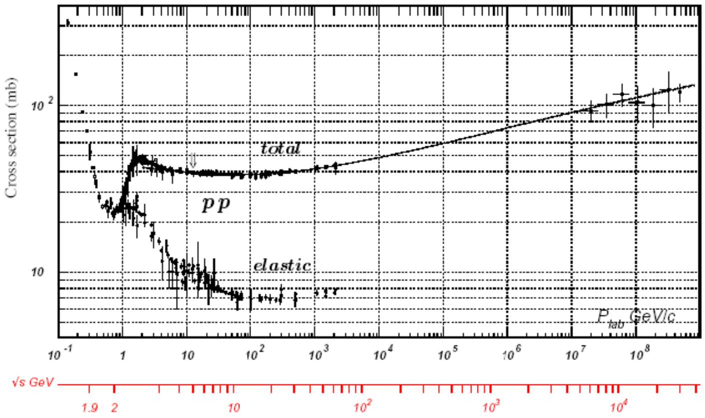

Figure 3.1: Total pp cross section in a pp collider as function of $\sqrt{s}$.

LHC will therefore be able to probe the physics at several TeV. The total proton-proton cross section at 14 TeV is $\approx$ 110 mb where contribution from inelastic processes cross section is 60 mb, contribution from single diffractive processes cross section is 12 mb and contribution from elastic scattering cross section is 40 mb. Proton-antiproton cross sections at the Tevatron and LHC are displayed in Figure (3.2). The Higgs cross section for a 150 GeV Higgs is about 109 times smaller than the total inelastic cross section. Note that at the LHC, the cross section for $m_H = 150$ GeV increases by about 100 times over the Tevatron. $t\bar{t}$ cross section increases by 200. Elastic and diffractive events produce particles with very small angles to the beam axis.

3.2 Higgs search at LHC

3.2.1 Higgs production

The main production channels for the Standard Model Higgs boson are:

- gluon fusion via top loop
- vector boson (W/Z) fusion
- $t\bar{t}$ fusion
- W/Z associated production

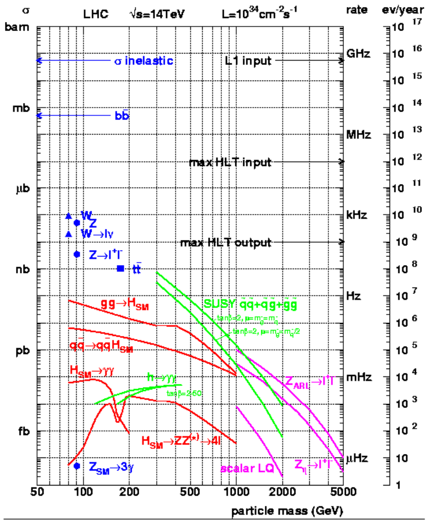

Figure 3.2: pp and $p\bar{p}$ cross section at $10^{34}\text{cm}^{-2}\text{s}^{-1}$ as function of $\sqrt{s}$ for different processes at LHC and at other hadron colliders.

The corresponding Feynman diagrams and the production cross section at the LHC as a function of the the Higgs mass are shown in Figure (3.3). For the entire range of the Higgs masses below 1 TeV, the production via gluon fusion dominates. The number of events expected is shown on the vertical scale on the right hand side of the graph. This implies that the discovery of the Higgs boson and the study of its properties is already possible at tens of fb^{-1} of data, corresponding to the first few years of physics runs at the LHC. Despite the fact that, at low Higgs mass, the cross section from gluon fusion is at least an order of magnitude higher than the other channels, the vector boson fusion (VBF) is an equally important production channel, since it creates two outgoing jets which can be tagged providing the characteristic signature of Higgs events. The characteristics of the VBF process are that the two outgoing jets are mainly in the forward direction, and that the hadronic activity is heavily suppressed in the central region. This is due to the absence of color exchange between the leading quark jets. The rapidity gap allows observation of the Higgs decay products in an isolated environment, and can also be used to distinguish VBF events from the background QCD processes which often generate central jets. The leading order cross section of Higgs production via vector boson fusion (VBF) was calculated by Cahn and Dawson[39]. The Higgs production cross section via VBF in the

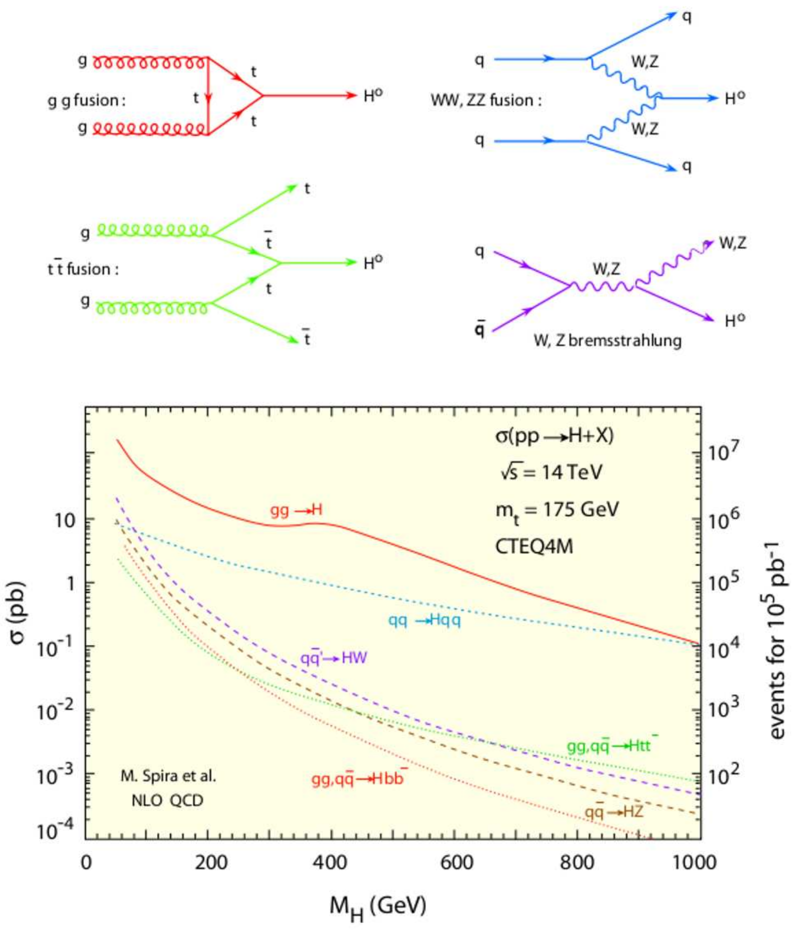

Figure 3.3: Up: Feynman graphs for Higgs boson production modes. Down: cross section for boson production modes as a function of M_H

centre of mass frame of the initial particles is given by:

$$\sigma \approx \frac{g^2}{16\sqrt{6}\pi^3 m_V^4}(C_1 + C_2)\log\left(\frac{\hat{s}}{m_H^2}\right),, \tag{3.1}$$

where $\hat{s}$is the incoming particles' center of mass energy squared, p_i and p_i' are the four-momentum of the incoming and outgoing quarks and k is the four-momentum of the Higgs boson, g is the electroweak coupling constant, m_v is the mass of the boson produced in the interaction, m_H is the Higgs boson mass and C_1 and C_2 are constant terms that can be written in terms of g, the weinberg angle and the higgs boson quantum numbers. Equation (3.1) shows that the cross section decreases with increasing mass of the Higgs boson; however, as shown in Figure (3.3) the cross section for the gluon fusion production drops more steeply, hence the VBF channel becomes particularly important when the Higgs boson mass is large.

3.2.2 Higgs decay channels

The decay channels for the Higgs boson are:

$H \rightarrow \bar{f}f$: fermion-antifermion pairs

$H \rightarrow \bar{V}V$ vector boson couples pairs

$H \rightarrow \gamma\gamma$ photon pairs

The total decay width of the Higgs boson as a function of its mass is shown in Figure (3.4, up). Below the threshold mass for $H \rightarrow ZZ$, $H \rightarrow WW$, the decay width is of the order of 10^{-3} GeV. In this region low values of the decay width provide a neat peak for the Higgs mass signal, making it easier to separate the signal from the dominant background events at those energies, which peak at the Z mass. However, a measurement of the Higgs lifetime ($\tau = 1/\Gamma$) requires a careful reconstruction of all the decay products and a precise knowledge of the uncertainties. On the other hand, a direct measurement of the lifetime is possible from the width of the reconstructed mass distribution if the Higgs mass is large. The branching ratio of the Higgs decay channels as a function of the Higgs mass is shown in Figure(3.4, down). Below the threshold $m_H = 2m_{W/Z}$, decays to the heaviest fermions have the largest branching ratio since $\Gamma_f \propto m_f^2$. A top quark pair is too massive to be produced in this range of the Higgs mass; however, a virtual top loop producing a gluon or a photon pair contributes to the total decay width. The $H \rightarrow \gamma\gamma$ channel is one of the most promising channels at the LHC despite

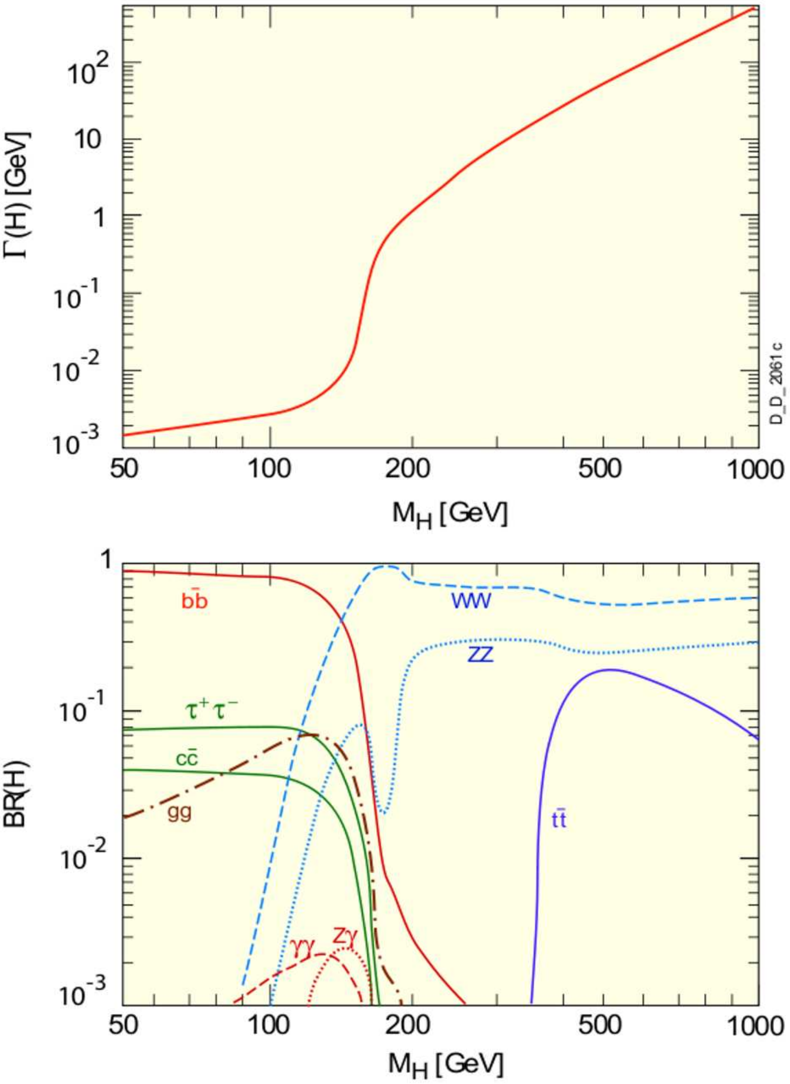

Figure 3.4: Up: total higgs production cross section as a function of M_H; Down: cross section as a function of M_H for each higgs decay mode

its relatively small branching ratio; a clean signature with two almost back-to-back photons can be observed with very little QCD backgrounds, and the CMS experiment has put an enormous effort in designing and building an excellent electromagnetic calorimeter to detect these photons with a good resolution. The heaviest lepton, τ, is also an important decay product since it further decays to another lepton or to a hadronic jet, which has distinct properties, and can be identified among QCD jets. A combination of this decay channel, $H \rightarrow \tau^+\tau^-$, with the VBF production process enables a successful suppression of the backgrounds from "lepton + jets" arising from W/Z production via QCD processes. If the Higgs boson is heavy enough to produce a vector boson pair, its decays to W^+W^- and ZZ start to dominate because their decay widths grow as $\propto m_H^3$. Although the branching ratio of $H \rightarrow W^+W^-$ is greater than the channel $H \rightarrow ZZ$ due to the factor of two difference from the electroweak Lagrangian, decays to Z are very promising due to their final states without neutrinos.

The $H \rightarrow \bar{f}f$ channel

Higgs boson decaying into a fermion anti-fermion pair illustrated by the Feynman diagram in Figure (3.4) and its lowest order partial can be written as:

$$\Gamma(H \rightarrow ff) = \frac{N_c G_F}{4\sqrt{2}\pi} m_H m_f^2 \left(1 - \frac{4m_f^2}{m_H^2}\right)^{3/2}, \tag{3.2}$$

where N_c is the number of color states, 3 for quarks and 1 for leptons and m_H, m_f are the masses of the Higgs boson and the fermion respectively. The term, $(m_f/m_H)^2$, suppresses decays into heavy fermions as the sum of their masses approaches the mass of the Higgs boson. At low Higgs masses ($m_H < 135$ GeV$/c^2$) the dominant decay channel is $b\bar{b}$, while the $t\bar{t}$ couples are too massive to be produced. High QCD background for $b\bar{b}$ events is the main problem Higgs search through this channel has to face.

The $H \rightarrow VV$ channel

The $H \rightarrow VV$ lowest order decay width can be written as:

$$\Gamma(H \rightarrow VV) = \frac{N_V G_F}{16\sqrt{2}\pi} m_H \left(1 - \frac{4m_V^2}{m_H^2}\right)^{1/2} \left(1 - \frac{4m_V^2}{m_H^2} + \frac{12m_V^4}{m_H^4}\right), \tag{3.3}$$

where $N_V = 2$ for $H \rightarrow W^+W^-$ and $N_V = 1$ for $H \rightarrow ZZ$. The other factors in the equation account for decays via virtual vector bosons below the threshold mass of the Higgs boson, $m_H = 2m_{W/Z}$.

The $H \rightarrow WW$ decay is dominant for $m_H > 135$ GeV/c^2. However, since neutrinos are undetected, reconstruction of Ws' four-momentum relies on missing transverse energy reconstruction and lepton or quark momentum measurement.

On the other hand, the $H \rightarrow ZZ$ decay is considered the "golden" channel for Higgs discovery. At about $130 < m_H < 180 GeV/c^2$ at least one of the produced Zs must be virtual (Z^*), and at $m_H > 2m_Z$ both Z bosons are real. While the $BR(H \rightarrow WW) \sim 3 \times BR(H \rightarrow ZZ)$, the Z channel compensates this with an overall better mass resolution (due mainly to the final state without neutrinos) and an excellent signal/background ratio[41].

The $H \rightarrow \gamma\gamma$ channel

Despite its low BR (about $2 \cdot 10^{-3}$), the $H \rightarrow \gamma\gamma$ channel[40] is of great interest for Higgs discovery in the low-mass scenario. If the back-to-back photon couples reconstruction is good, it is possible to have an excellent background rejection, resulting in a clean signal.

3.2.3 Theoretical limits on the Higgs mass

Although the Standard Model does not predict the mass of the Higgs boson, constraints on it can be deduced ftom theoretical arguments[42][43].

First, for the internal consistency of the Standard Model, the perturbation approach has to be valid. The processes mediated by the Higgs boson are needed to compensate for the increasing cross-section of the processes including longitudinally polarized W bosons. However, if $m_H \gtrsim 1$ TeV/c^2, the couplings in the W and Z boson sector become so large that perturbation theory fails before the process including the Higgs boson becomes effective. Therefore, the consistency requires an upper limit of $m_H \lesssim 1$ TeV.

Other bounds can be derived from the energy scale limit up to which the Standard Model can be extended. The Higgs potential has the form shown in (1.29):

$$V_0(\Phi) = \mu^2\Phi^\dagger\Phi + \lambda(\Phi^\dagger\Phi)^2.$$

Higher order loop corrections add a V_1 term, so that the potential becomes:

$$V(\Phi) = V_0(\Phi) + V_1(\Lambda, m_t, m_H, ...) \tag{3.4}$$

which modifies the potential. Λ is the renormalization scale which enters in the expression because of the loop corrections. The vacuum stability requires that the additional term should not destroy the shape of the potential function and the derivative of the potential should not become negative at high values of ϕ driving the potential function down below the original minimum. One requires the vacuum to be stable in the region $\phi < \Lambda$, i.e. the range where the theory must be valid. It means that the potential curve has an absolute minimum at $\phi^\dagger\phi = v^2/2$. The Higgs mass must therefore be high enough to keep the coefficient of $(\phi^\dagger\phi)^2$ positive even after the corrections. Thus the lower limit for the Higgs mass can be deduced. The Higgs potential written in terms of $\phi_0 = \frac{1}{\sqrt{2}}(v + H)$ becomes:

$$V(H) = -v^2\lambda H^2 + \lambda v H^3 + \frac{1}{4}\lambda H^4. \tag{3.5}$$

The quadratic Higgs self coupling $v^2\lambda H^2$ increases with the Higgs mass $(m_H = \sqrt{2\lambda}v)$ and there is a point where couplings diverge. The position of such a divergence depends on the Higgs mass and thus an upper limit for the mass can be deduced.

If the scale for Standard Model is unrealistically set to the Planck scale $(\Lambda = 10^{19} GeV)$, the Higgs mass limit are $130 - 190$ GeV/c^2. At the scale of $\Lambda \sim TeV$, the Higgs mass constraints are $55 - 700 GeV/c^2$. The allowed Higgs mass range as a function of the scale is shown in Figure (3.5).

Experimental limits on the Higgs mass

Searches for Higgs Boson follow two complementary routes:

1. direct search for Higgs boson evidence through its decay channels
2. tightening of indirect experimental constraints on the Higgs boson mass by measuring with high precision other parameters of the Standard Model

Searches for the Standard Model Higgs boson have been carried out at LEP[23] and studies are currently on-going at the Tevatron[44].

At LEP[45], the dominant production process was the W/Z associated channel; the e^+e^- collision events provided much lower level of hadronic activity compared to hadron colliders, which would have enabled observation of clear signatures from the Higgs and the vector boson decays. The centre of mass energy at LEP went up to a maximum of $\simeq 209$ GeV/c^2. At those energies, Higgs production was expected through a process of "Higgsstrahlung ", that is $e^+e^- \rightarrow H\,Z$ (Figure (3.6)) and the dominant Higgs decay channel was expected to be $H \rightarrow b\bar{b}$.

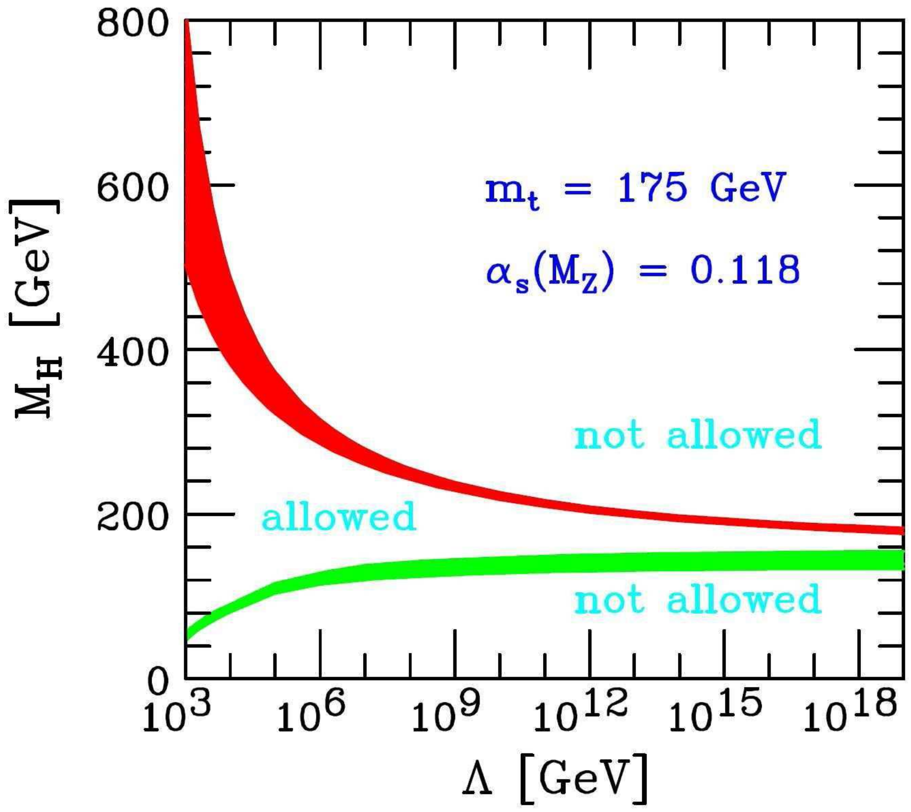

Figure 3.5: Theorethical bounds for the Higgs boson Mass in the Standard Model.

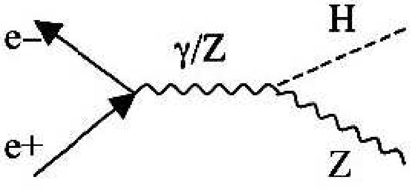

Figure 3.6: Feynman diagram for Higgsstrahlung process.

The combination of the results of the four direct Higgs searches at LEP lead to a lower exclusion limit on the Higgs mass of

$$m_H \geq 114.4 \text{ GeV}/c^2$$

at the 95% confidence level.
At Tevatron, where proton and anti-proton beams collide at 2 TeV, Gluon fusion has the highest production cross section; however, the same W/Z associated production is also important since tagging of b-jets from the dominant Higgs decay process can be carried out with better accuracy.
Although the Standard Model can accommodate a mass of the Higgs boson up to 1 TeV/c^2 (unitarity arguments), further constraints on the Higgs mass are set experimentally by comparing Standard Model parameter measurements with theoretical predictions. At tree level, the masses of the vector bosons are defined exactly as given in Equations (1.35, 1.39) and (1.37, 1.40), which involve only the two coupling constants and the Higgs vacuum expectation value; however, higher-order corrections to W and Z mass include contributions from virtual loops of the Higgs, as can be seen in Figure (3.7). Precision measurements of the W boson mass can be used to predict the contributions from the Higgs boson loops, while the top loop correction is currently the largest source of uncertainty on the Higgs mass. Using the direct measurements of the W boson mass at LEP of 80.410 ± 0.032 GeV/c^2 and the top quark mass at Tevatron of $172.7 \pm 2.9 GeV$ as well as the other

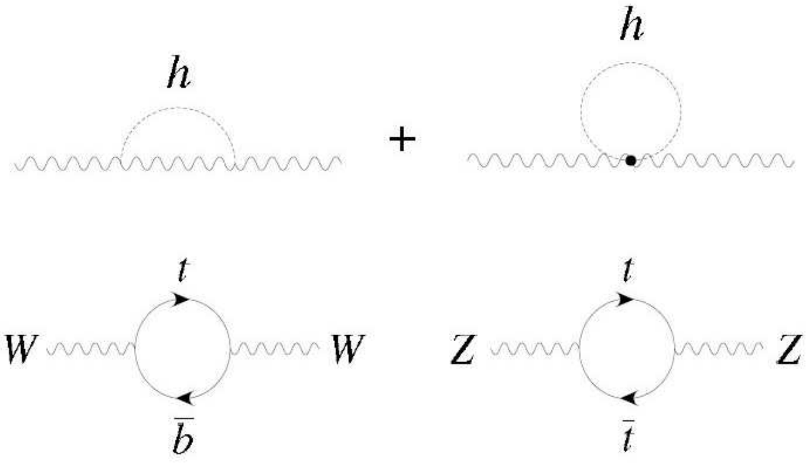

Figure 3.7: Diagrams for the higher order correction to the W and Z masses.

precise EW data, a prediction of the possible Higgs boson mass has been made, which is shown in dotted blue in Figure(3.8). Additional data from LHC in the coming years will give rise to more precise top and W mass measurements. Another constraint on the Higgs mass has been imposed by LEP

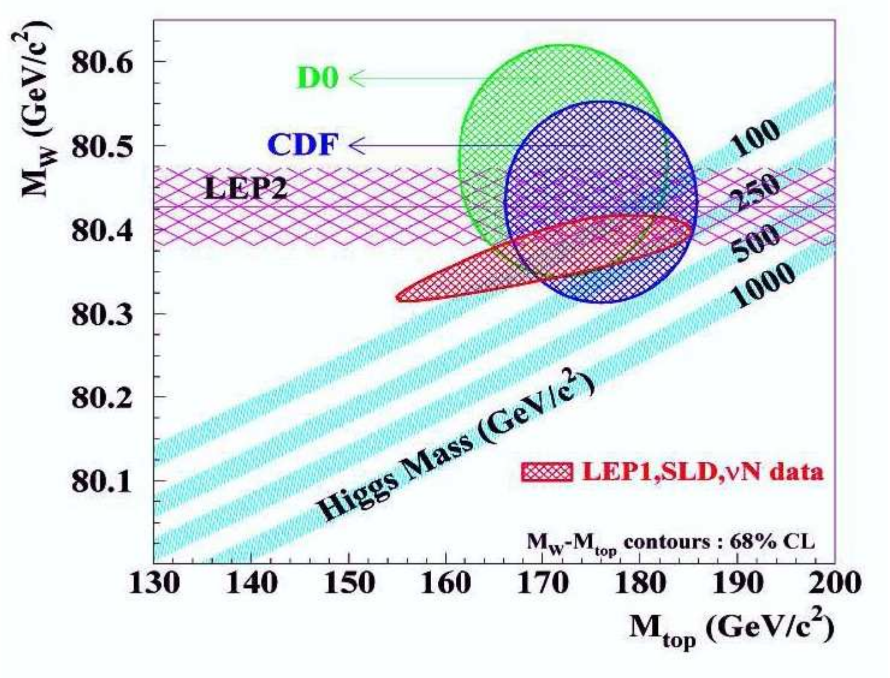

Figure 3.8: Constraints on the Higgs mass obtained from m_W and m_t precision measurements at various experiments at LEP and Tevatron.

Standard Model parameter measurements which depend on the Higgs mass. m_H can be extracted from a global fit of all of them. The results of LEP fit are shown in Figure (3.9), and the Higgs Mass from the fit is:

$$m_H = 89^{+38}_{-28} GeV/c^2$$

with an upper limit of 194 GeV/c^2 at the 95% confidence level.
All the mentioned results give strong indication for lower values of the Higgs boson mass.

3.3 Standard Model

The main goal for Standard Model physics is to describe three of the four fundamental interactions within the common formalism of quantum field the-

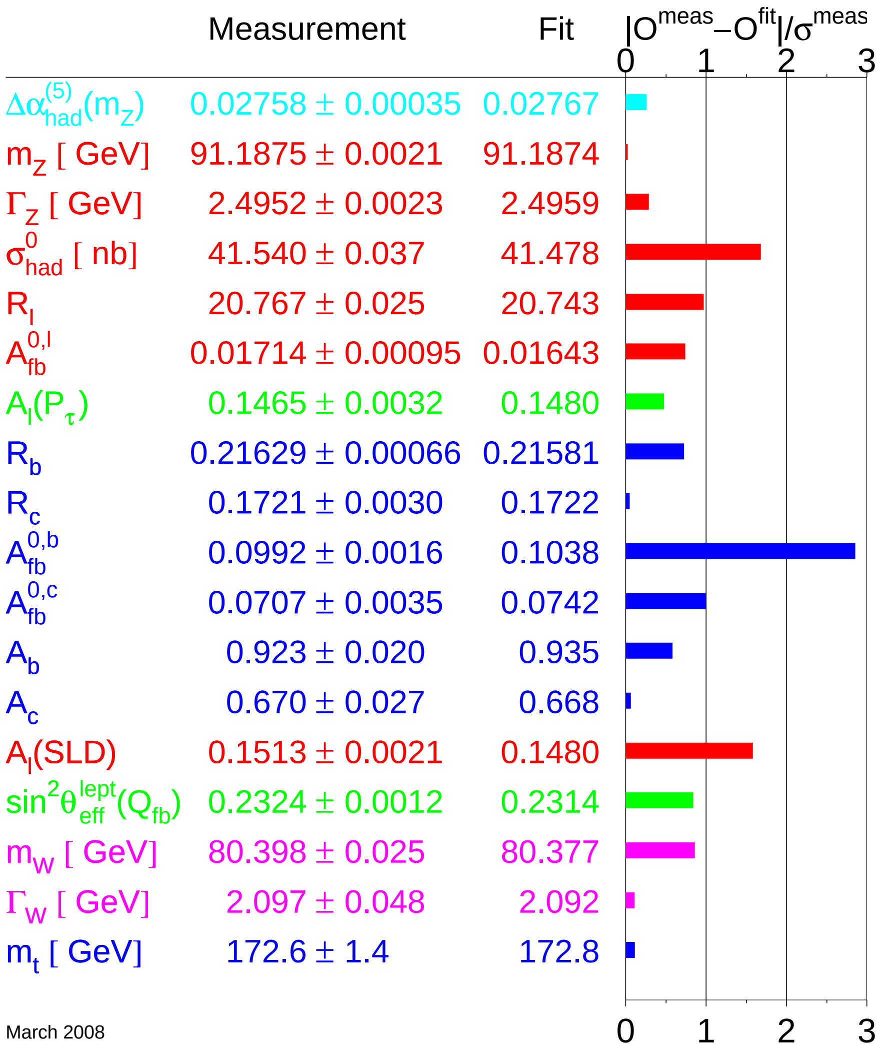

Figure 3.9: Simultaneous fit of all SM parameters at LEP.

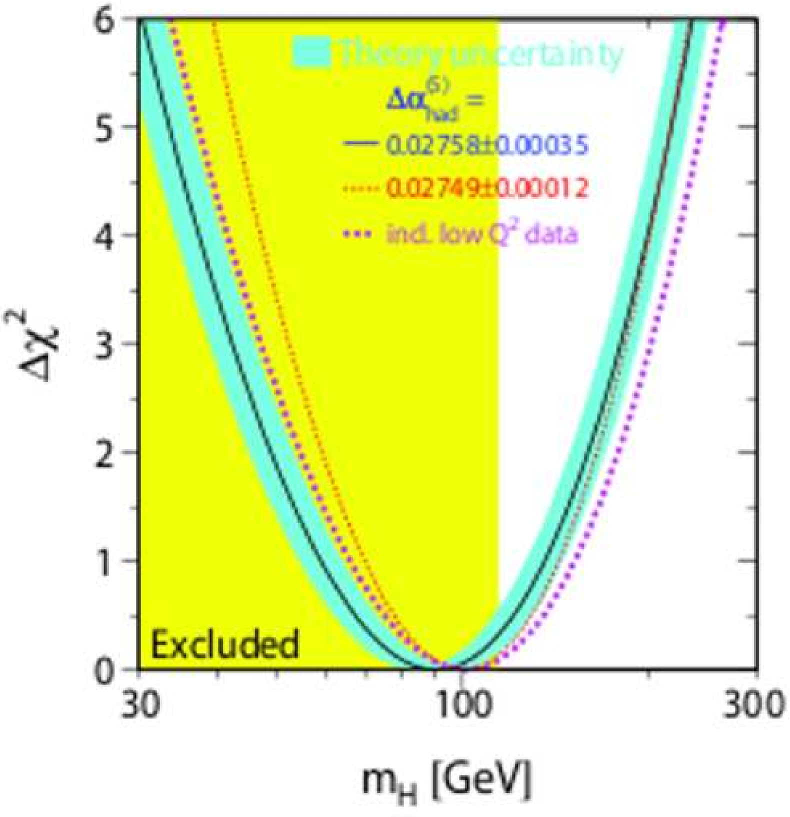

Figure 3.10: χ^2 of the simultaneous fit of all SM parameters as a function of M_H.

ory through the imposition of the gauge principle. Experimental results up to now are in excellent agreement with the Standard Model predictions. In particular, the electroweak sector of SM has been tested from the scale of few GeV up to Z[46] boson mass scale and even up to the t quark scale. Strong interactions are successfully described, at high energies, by the QCD theory, though the precision of the results is reduced because of the uncertainty on PDFs. Also, low energy processes cannot be treated with a perturbative approach in QCD because of the running strong coupling constant. LHC will provide a good test ground for Standard Model physics, since its high luminosity will result in abundant production of W, Z bosons and top quarks. Systematics uncertainties will in many cases be dominant over statistics uncertainties. A good estimation of M_W , M_t and θ_w is important for the Higgs sector, too: thanks to Higgs bosob and top quark corrections to the W mass one can tighten the constraints on the M_H itself. Evaluating QED radiative corrections to M_W, it can be written as:

$$m_W = \left(\frac{\alpha\pi}{G_F\sqrt{2}}\right)^{1/2} \cdot \frac{1}{\sin\theta_w \cdot \sqrt{1-\Delta R}}, \tag{3.6}$$

where ΔR is a corrective terms which depends from the top quark mass and the Higgs boson mass, α is the electromagnetic coupling constant and G_F is the Fermi constant. One can therefore use Equation 3.6 to determine the allowed range for the Higgs mass that is compatible with m_W, m_t and θ_w measurements, given that α and G_F are known with far greater accuracy.

3.3.1 B mesons physics

One of the four big LHC experiments is dedicated to it (LHCb,). At low luminosity ($L = 10^{33}\mathrm{cm}^{-2}\mathrm{s}^{-1}$), LHC is estimated to produce 10^{12} $b\bar{b}$ pairs in a year of data taking. Statistic for such process will be the highest ever achieved (see the CDF experiment at Fermilab). The LHCb experiment will study the different decay rates of B^0 meson to explore CP violation. Several channels can be taken into account for this studies. One can verify that $\Gamma(B^0 \to f) = \Gamma(\bar{B}^0 \to \bar{f})$, where f is a generic final state. Theorical predictions are very accurate for a particular class of those decays, i.e. those where the asymmetry rate A, defined as:

$$A = \frac{\Gamma(B^0 \to f) - \Gamma(\bar{B}^0 \to \bar{f})}{\Gamma(B^0 \to f) + \Gamma(\bar{B}^0 \to \bar{f})} \tag{3.7}$$

only depends on the phases of CKM matrix. A channel of interest is $B^0 \to J/\Psi K_s \to l^+l^-\pi^+\pi^-$, since the final state's characteristic signature, with two high p_T leptons.

3.3.2 Top quark physics

LHC's high luminosity values and high center of mass energy make it an ideal environment for $t\bar{t}$ production, so that it is often considered a t-factory: LHC can produce order of $10^8\, t\bar{t}$ couples every year. Top mass measurements are important to evaluate quantum mechanical corrections to Standard Model parameters, like the vector bosons masses, and to tighten the mass interval for Higgs boson. One of the most promising channel for top precision measurements is the $pp \to t\bar{t} \to l\nu b + jjb$, where j is a jet produced by a light quark (u, d, s, c). It is possible to obtain a precision in m_{top} measurement around $1 \div 2\mathrm{GeV}/c^2$[47].

3.4 Physics beyond Standard Model

The Standard Model provides a remarkably successful theory of physics at accelerators up to the currently explored energy scale. However, despite the outstanding agreement between theorical predictions and the experiment, many issues of modern particle physics are still not resolved inside the Standard Model :

Particle masses: the origin of particle masses is not fully understood. If masses are due to couplings with the Higgs boson, the nature of those couplings is purely phenomenological;

Unification: in SM there is not a simple group for unifying all known particle interactions;

Flavour: no reason is given why there are exactly 3 families of quarks and leptons and why weak interactions mixes them in the peculiar observed way;

Gravitation: at the energy scale of SM, a quantum theory for gravitation is not introduced. Quantum gravity effects are supposed to become relevant at the energy scale of Planck mass $m_P = (8\pi G_{\mathrm{Newton}})^{-1/2} \sim 2.4 \cdot 10^18$ GeV.

In order to solve those unanswered questions many theories have arised. Neverthless, the experimental frontier has advanced into the TeV range with no unambiguous hints of additional phenomena beyond the Standard Model. However, there is a 16 orders of magnitude range in energy between the presently explored range near the electroweak scale, m_W , and the Planck scale. Chances are high that new physics exists far before the Planck mass limit. Moreover, all cross-section evaluations performed within the Standard Model use a perturbative approach to matrix element calculations. Such an approach is supposed to fail at a certain energy scale, that is thought to be around a few TeV, beyond which no prediction can be made even within the SM. Theories Beyond Standard Models (BSM) include Supersymmetry theories, Great Unified Theories, extra dimensions, TeV scale Gravity and Technicolor theories. An important task for CMS and ATLAS will therefore be to search for BSM physics signatures. If low mass supersymmetry exists it will be within the reach of the LHC. The discovery reach for scenarios with extra dimensions, and new vector bosons high mass states are explored using several different experimental signals.

3.4.1 Supersymmetry

One of the most promising theories BSM is supersymmetry (SUSY)[48]. SUSY models predict new physics channels at the scale of energy explored at LHC, so the search for supersymmetry signatures will be an important task at CMS and ATLAS. SUSY is introduced to solve a problem of Standard Model known as the hierarchy problem. This is not a problem with the Standard Model at the current energy scale, but rather difficulty with the Higgs potential that occours as new BSM particles are introduced. The problem is that the Higgs mass term m_H^2 receives corrections from the virtual effects of every particle that couples to the Higgs field. If the Higgs field couples to a fermion f with a term in the Lagrangian $-\lambda_f$, then the Feynman diagram in Figure yields a correction Δm_H^2 to the Higgs mass:

$$\Delta m_H^2 = \left(\frac{\lambda_f}{16\pi^2}\right)\left[-2\Lambda_{UV}^2 + 6m_f^2 \ln\frac{\Lambda_{UV}}{m_f} + ...\right], \tag{3.8}$$

where Λ_{UV} is an ultraviolet momentum cutoff used to regulate the loop integral. Every particle that couples with the Higgs boson gives therefore a contribution to the Higgs mass term. However, both experimental and theoretical limits to the Higgs mass predict a value of $m_H \sim 100$GeV, with an upper limit of $m_H \lesssim 1$ TeV. If corrections to Higgs mass due to BSM particles are too large, it may significantly exceed the expected values. In order to obtain the sistematic cancellation of all Δm_H^2 terms, supersymmetry postules the existance of a new symmetry that associates bosons to fermions. The reason for this choice is that the signs of bosonic and fermionic loops corrections to Higgs mass are opposite, thus giving a hint that for each fermion a boson should exist and vice-versa. Particles associated this way are said supersymmetric partners, and they possess identical characteristics except for the spin. Each 1/2 spin fermion has a 0-spin particle, while 1-spin and

0-spin bosons are associated with 1/2 spin fermions. Quarks are associated to squarks, leptons to sleptons, W and Z bosons have *Winos* and *Zinos* as their partners. Figure (3.11) summarizes the SUSY partners of Standard Model particles. It is noteworthy that, since no supersymmetric particle has yet been observed, the masses of SM particles must differ from those of their supersymmetric partners. In order to preserve intrinsic consistency, Supersymmetry must therefore be spontaneously broken. Supersymmetry is searches at the LHC will revolve around inclusive studies based on large missing energy and jets[30]. Typical SUSY signatures are squarks and gluinos decays. If the squarks and/or gluinos are kinematically accessible at the LHC, they are expected to have large production rates. The cross sections for the production of a squark or a gluino at the LHC are displayed in Figure (3.12). Both squarks and gluinos have cascade decays into neutralinos, producing jets and leptons in the final state (see Figure 3.13). Since light neutralinos χ_1^0 don't interact with the detector, a typical supersymmetry signature includes large $\not{E}_T$ Since final state of many SUSY signatures include high energy leptons and jets, processes such inclusive $pp \to Z/W$ and $pp \to Z/W + jets$ are the Standard Model background for SUSY events.

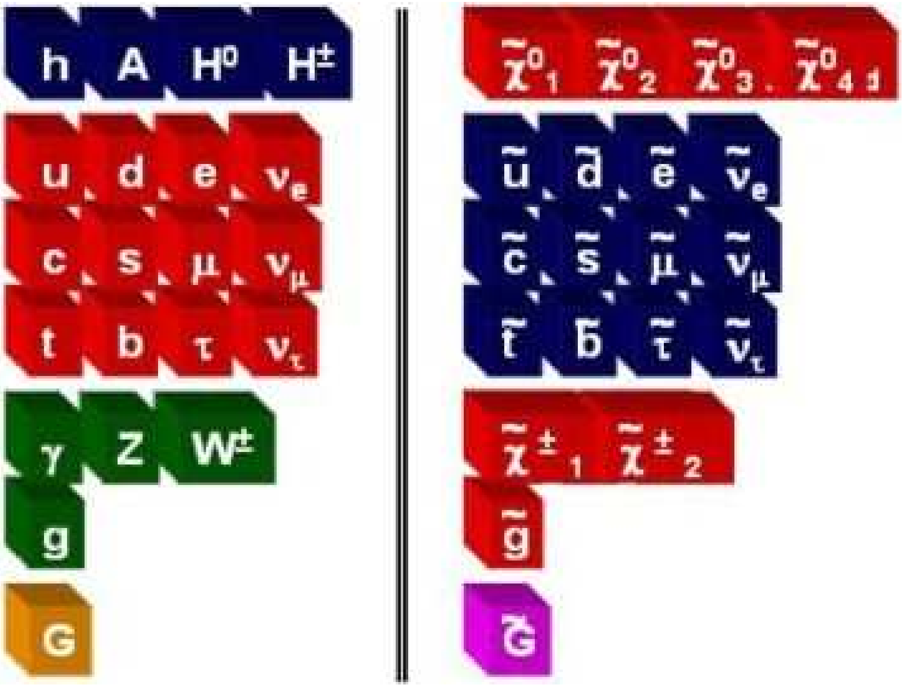

Figure 3.11: Supersymmetric partners of Standard Model particles.

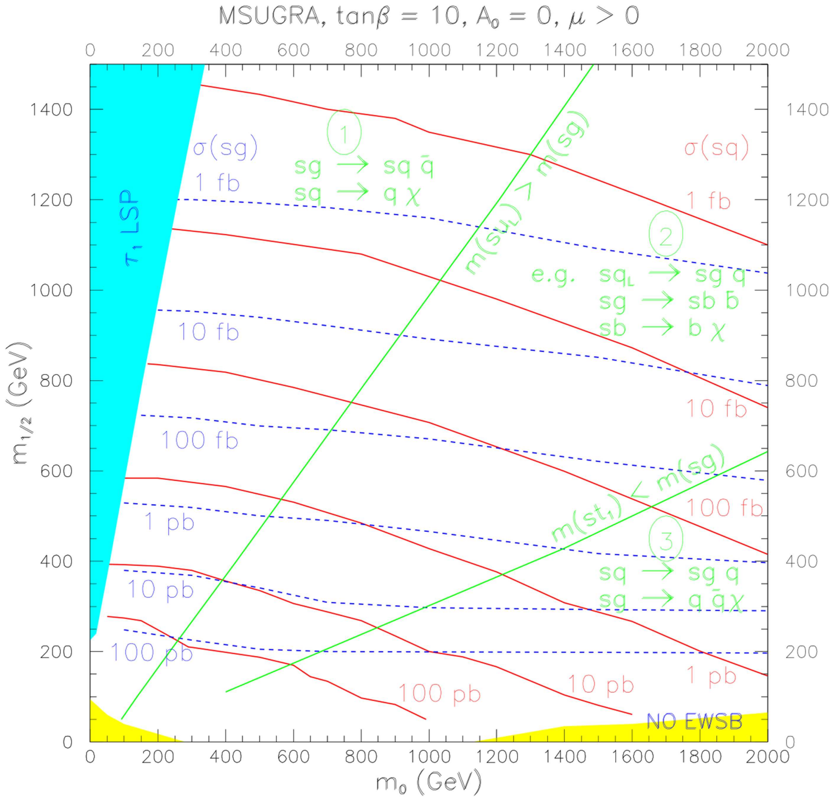

Figure 3.12: Supersymmetric particles branching ratios.

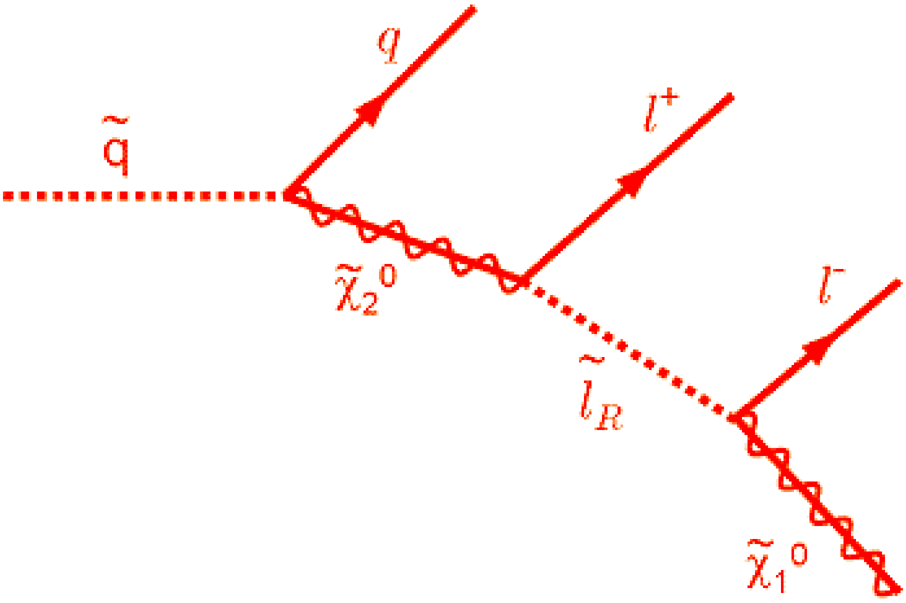

Figure 3.13: The decay cascade of an squark.

3.4.2 Extra dimensions and heavy Vector Bosons states

The theoretical and phenomenological landscape of beyond the standard model searches extends to a multitude of exotic tendencies today in collider physics. Most are conceived within one kind or another of extra dimensions and supersymmetric scenarios. The strict or loose dualities between different frameworks for physics "beyond the standard model" have a direct experimental consequence: the final states and signatures of the models are very similar. This renders the characterisation of an excess or a deviation a fine and probably long challenge.

Models with heavy vector bosons

Additional heavy neutral gauge bosons (Z)[50] are predicted in many superstring-inspired[51] and grand unified theories (GUTs), as well as in dynamical symmetry breaking[52] and "little Higgs"[53] models. There are no reliable theoretical predictions, however, of the Z mass scale. The LHC offers the opportunity to search for Z bosons in a mass range significantly larger than 1 TeV/c^2. Many models representative of a broad class of extra gauge bosons are took into account at CMS:

- Z_{SSM}, defined within the Sequential Standard Model (SSM), which has the same couplings as the Standard Model Z

- Z_{ψ}, Z_{η} and Z_{χ}, arising in E_6 and $SO(10)$ GUT groups with couplings to quarks and leptons as derived in Refs. [95, 96].
- Z_{LRM} and Z_{ALRM}, arising in the framework of the so-called "left-right" [97] and "alternative left-right" [91, 92] models with couplings as derived in Ref. [91, 92]

Randall-Sundrum extra dimensions

Randall-Sundrum refers to a class of scenarios, also known as warped extra dimensions mod- els, originated by Lisa Randall and Raman Sundrum[**?**]. In these scenarios there is one extra spatial dimension, and the five-dimensional geometry is "warped" by the presence of one or more branes. The branes extend infinitely in the usual three spatial dimensions, but are sufficiently thin in the warped direction that their profiles are well-approximated by delta functions in the energy regime of interest.

3.4.3 Technicolor models

Technicolour (TC) provides an alternative to the elementary Higgs mechanism of the Standard Model. It introduces a new strong interaction [54]providing a dynamical nature to Electroweak Symmetry Breaking. Technicolour is a QCD-like force, acting on technifermi-ons at an energy scale$\Lambda_T \approx 246$ GeV. TC theory predicts that the Higgs Boson is a fermion condensate . A number ND of technifermion doublet condensates yield the pseudo-Goldstone bosons π_TC , together with a wide spectroscopy of excited technimesons, like ρ_{TC} and ω_{TC}. The main discovery channel for Technicolor at CMS will be $\rho_{TC} \to W + z$

Chapter 4

Production of Z + Jets

The analysis of the $pp \rightarrow Z + n$ jets $\rightarrow \mu^+\mu^- + n$ jets channel was performed on fully simulated and reconstructed events.

The present chapter describes all the steps that go from the event generation to the production of a dataset for offline analysis.

The physics process and the detectors' responses are simulated by Monte Carlo (MC) generators. Informations from sub-detectors are then combined to identify physics objects in the final state. The data are therefore stored in one of the different formats available in CMS. The chosen format depends on the informations required for offline analysis and on the physical disk space available.

The first part of the present chapter gives an overview of the MC simulation tools for physics processes at CMS. The Monte Carlo "simulation chain" starts from the pp collision and simulates the subsequent physics processes, the interactions of particles with the detector and the response of the readout electronics.

The second part of the chapter explains the strategies for identification of physics objects adopted in CMS and the reconstruction algorithms implemented.

The last part of the chapter describes the main data formats used for offline analysis in CMS.

4.1 The simulation chain

The complete Monte Carlo simulation of an event at CMS is separated into three steps :

- Generation of the physics processes: input for the simulation, to be produced by a specified event generator source, such as particle gun or

Pythia [55], in the same chain with detector simulation or further, or to be read from an external file.

- Simulation: Geant4[56] based simulation of the physics processes occurring when particles pass through the hierarchy of volumes and materials that compose the CMS detector, and of the sub-detectors responses (simulated hits).
- Digitization: simulation of the electronics response to the hits in the detector

4.2 Event generation

CMS simulations include the production of complete pp events generated with Monte Carlo methods. High-energy particles collisions give rise to complex final states, with large multiplicities of hadrons, leptons, photons and neutrinos. The complexity of such events is mastered by a subdivision of the full problem into a set of simpler separate tasks:

Hard processes The cross section for a process $ij \rightarrow k$ involving two partons i, j from two different beam particles forming a final state k can be written as:

$$\sigma_{(ij\rightarrow k)} = \int dx_1 \int dx_2 f_{i,1}(x_1, Q^2) f_{j,2}(x_2, Q^2) \hat{\sigma}_{(ij\rightarrow k)}.$$

Here $\hat{\sigma}$ is the cross section for the hard partonic process, as codified in the matrix elements for each specific process. For processes with more than one particle in the final state, k would be replaced by an integral over the allowed final-state phase space. The $f_{i,a}(x_a, Q^2)$ are parton-distribution functions, which describe the probability to find a parton i inside the beam particle a, with parton i carrying a fraction x_a of the total a momentum. Parton distributions also depend on the momentum scale Q^2 of the process.

Parton showers QCD radiation is produced from colored particles and results in showers of partons (gluons and quarks). Such radiation is divided into initial and final state radiation. An $e^+e^- \rightarrow Z \rightarrow q\bar{q}$ process would only contain final state radiation, while a $q\bar{q} \rightarrow Z \rightarrow e^+e^-$ process would only contain initial state radiation. LHC processes always present initial state radiation because of the hadronic nature of collisions, while parton showers produced from final state partons contribute to the formation of hard jets with high transverse momentum.

The evolution of final state showers is parametrized in terms of the originary parton's kinematic variables (e.g. the Q^2 scale or the p_T).

Hadronization A number of phenomenological models for the binding of partons into color singlets exist, usually distinguished into three main models, string fragmentation (SF), independent fragmentation (IF) and cluster fragmentation (CF), but many variants and hybrids exist. None of them can lay claims to be "correct", although some of them may be better founded than others. The best that can be aimed for a model is internal consistency, a good representation of existing data, and a predictive power for properties not yet studied or results at higher energies. For quark-antiquark pairs, QCD studies lend support to a linear confinement picture, i.e. the energy stored in the colour dipole field between a charge and an anticharge increases linearly with the separation between the charges. The assumption of linear confinement provides the starting point for the string model, used for instance in PYTHIA.

Underlying Event Fragments of beam protons not involved in the hard collisions produce parton-showers that hadronize after hard collisions, contributing to the Underlying Event. For each beam a particle coming from initial-state radiation is chosen by the reconstruction algorithms to be a shower initiator. The 4-momentum is then divided between the shower initiators and the rest of pp fragments.

Decays A large fraction of the particles produced by fragmentation are unstable and subsequently decay into stable (or almost stable) ones. It is therefore important to include all particles mass distributions and decay properties. Usually it is assumed that decay products are distributed according to phase space, i.e. that there is no dynamics involved in their relative distribution. However, in many cases additional assumptions are needed, e.g. for semileptonic decays of charm and bottom hadrons one needs to include the proper weak matrix elements.

All main aspects of the events are simulated, such as hard-process selection, initial and final-state radiation, beam remnants, fragmentation, decays, and so on. Therefore events should be directly comparable with experimentally observable ones. Many different event generators capable of simulating all the stages of a physics process are used in CMS. Examples are PYTHIA ([55]), SHERPA ([57]) or HERWIG ([58]). Those generators use different approximations or models for the different stages of the event. Many other generators are designed and optimized for a specific category of processes, like ALPGEN ([59]) which is dedicated to the study of multiparton hard processes in hadronic collisions. There are also simpler generators that produce individual particles. These are called generically particle guns, and are particularly useful for tests. General purpose generators are often combined with specific packages to simulate specific processes. As an example the flow of an event generation for PYTHIA is described: it starts with the generation of a "process" that decides the nature of the event. Often it would be a "hard process", such as $gg \to h \to ZZ \to l^+l^-l^+l^-$, that is calculated in perturbation theory. Only a very small set of partons/particles is defined at this level, so only the main aspects of the event structure are covered. The next step is the generation of all subsequent activity on the partonic level, involving initial and final-state radiation, multiple parton-parton interactions and the structure of beam remnants. At the end of this step, a realistic partonic structure has been obtained, e.g. with broadened jets and an underlying-event activity. The last part involves the hadronisation of the partons by string fragmentation, followed by the decays of the unstable particles. This part is almost completely nonperturbative, and so requires extensive modelling and tuning or, especially for decays, parametrisations of existing data. It is only at the end of this step that realistic events are available, as they could be observed by a detector. Informations on generated particles are also accessible for offline analysis. The generation algorithms of PYTHIA can be invoked inside of the CMS software framework (CMSSW)[60].

4.2.1 Simulation and digitization

The interactions of the particles with the detector elements as well as the dead materials are simulated and interpreted in terms of signal output from the front-end electronics (digis). This procedure is carried out in with software packages present in CMSSW. Multiple p-p collision events are included in order to create a pile-up environment. This step is based on the GEANT4 package.

4.2.2 Particles and physics objects in the CMS software framework

4.3 The events reconstruction

Reconstruction algorithms collect the readout digis from the sub-detectors to create complex physics objects like tracks, electromagnetic or hadronic showers.

Informations from one or more detectors are combined together to correctly identify physics objects like electrons, photons, muons, hadronic showers etc. and to evaluate the related kinematic observables. All reconstructed objects are stored into collections with other objects of the same type. All algorithms run inside the same framework used for analysis.

4.3.1 Electron and photon reconstruction

An electron shower deposits its energy in several crystals of the ECAL[61]. Approximately 94% of the incident energy of a single electron is contained in 3×3 crystals, and 97% in 5×5 crystals. The spread energy of photons and electrons is clustered by building a cluster of clusters ("supercluster"), which is extended in ϕ. This algorithm is called the "Island algoriythm". It starts by a search for cluster seeds, which are defined as crystals with an energy above a certain threshold. Starting from the seed position, adjacent crystals are examined, scanning first in η and then in ϕ. Along each scan line, crystals are added to the cluster until a rise in energy or a crystal that has not been read out is encountered. In much the same way as energy is clustered at the level of calorimeter cells or crystals, non overlapping island clusters can in turn be clustered into superclusters. The procedure is seeded by searching for the most energetic cluster and then collecting all the other nearby clusters in a very narrow η-window, and a much wider ϕ-window. For electrons the reconstruction continues in the Inner Tracker, as this procedure drives the finding of track hits ("seed") in the Inner Tracker. Figure (4.3) shows the electron energy resolution for different electron categories.

4.3.2 Track reconstruction

Tracks physics objects are reconstructed in the position sensitive detectors[62]. The hits from the detectors are analyzed using a pattern recognition algorithm to associate the measurements with trajectories. The sequence leading from measured hits to tracks does not depend from the sub-detector and occurs in four stages:

- Seeding: two or three close hits must be identified as a track segment.
- Trajectory building: Starting from the track segment, compatible hits in subsequent detector layers are identified in the direction specified by the seed.
- Trajectory cleaning: the trajectory building produces a large number of trajectories, many of which share a large fraction of their hits. In the

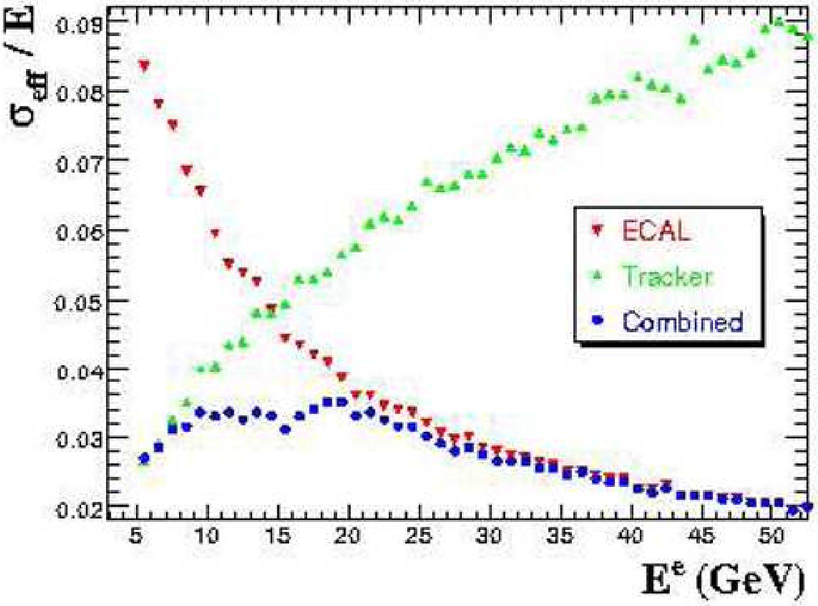

Figure 4.1: The energy resolution of the electrons as a function of E_e for Ecal superclusters (red), tracks (green) and combined measurements (blue).

cleaning stage, ambiguities among the possible trajectories are solved and a maximum number of track candidates are kept.

- Trajectory smoothing: A backward fitting is performed, using the Kalman Filter to increase precision in track parameter measurements

The reconstructed track is a helix, depending on five parameters: x, y, z, λ and p. x, y, z, are the coordinates of a point of the trajectory in space, λ is the angle of the tangent vector to the trajectory with respect to the B magnetic field, and p is the module of the particle 3-momentum evaluated in the x, y, z point.

4.3.3 Muon reconstruction

One of CMS main features is its ability to trigger on, and to reconstruct muons with high efficiency.
Information from all the detectors in the Muon System is used in muon reconstruction, while the RPCs are also used for triggering over muons[63].
The central tracker also plays an important role in the muons track and momentum measurements, since the spatial resolution of tracker hits is better than MS by an order of magnitude.
The muons reconstruction is performed in three stages:

- local reconstruction.
- standalone reconstruction.
- global-muon reconstruction.

Local muon reconstruction

Local muon reconstruction uses digis from muon chambers to reconstruct a track segment. In DT chambers the digis are drift times measured with Time Digital Converters (TDC). Position in DT chambers is a function of drift times and of the magnetic field B. After the reconstruction of the hits position, a pattern recognition algorithm reconstructs line segments from consecutive hits that point towards the nominal vertex, fitting the segment hits to a line in space. Segments with number of hits > 3 and $\chi^2/ndf < 20$ are kept (chi squared per number of degrees of freedom). In CSCs the digis are charge deposits on cathode strips and anode wires. Position of hits is obtained with the mean of the cathode strip position weighted by the charge deposit on it. The resolution of muons p_T is shown in Figure (2.5)

StandAlone muon reconstruction

Standalone muons are reconstructed combining information from DT/CSC and RPCs. The track reconstruction proceeds using the standard tracking procedure as explained in Section4.3.2, where the seeds are the track segments obtained through local reconstruction in DT and CSC. The reconstruction of the tracks uses also the hits in RPCs, even if the spacial resolution is worse than CSC and DT by a factor 4-5.

Global muon reconstruction

The global muon reconstruction is performed extending the standalone muon track from the innermost chamber of the Muon System to the outer section of the tracker, considering effects of muon propagation through the material. Once the intersection point of the trajectory with the tracker is obtained and the parameters of the muons have been evaluated through backward propagation, a seed consisting of two points in the tracker compatible with the track extension is searched for. Tracking algorithms are therefore applied to the new seed to reconstruct the muon track inside the detector. For global reconstruction, however, the smoothing procedure uses all hits both in the Inner Tracker and in the Muon System.

Muon isolation

In the p_T range of $10 \div 30$ GeV/c, the contribution of muons from b and c quarks decay is relevant. At lower p_T values, K and π decays contribution dominate, while for $p_T > 30$ GeV/c, muons from Z and W processes dominate. Isolation is a variable introduced to discriminate muons produced inside the jets and muons coming from heavy particles decays. Isolation algorithms consider the energy deposit in a cone around the muon. The axis of the cone is usually identified as the axis of the muon direction. The cone is defined by the condition $\Delta R < \Delta R_{Max}$, with $\Delta R = \sqrt{(\Delta\eta)^2 + (\Delta\phi)^2}$, where $\Delta\eta$ and $\Delta\phi$ are the distances in pseudorapidity and polar angle from the muon axis. The isolation can be defined with respect to the p_T or E_T of the objects measured in a detector within the isolation cone. A veto cone inside the isolation cone is defined in order to exclude the energy deposit of muon itself.

4.3.4 Jet reconstruction

Due to the increase of the strong coupling constant at small energies, the perturbative evolution of the parton shower eventually has to be followed by

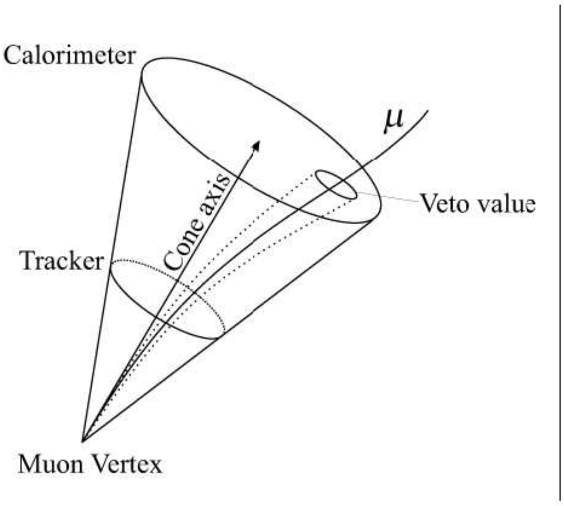

Figure 4.2: Schematic illustration of the Isolation cone. The energy deposit is computed in the isolation cone, the muon deposit is removed by excluding a small area around the muon (the so-called veto cone).

the non-perturbative description of fragmentation or hadronization of partons into jets of color-neutral hadrons.
In all the physics processes, like $Z + jets$ production, characterized by a topology which contains quarks in the final state of pp collisions at the LHC, the jets reconstruction plays a role of major importance to reconstruct the quarks kinematics.
The association of measured energy clusters with the scattered partons is a complex problem[65] because of the multitude of physics and detector effects that needs to be accounted for: gluon radiation, Underlying Event, pile-up and noise contributions, uncertainties in jet-fragmentation models, out of-cone showering, loss of low momentum charged particles due to the magnetic field, energy loss due to dead material and so on. In general the ambiguities in the jet definition arising from the experimental problematics can be divided in: jet clusters algorithms [64]and sub-detector response. Of course, some problems arise also from the theorethical point of view if higher order corrections are taken into account. Figure (2.15) shows the resolution of jets reconstructed in the HCAL.

Jet clustering

When a quark or gluon fragments into a jet, the produced hadrons are collimated in the direction of the initial parton due to its high boost. Therefore, a straightforward method to reconstruct jets is to cluster energy deposits in a cone whose direction is associated to the parton initial direction. These cones are described in the η, ϕ plane using this metric:

$$\Delta R = \sqrt{(\Delta\eta)^2 + (\Delta\phi)^2} \tag{4.1}$$

Readout cells in the Calorimeters are arranged in a tower pattern in η, ϕ space, projective to the nominal interaction point. Three principal jets reconstruction algorithms have been coded and studied in CMS:

The iterative cone: the algorithm starts by ordering the input ojects according to decreasing E_T. The first object in the list is taken as jet seed, provided it exceeds a specified seed threshold. A so-called proto-jet is constructed by clustering objects in a given cone around the seed. The direction of this proto-jet is used as a new seed, and this procedure is iterated until the energy and the direction of the proto-jet stabilizes. The proto-jet is therefore added to the list of jets and the objects in the proto-jet are deleted from the list of input object. The whole procedure is then repeated until no more input objects are found exceeding the seed threshold. The jet cone size and the seed threshold are the algorithm's parameters.

The midpoint cone: the algorithm has been designed to improve the treatment of overlapping jets. It uses the same procedure as the iterative cone algorithm to find proto-jets, but in contrast no input objects are removed from the list of seeds. Once all proto-jets are constructed, the momenta of pairs of overlapping proto-jets are combined into so-called midpoints, which serve as additional seeds for new proto-jets. On all the obtained proto-jets, a splitting and merging procedure is applied, starting with the highest E_T proto-jet. This proto-jet becomes a jet if no input objects are shared with other proto-jets. Otherwise a comparison is made between the shared transverse energy with the highest E_T neighbor and the total E_T of this proto-jet. If this fraction is larger than a given value, tipically 50%, the proto-jets are merged, otherwise the common objects are assigned depending on which of the two proto-jets is the closest. This procedure is repeated, always starting from the highest E_T proto-jet until no proto-jets are left. This algorithm has as parameters the jet cone size, the seed threshold, the threshold on the shared energy fraction for jet-merging, and also a maximum of number of proto-jets used to generate midpoints.

The inclusive k_T: the algorithm implemented[66] for CMS calculates for each input object i and each pair (i, j) the quantities:

$$d_i = E_{T,i}^2 R^2 \,\text{and}\, d_{i,j} = min\left\{E_{T,i}^2 E_{T,j}^2 \Delta R_{i,j}^2\right\}, \tag{4.2}$$

where R is a dimensionless parameter, and ΔR is the metric defined in 4.1. An iterative procedure searches the smallest value of all the d_i and $d_{i,j}$ over all objects and pairs. If a $d_{i,j}$ type value is the smallest one, the objects i and j are removed, and merged into a new input object. If a d_i value is the smallest one, the input object i is added to the list of found jets, and deleted from the input list. When all input objects are transformed into jets, a new iteration merges all jets i and j with distance $\Delta R_{i,j} < R$. It follows that $\Delta R_{i,j} < R$ for all i and j and hence R can be interpreted as the equivalent parameter of the jet cone size fore the cone-based algorithms.

The midpoint and k_T algorithms[67] are widely used in offline analysis in current hadron collider experiments, while the iterative cone is simpler and faster and commonly used for jet reconstruction in software based trigger systems, as well as in this analysis.

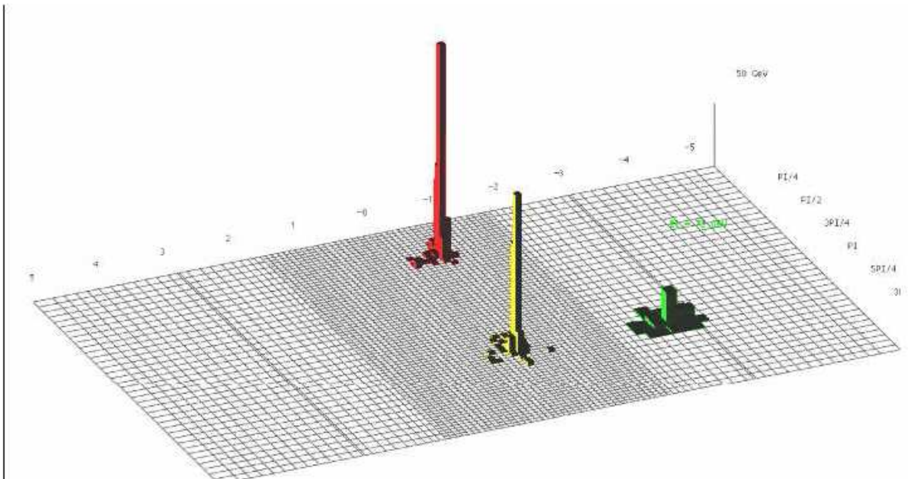

Figure 4.3: The HCAL segmentation with three reconstructed jets.

4.4 CMS data formats

Event Data Model(EDM) adopted at CMS uses three different data formats for an event, each containing different informations:

FEVT(Full EVenT): it includes all informations on an event, including "raw" data. An event in the FEVT format occupies $\sim 1-3$ MB.

RECO(RECOnstructed data): it includes all informations from the reconstruction of the events.An event in the RECO format occupies ~ 500 kB.

AOD(Analysis Object Data): it includes only high level reconstructed events. An event in the AOD format occupies ~ 50 kB.

Chapter 5

Study of the $Z + \text{jets} \rightarrow \mu^+\mu^- + \text{jets}$ channel

This chapter describes the performed study of the $pp \rightarrow Z + n\,\text{jets} \rightarrow \mu^+\mu^- + n\,\text{jets}$ channel.
The study was performed on Monte Carlo (MC) samples of signal and background events . A study on the jet multiplicity is made, and events with different number of reconstructed jets are separated and treated as independent categories. A procedure to subtract the background from the data is therefore applied on channels with number of jets $n =$ 1, 2, 3. Such procedure is data-driven, in the sense that it does not depend on informations from the simulation chain, and can be applied directly on the data at the LHC startup.

5.1 Analyzed data samples

The analyzed events are stored in an AODSIM format dataset which is part of the official CSA07[1] production. The detector response is reproduced through the entire generation-simulation-digitization chain and physics objects are reconstructed starting from the digis in the detector. The data sample contains informations on all particles produced through each step of the Monte Carlo simulation and on the reconstructed objects. We have considered the following background events for the $Z(\mu^+\mu^-)+$ jets background: W, $t\bar{t}$, $Z \rightarrow e^+e^-$ and $Z \rightarrow \tau^+\tau^-$.

---

[1] The CSA07 (Computing Software and Analysis Challenge 2007) is an official CMS production. CSA07 data consist of more than 150M events of various Standard Model processes. See also [69]

Table 5.1: Information on generated sample

Process	Cross section (lepton channels only for Z and W) (pb)
$Z + 0$ jets	4400
$Z + 1$ jet	965
$Z + 2$ jets	299
$Z + 3$ jets	81
$Z + 4$ jets	18.3
$Z + 5$ jets	13.7
$W + 0$ jets	45000
$W + 1$ jet	9450
$W + 2$ jets	2725
$W + 3$ jets	690
$W(\mu^+\nu) + 4$ jets	165
$W(\mu^+\nu) + 5$ jets	125
$t\bar{t} + 0$ jets	619
$t\bar{t} + 1$ jet	176
$t\bar{t} + 2$ jets	34
$t\bar{t} + 3$ jets	6
$t\bar{t} + 4$ jets	1.5
$t\bar{t} + 5$ jets	400

The generated physics processes in the sample therefore include:

- $pp \to Z + n\,\text{jets} \to l^+l^- + n\,\text{jets}$
- $pp \to W + n\,\text{jets} \to l^\pm\nu + n\,\text{jets}$
- $pp \to t\bar{t}$.

where $l = e, \mu, \tau$.

Generation of the matrix element uses the ALPGEN algorithms, which are optimized for cross section evaluation of hard processes with multiple partons in the final state, while parton showering and hadronization are simulated through PYTHIA algorithms. Table (5.1) report values of cross section of all the processes. The equivalent luminosity for the entire sample has been scaled to 10 pb^{-1}.

5.2 Analysis strategy

The selected $Z + n\,\text{jets} \rightarrow \mu^+\mu^- + n\,\text{jets}$ events request a pair of muons with opposite charge reconstructed through both the tracker and the muon systemS ("GlobalMuons") and a number of jets N reconstructed in the Calorimeters.

In order to reject background events that contain two muons, cuts on muons and jets kinematic variables are applied. The remaining background is subtracted with a method based on the fit for the invariant mass distribution of $\mu^+\mu^-$ pairs . The validation of the subtraction procedure has been done through a comparison with the Monte Carlo truth.

5.3 Physics objects

Muons and jets p_T and η, are the physical observables considered for signal selection and analysis purposes. The invariant mass of $\mu^+\mu^-$ pairs is also considered in this analysis. In a pure signal (no background) scenario the observed invariant mass distribution of muon pairs should result approximately in a Breit-Wigner distribution in the proximity of Z mass peak[2]. The jet multiplicity in an event is an important observable, since it is used for studies of the multi-parton processes ratios.

5.3.1 Jets

Jets are reconstructed through energy release in the Calorimeters by hadronic showers. In order to identify an hadronic shower as a jet, an operative definition is required. Jet Clustering algorithms described in Section (4.3.4) provide good operative definitions for jets, and they can be applied on calorimetric clusters as well as on MC generated particles. The clustering Iterative-Cone algorithm is applied on the calorimetric clusters in order to reconstruct commonly called CaloJets. Jets reconstructed from Monte Carlo generated particles are called GenJets. The latter are interpreted as the equivalent of Monte Carlo truth for jets, meaning that GenJets are the jets that would be reconstructed in the "ideal" detector.

Since clustering algorithms don't filter hadrons coming from the Underlying Event, a great number (order of 60) of low energy, high η jets is reconstructed

---

[2] The parton Distribution Functions distort the pure Breit-Wigner as well as energy loss for final state radiation. For the complete model used for the Z mass signal see chapter(5.4.1)

for each event. High-p_T jets coming from a $Z + n\,\text{jets} \rightarrow \mu^+\mu^- + n\,\text{jets}$ process must be separated from the Underlying Event jets. Cuts on kinematic variables p_T and η are imposed (Table 5.2). Several possibilities were considered for p_T requirements, and in the end a treshold on $p_T > 30$ GeV/c was imposed. Detailes on p_T and η distributions for the final choice of the p_T threshold are shown in Figure (5.1).

Table 5.2: Kinematic cuts on jets variables

Performed cuts:
$p_{T,Jets} > 30$ GeV/c
$\lvert\eta_{Jets}\rvert < 3$ GeV/c

The jet multiplicity for reconstructed and MC jets is shown in Figure(5.2).

GenJets multiplicity is compared to CaloJets multiplicity in order to have a comparison between signal and the Monte Carlo. Figure (5.3) shows the number of GenJets vs number of CaloJets: in the ideal case the two variables would have a correlation coefficient[3] $\rho = 1$. Energy reconstruction inefficiencies cause CaloJets to have a lower reconstructed p_T than GenJets. This results in events where a GenJet survives the kinematic cut but a CaloJet is rejected. This is one of the reasons for the different population of the regions above and under the diagonal line of the plot.

Leading Partons definition and Jet-parton matching problem

Strong interactions are responsible for jet formation. A jet is the product of the fragmentation of partons, that happens through the steps of gluon radiation and hadronization. Hard processes involving parton production allow the study of strong interactions in the asymptotic freedom regime, where perturbation theory can be applied. However, the association of observed jets to generator partons is not straightforward, since theoretical models cannot give a rigorous definition of a jet without introducing several approximations. On the other hand, algorithms for jet clustering give operative definitions of jets which don't have any information on elementary processes.

In the present analysis, a comparison between the multiplicity of partons produced by Monte Carlo and reconstructed jets is made. Quarks or gluons selected among final state particles of the hard processes are defined as

---

[3] Correlation between two variables x and y is defined as $\rho = \frac{\sigma_{xy}}{\sigma_x \sigma_y}$
where $\sigma_x(\sigma_y)$ is the variance of $x(y)$ and σ_{xy} is the covariance between x and y

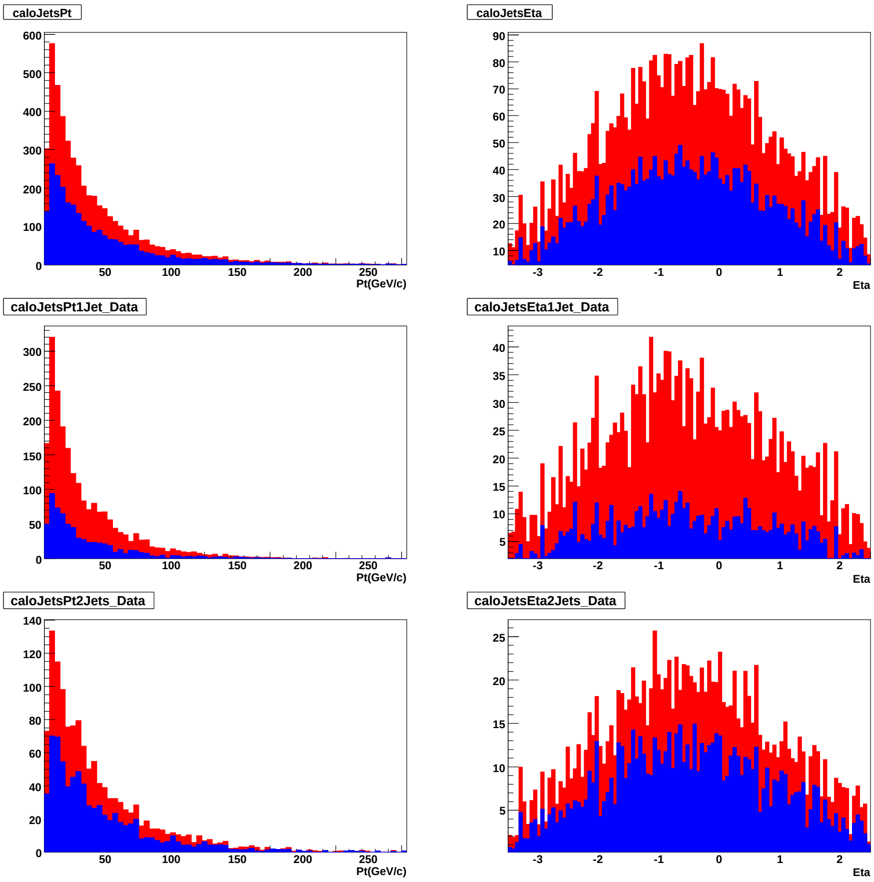

Figure 5.1: The Jets p_T (left) and η (right) distributions in the inclusive channel $Z(\mu^+\mu^-) + X$ (top) and in the 1(middle), 2(bottom) jets channels. Red: Signal + background. Blue: Monte Carlo background.

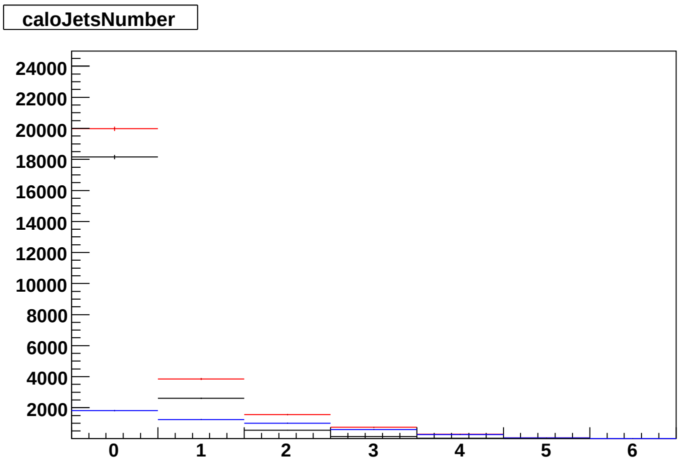

Figure 5.2: CaloJets multiplicity for jets with $p_T > 30$. Red: Signal + background. Black: Monte carlo signal. Blue: Monte Carlo background.

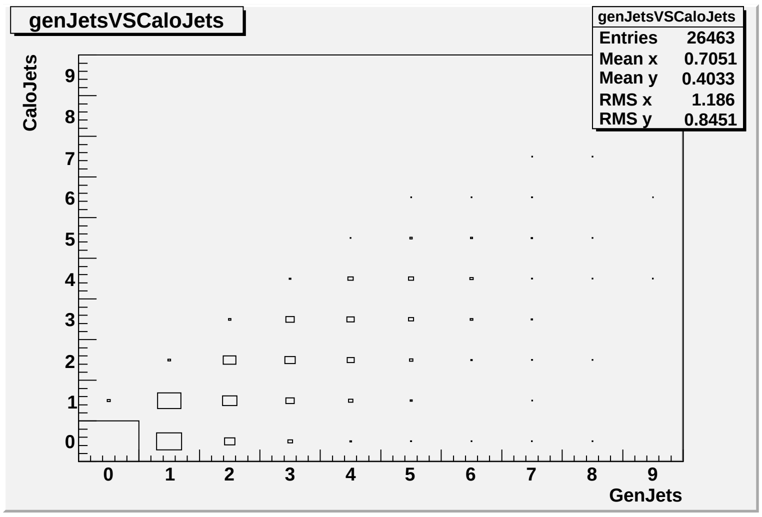

Figure 5.3: Multiplicity of GenJets versus multiplicity of CaloJets.

leading partons. The algorithm for the leading partons selection is reported in Appendix (B). Leading partons involved in pp hard scattering processes produce jets with high p_T values. A large p_T is required to select hard jets and reject Underlying Event jets. The same p_T and η cuts applied on reconstructed jets are also applied to leading partons. Figure (5.4) shows the distribution of number of partons n_P versus number of GenJets $n_{GenJets}$ and CaloJets $n_{CaloJets}$. The plots shows that the correlation between jets and partons is not 1. Three regions in the plots of (5.4) can be distinguished:

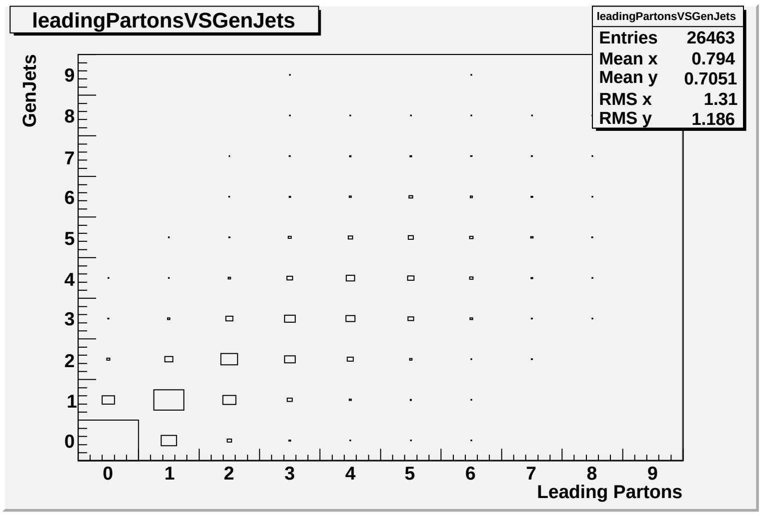

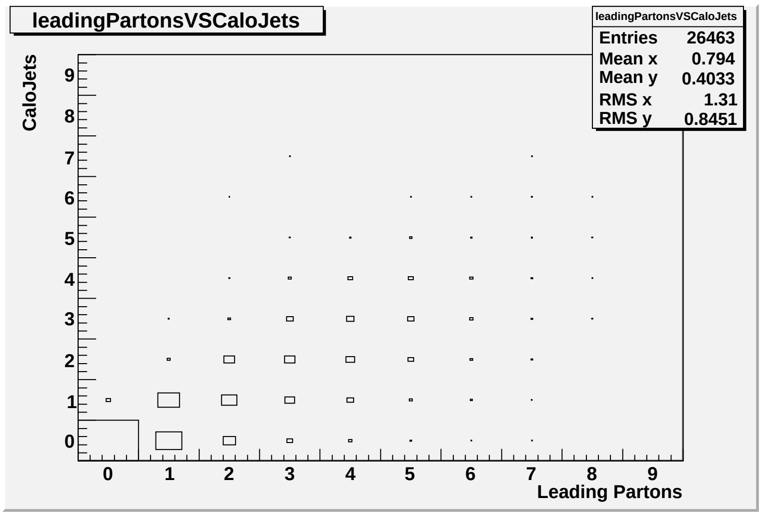

Figure 5.4: Multiplicity of leading Partons versus multiplicity of GenJets and CaloJets.

$n_P = n_{Jets}$, $n_P < n_{Jets}$, and $n_P > n_{Jets}$, where(n_{Jets} is the number of CaloJets or GenJets). To understand the population of the last two regions, an insight is necessary in the jets production and reconstruction mechanism. In the gluon radiation phase of jet formation a gluon carrying a great portion of the original parton can be produced. In this scenario, the high energy gluon may very well have a consistent lorentz boost in the direction orthogonal to the original parton momentum, resulting in the formation of two jets. This causes an excess of jet number with respect to partons, contributing to the population $n_P < n_{GenJets/CaloJets}$ region. However, the parton energy in this scenario is degenerated, since it is divided amongst the two separate jets. If the resulting jets are not energetic enough to survive kinematic cuts, they are mis-interpreted as Underlying Event jets and thus rejected. This contributes to events with $n_P > n_{GenJets/CaloJets}$. Also, energy loss due to inefficiencies in the calorimeters produces a similar effect.

5.3.2 Muons

Muons with a high measured p_T produced in hard processes provide a clean signature in the detector. The distributions of muons kinematic variables p_T,η and ϕ for data, MC signal and MC background are shown in Figure(5.5). No kinematic cuts were applied.

Due to the muon detector angular coverage, the muon spectra extend up to $|\eta| \sim 2.4$ A threshold is put on the highest p_T muon: only events with at least a muon with p_T greater than 15 GeV/c are considered. A cut on the overall muon distribution was made, so that all muons with $p_T < 5$ GeV/c are discarded.

5.3.3 Reconstructed Z candidates

Z candidates are reconstructed through a combinatorial algorithm that combines all possible μ^+ μ^- pairs. The total 4-momentum of the Z is then obtained as a sum of the particles 4-momenta. It is also possible to impose a cut on the reconstructed Z variables. Since all possible combinations are taken into account, fake Z can be reconstructed even in a true $Z \rightarrow \mu^+\mu^-$ event if an extra muon is present. This results in an effective contribution to the background for any Z measurement, which sums up to the physical backgrounds. The Monte Carlo generated $Z \rightarrow \mu^+\mu^-$ events actually present a Z/γ^* exchange in the matrix element. This produces a Drell-Yan contribution to the $\mu^+\mu^-$ mass term which has a $1/\hat{s}$ behavior, where $\hat{s}$ is the center of mass energy squared of the Drell-Yan process. Such contribution is present in

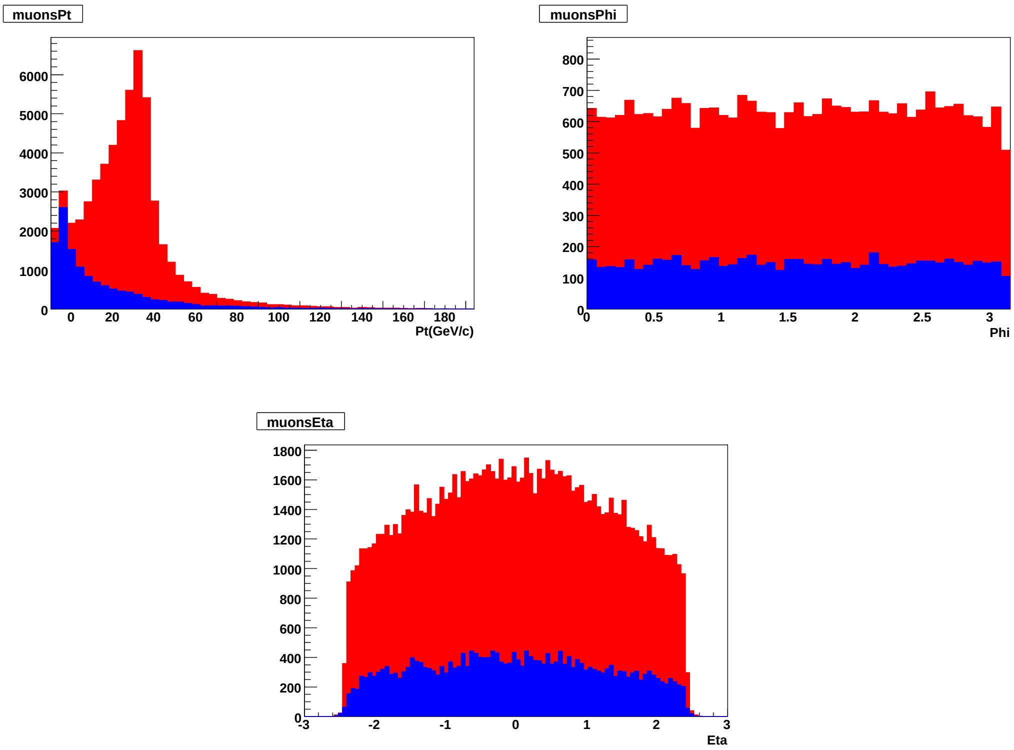

Figure 5.5: The muons p_T (top left), ϕ (top right) and η(bottom) spectra in the inclusive $(Z(\mu^+\mu^-)+X)$ channel before cuts are performed. Red: Signal + background. Blue: Monte Carlo background.

the distribution of Figure(5.6). There is a bump in the $\mu^+\mu^-$ mass distribution around $m_{\mu^+\mu^-} = 40$ GeV$/c^2$ is an artifact due to a cut at generator level on $m_{\mu^+\mu^-} > 40$ GeV$/c^2$. However, there are Z candidates with reconstructed masses in the $m_{\mu^+\mu^-} < 40$ GeV$/c^2$ range, due to either combinatorial effects or energy loss of muons due to radiation emission.Figure(5.6) also shows the reconstructed Z mass for channels with different number of jets. The contribution of the background on the signal becomes more important as the number of jets increases.

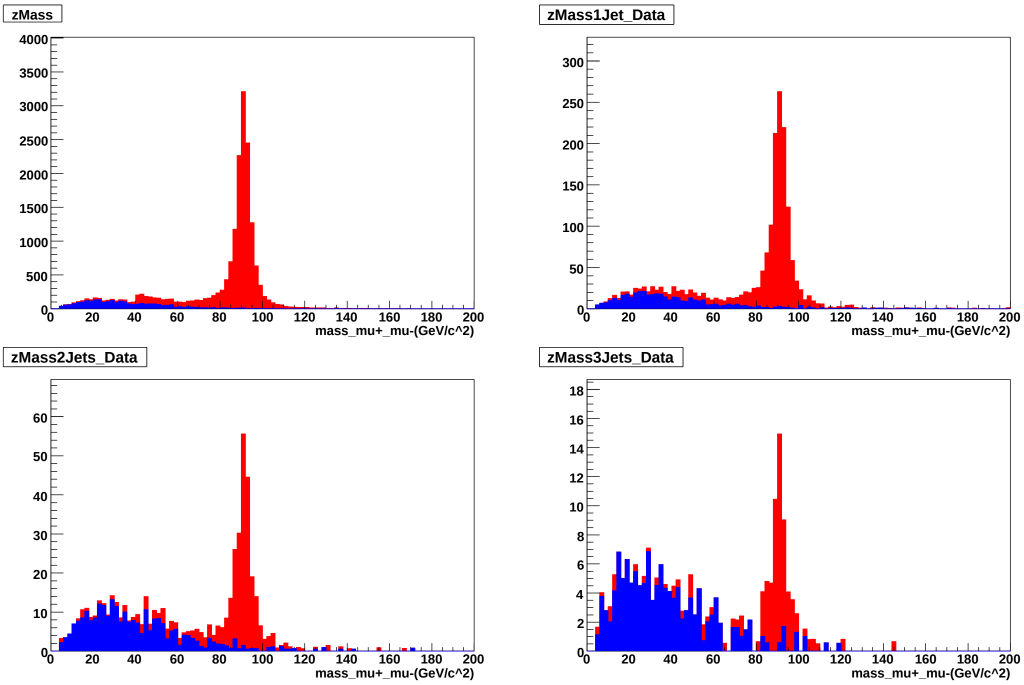

Figure 5.6: The $\mu^+\mu^-$ mass distribution in the inclusive channel $Z(\mu^+\mu^-)+X$ (top-left) and in the 1 (top-right), 2 (bottom-left), 3 (bottom-right) jets channels. GeV$/c^2$ is intended on the x axis. Red: Signal + background. Blue: Monte Carlo background.

5.4 Background subtraction

A data driven procedure to to reject the background has been developed. It consists two steps:

Background yield estimation: The total number of background events is estimated from a fit to the reconstructed $\mu^+\mu^-$ mass. The model for

Table 5.3: Summary on kinematic cuts

$p_{T,\mu} > 15$ GeV/c for highest p_T muons
$p_{T,\mu} > 5$ GeV/c
$40 < m(\mu^+\mu^-) < 200$

the fit is the sum of two different functions for the respective contributions of Z signal events and background events. The fit results allow to estimate the fractions of signal and background on the total number of events.

Subtraction of the background: The shape of the background distributions for variables other than the Z mass is obtained from Monte Carlo. Monte Carlo Background distributions are normalized to the background yield estimated from the $\mu^+\mu^-$ mass fit, and then they are subtracted from the distributions which contain signal+background.

The procedure is applied separately to events with different number of jets. After the subtraction procedure is performed and errors are calculated, the resulting distribution can be compared to the signal distribution from Monte Carlo truth in order to evaluate the reliability of the procedure.

5.4.1 Determination of Z event yields

The first step of the background subtraction consists of the determination of the signal/background fraction for $Z + n$ jets distributions. In this procedure, the events with different number of jets n were treated as independent channels. Only events in the $m_{\mu^+\mu^-} > 40$ GeV/c^2 range are considered in order to take into acconunt the cut at $m_{\mu^+\mu^-} > 40$ at generator level described in Section (5.3.3). The procedure of rejection was performed on channels with n = 1, 2, 3 jets. For each channel, a fit to the mass distribution of the reconstructed Z is made. The fit function is modeled as a sum of two functions

$$f_{fit}(m) = f_{background}(m) + f_{signal}(m), \tag{5.1}$$

where m is the invariant mass of $\mu^+\mu^-$. Once the parameters of the two functions have been obtained from the fit, the fraction of background events F_B is defined:

$$F_B = \frac{\int_a^b f_{background}(m)dx}{\int_a^b (f_{background}(m) + f_{signal}(m))\,dx} \tag{5.2}$$

where the integration interval $[a, b]$ can be adjusted to select a specific region of invariant mass.

Model functions for background and signal

The model for the signal function f_{signal} is the convolution[4] between a relativistic Breit-Wigner function and a Gaussian, multiplied by a decreasing exponential. The exponential is a phenomenological term to take into account the effect of Parton Distribution Functions .
The background function $f_{background}$ is a second order polynomial multiplied by a decreasing exponential in the case of 1 and 2 jets channels, and a first order polynomial multiplied by a decreasing exponential for the 3 jets channel, due to the lower statistics in the test sample for n jets $= 3$.
The signal function can therefore be written as:

$$f_{signal}(m) = N \cdot e^{(-\lambda_S m)} \int \frac{1}{\sqrt{2\pi\sigma^2}} e^{\left(\frac{(m'-m)^2}{2\sigma}\right)} \cdot BW(m')dm', \tag{5.3}$$

where $BW(m)$ is the normalized relativistic Breit-Wigner function:

$$BW(m) = \frac{2}{\pi} \frac{\Gamma_Z^2 m_Z^2}{(m^2 - m_Z^2) + m^4(\Gamma_Z^2/m_Z^2)}. \tag{5.4}$$

The background function is:

$$f_{background,n}(m) = e^{(-\lambda_{B,n} m)}(P_{0,n} + P_{1,n}m + P_{2,n}m^2), \tag{5.5}$$

for $n = 1, 2$ jets, and

$$f_{background,3}(m) = e^{(-\lambda_{B,3} m)}(P_{0,3} + P_{1,3}m). \tag{5.6}$$

for the $n = 3$ jets case. Another possibility for f_{signal} was to add to the term of Equation (5.3) a photon propagator term:

$$f_\gamma = N_\gamma e^{(-\lambda_\gamma m)} \frac{1}{m^2}, \tag{5.7}$$

in order to take into account the $\sim \frac{1}{s}$ behavior of the signal far from the m_Z peak. This possibility was explored but was not convenient, since the Drell-Yan contribution of the γ is not distinguishable from the background contribution in the fit.

---

[4] The convolution between two functions f and g is defined as the function $h(x) = \int f(x') \cdot g(x' - x)dx'$.

The $\mu^+\mu^-$ mass fit

The three fits to the Z mass histograms were performed with the least squares method. The variable X^2_i was built for each of the three channels. X^2 is defined as:

$$X^2 = \sum_{i=1}^{N} \frac{(N_i^{obs} - N_i^{exp})^2}{\Delta N_i^{obs}}, \tag{5.8}$$

where N is the number of bins, the N_i^{obs} is the content of the ith bin, N_i^{exp} is the value of the fit function evaluated in the center of the ith bin, ΔN_i^{obs} is the uncertainty on the ith bin content. The fit procedure consists in finding the values of the fit functions' parameters for which X^2 assumes the minimum possible value. The distribution probability of X^2 at its minimum possible value becomes the χ^2 distribution function[5][72]. The obtained fit functions are dependent from the choice of the bin. In order to obtain a bin-independent function that can be interpreted as a probability distribution, it should be $N_i^{exp} = f(x_i) \cdot \Delta B_i$, where x_i and ΔB_i are the center and the width of ith bin respectively. The fit range is $[40, 200]$ GeV/c^2 and it includes the regions where the background distribution is dominant over the signal ("sidebands"). This inclusion is needed to improve the performance of the fit, since in the sidebands the background function gives a robust contribution to data, while restraining the fit range under the Z mass peak region, the contribution of the background would be poorly extimated with fit procedures. The results of the fits are reported in Table (5.4).

Estimation of the background fraction

The background fraction F_B as defined in 5.2 can be evaluated from the functions obtained in the $\mu^+\mu^-$ mass fit. The integral of the fit functions are evaluated with methods implemented in the ROOT program[71]. The range of mass $77.5 < m_{\mu^+\mu^-} < 121.5$ is selected. In such range the background fraction is then obtained in this interval. At the same time a cut is imposed to discard events outside the selected mass interval.

5.4.2 Background subtraction method

The subtraction procedure requires the knowledge of the background distribution function of variables which must be performed on. For the present analysis, Monte Carlo background distributions are used. The distribution

---

[5] This is only true if X has a linear dependence from parameters and parameters have Gaussian distribution function. In the other cases this is true in the limit where $N \to \infty$

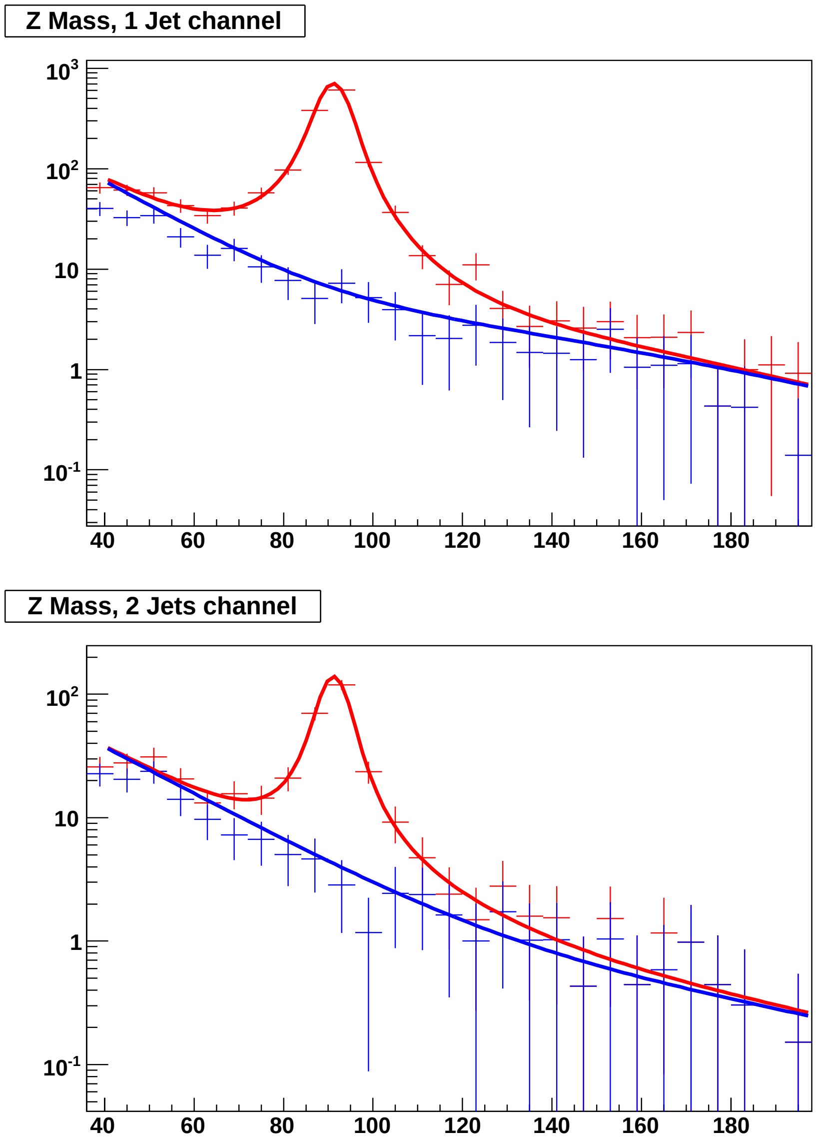

Figure 5.7: The fit to $\mu^+\mu^-$ mass in the 1 and 2 jets channel. Red: data histogram and data fit function ($f_{background}(m) + f_{signal}(m)$). Blue: Background histogram and background fit function ($f_{background}(m)$ only).

Table 5.4: Results for the three fits to Z mass

Parameter	Description	Value
$Z+1$ jet mass fit		
$\chi^2/ndof$	χ^2 per degrees of freedom	12/16
$ndof$	number of degrees of freedom	16
m_Z	mass of the Z	91.5 ± 0.3
Γ_Z	Z total width	5.8 ± 0.8
μ_Z	shift of the m_Z	fixed to 0 in the fit
σ_Z	resolution width for the Z mass	2.0 ± 0.6
Λ_S	exponential parameter for the signal function	-0.038 ± 0.009
Yield	integral of the Z signal function	$4 \cdot 10^4 \pm 3 \cdot 10^3$
P_0	background polynomial coefficient of order 0	1700 ± 1200
P_1	background polynomial coefficient of order 1	30 ± 30
P_2	background polynomial coefficient of order 2	0.02 ± 0.02
Λ_B	exponential parameter for the background function	-0.040 ± 0.009
$Z+2$ jets mass fit		
$\chi^2/ndof$	χ^2 per degrees of freedom	9/16
$ndof$	number of degrees of freedom	16
m_Z	mass of the Z	91.5 ± 0.7
Γ_Z	Z total width	6 ± 2
μ_Z	shift of the m_Z	fixed to 0 in the fit
σ_Z	resolution width for the Z mass	1.8 ± 1.6
Λ_S	exponential parameter for the signal function	-0.031 ± 0.002
Yield	integral of the Z signal function	$2 \cdot 10^4 \pm 4 \cdot 10^4$
P_0	background polynomial coefficient of order 0	340 ± 140
P_1	background polynomial coefficient of order 1	-4 ± 3
P_2	background polynomial coefficient of order 2	0.016 ± 0.015
Λ_B	exponential parameter for the background function	-0.025 ± 0.019
$Z+3$ jets mass fit		
$\chi^2/ndof$	χ^2 per degrees of freedom	6/15
$ndof$	number of degrees of freedom	15
m_Z	mass of the Z	91.3 ± 0.8
Γ_Z	Z total width	5 ± 4
μ_Z	shift of the m_Z	fixed to 0
σ_Z	resolution width for the Z mass	2.5 ± 1.9
Λ_S	exponential parameter for the signal function	-0.023 ± 0.015
Yield	integral of the Z signal	$5 \cdot 10^4 \pm 6 \cdot 10^3$
P_0	background polynomial coefficient of order 0	120 ± 50
P_1	background polynomial coefficient of order 1	-0.02 ± 0.2
Λ_S	exponential parameter for the background function	-0.04 ± 0.02

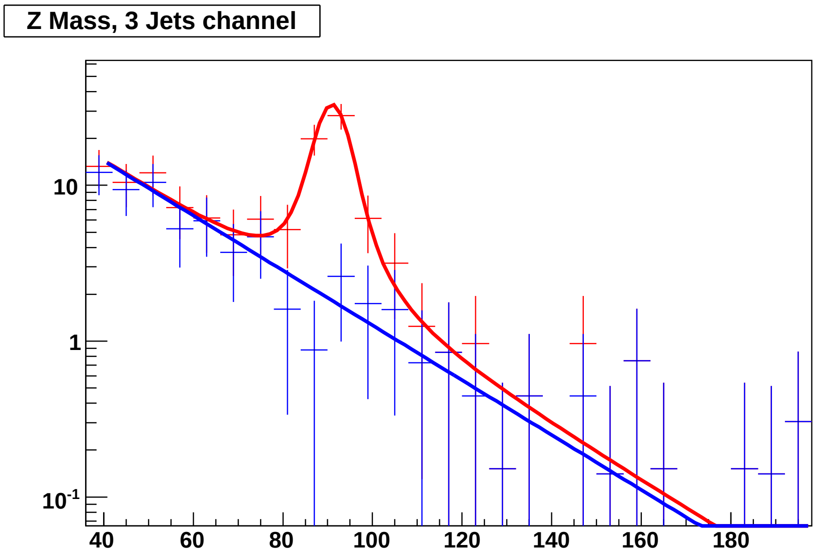

Figure 5.8: The fit to Z mass in the 3 jets channel. Red: data histogram and data fit function $(f_{background}(m) + f_{signal}(m))$. Blue: Background histogram and background fit function $(f_{background}(m)$ only).

of an observed variable x is the sum of signal and background contributions:

$$\frac{dN_D}{dx} = \frac{dN_S}{dx} + \frac{dN_B}{dx} = D(x) = S(x) + B(x), \tag{5.9}$$

Where N_S and N_B are the number of signal and background events respectively The normalized distribution function is $\frac{B(x)}{\int B(x)} = b(x)$. The fraction of background events obtained for the $\mu^+\mu^-$, is the same for the distributions of all variables:

$$\frac{\int B(x)}{\int D(x)} = \frac{N_B}{N_D} = F_B. \tag{5.10}$$

so that the background distribution normalized to the number of background events can be written as:

$$b = \frac{B}{\int B} = \frac{\int D(x)dx}{\int D(x)dx}\frac{B(x)dx}{\int B(x)} = \frac{\int D(x)dx}{F_B}B(x). \tag{5.11}$$

The signal and background distributions are:

$$B(x) = b(x)\frac{F_B}{\int D(x)dx} \quad , \text{ and} \qquad S(x) = D(x) - B(x) \tag{5.12}$$

This procedure derives all informations from data except for the normalized distribution function of the background, which is obtained from Monte Carlo.

5.4.3 Jet multiplicity and and transverse momentum spectra after the rejection

The background subtraction in the special case of jets multiplicity can be applied without the need of MC, since only the number of estimated signal events for the three channels is needed. The plot in Figure (5.9) reports the number of events in the three jets channels for observed data(in red), Monte Carlo GenJets(in black), and background subtracted data(in green), showing good agreement between the latter two. The values of bins in Figure (5.9) and their statistics uncertainties are reported in Table (5.5). The same color convention is used for Figure(5.10), where the p_T of jets is shown. (5.4.3).

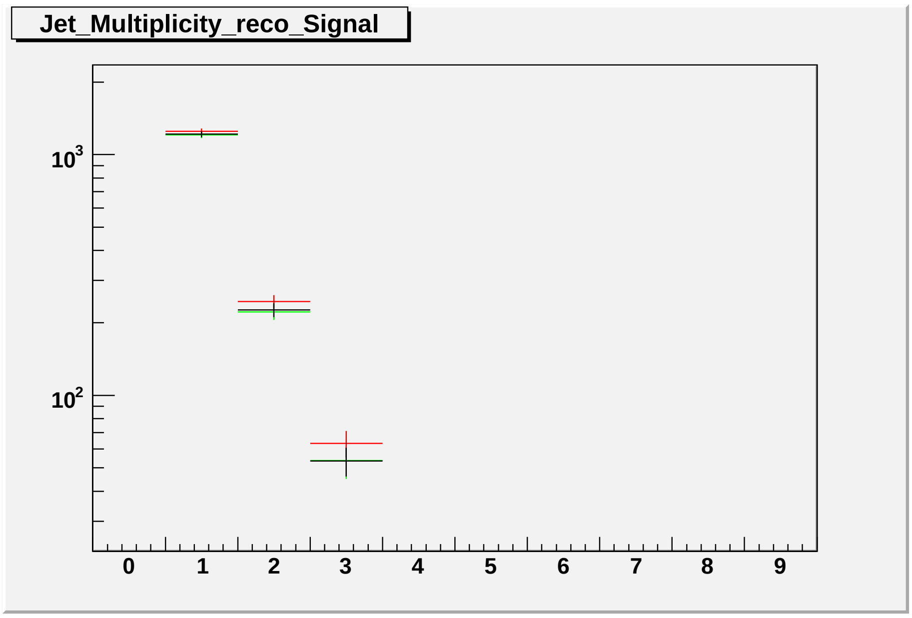

Figure 5.9: The jet multiplicity after background subtraction procedure (logarithm scale): the signal before the procedure is applied is red, Monte Carlo signal is black and signal after subtraction is green.

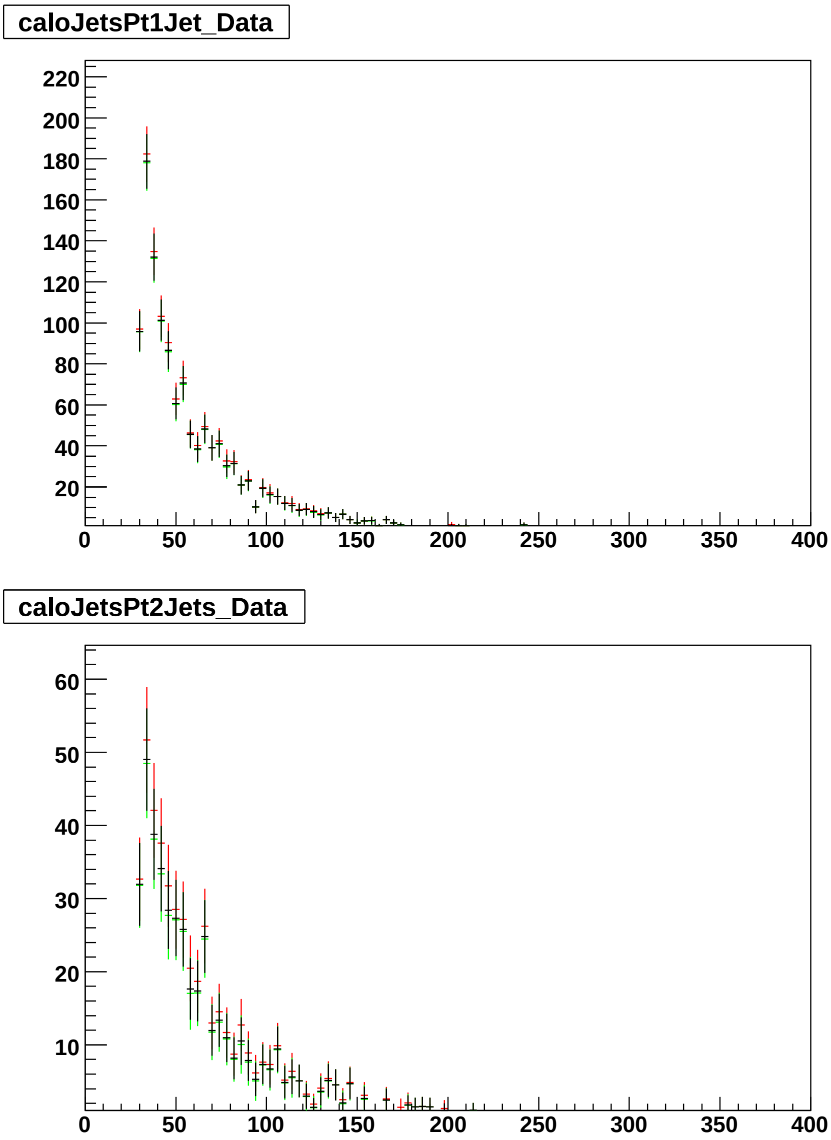

Figure 5.10: Jet p_T spectra after background subtraction procedure in logarithmic scale for 1 and 2 jets channels: the data before the procedure is applied is red, Monte Carlo signal is black and data after subtraction is green.

Table 5.5: Number of events after the subtraction in the different jets channels compared with the number of events from Monte Carlo truth.

Number of jets	Number of events	Number of MC truth signal events
1	1410 ± 40	1413
2	258 ± 20	262
3	62 ± 11	52

5.5 Evaluation of the $Z+$ jets cross section

The formula to estimate the cross section of an observed process is:

$$\sigma = \frac{N_{events}}{\mathcal{L} \times \epsilon_{cuts}}, \tag{5.13}$$

where N_{events} is the observed number of events, $\mathcal{L}$ is the luminosity of the machine and ϵ_{cuts} is the efficiency of the cuts imposed on the data. While luminosity in the present case is given by the MC parameters, in data taking the nominal value of $\mathcal{L}$ will be affected by an uncertainty of $\sim 10\%$ and will provide the main contribution to the systematics at LHC. ϵ_{cuts} is the

$$\epsilon_{cuts} = \frac{\text{number of signal events after the cuts}}{\text{number of signal events before the cuts}},$$

and it must be taken from MC truth. Table (5.5) shows the efficiency values for the cuts on the muons p_T and the Z invariant mass. The choice of the cuts introduces systematics uncertainties on the ϵ_{cuts} value due to resolution effects on the measurements of variables used for the cuts. The effect of this systematics has yet to be considered. The values of N_{events} and the statistics uncertainties on their values are evaluated with the subtraction method of Section 5.4.

Table 5.6: Efficiencies for the cuts in the 1,2,3 jets channels

Cut	ϵ (1 jet)	ϵ (2 jets)	ϵ (3 jets)
p_T (highest p_T muon) > 15	0.99	0.98	0.99
$78 < m_Z < 121$	0.85	0.85	0.90

The displayed procedure to evaluate the cross section of $Z+$ jets channels can be immediately applied on data when an estimation of kinematic uncertainties is obtained. The cross section for the considered processes is shown in Table (5.7)

Table 5.7: Cross section values for the jets processes

Number of jets	cross section (pb)
1	167 ± 7
2	47 ± 3
3	7 ± 1

5.5.1 Estimation of Z + partons cross section

A first estimation of the $Z + n$ partons processes cross section can be given using Equation (5.13), where the number of events in the $Z + n$ partons channel is different from the number events in the $Z + n$ jets channel, as shown in Section 5.3.1. A plot that displays the number of partons and the number of CaloJets for each signal event is taken from MC and is shown in Figure(5.11). This plot is used to estimate the number of events in the $Z+n$ (with n = 1, 2, 3) partons channels with the following procedure:

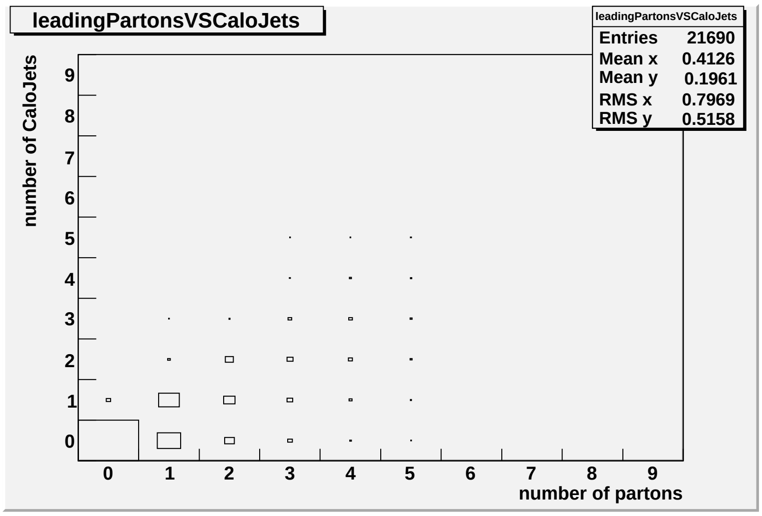

Figure 5.11: Multiplicity of leading Partons versus multiplicity of CaloJets for signal events.

1. The number of events in the m jets channels is obtained applying both the kinematic cuts and the subtraction procedure in the case of m = 1, 2, 3 jets channels. The number of events for the $m \neq 1, 2, 3$ jets channels is obtained after the imposition of kinematic cuts only.

2. The fraction of events in m jets channel that contributed to the n partons channel was obtained as

$$f_{mn} = \frac{c_{mn}}{\sum_k c_{mk}} \tag{5.14}$$

   where c_{mn} is the number of events with m jets and n partons taken from the jet-parton multiplicity plot in Figure(5.11).

3. The fraction obtained in Equation 5.15 is multiplied by the number of jets in the m channel obtain the contribution to the cross section of the n partons channel:

$$n_{mn} = n_m \cdot f_{mn} \tag{5.15}$$

4. The cross section of the n partons process is obtained as the sum of contributions from all the jets channels divided by the luminosity and by the cuts efficiencies:

$$\sigma_{n\,\text{partons}} = \sum_m \frac{n_{mn}}{\mathcal{L} \cdot \epsilon_{m\,\text{jets}}} \cdot \frac{1}{\epsilon_{n\,\text{partons}}} \tag{5.16}$$

   where $\epsilon_{m\,\text{jets}}$ are the cut efficiencies for the jets channels and $\epsilon_{n\,\text{partons}}$ are the cuts efficiencies for partons shown in table 5.8.

The results for the cross section of the 1, 2, 3 partons channels and the corresponding Monte Carlo generation values are reported in Table(5.9). The 1 parton channel shows a good agreement with the Monte Carlo value and the two partons channel is consistent within 3 σ with the Monte Carlo. The 3 parton channel is not consistent even within 3 sigma. However, systematic uncertainties due to the choice of the cuts were not taken into account.

Table 5.8: Efficencies for the $p_T > 30$ GeV/c cut on the partons

ϵ (1 parton)	ϵ (2 partons)	ϵ (3 partons)
0.8	0.77	0.63

Table 5.9: Cross section values for the partons processes

Number of partons	Measured cross section (pb)	Generation cross section (pb)
1	324 ± 11	321
2	93 ± 3	99.67
3	34.3 ± 1.5	27

Conclusions

The work consisted in the study of the $pp \to Z+n$ jets $\to \mu^+\mu^-$ jets channel with the CMS detector at LHC. When the machine will start the data taking, scheduled before the end of this year, the measurement of the Z channels cross section will be one of the earliest to be taken at LHC. The reason for the choice of this channel is that it presents a clean signature of a pair of $\mu^+\mu^-$ with high transverse momentum and with invariant mass distribution peaked around the m_Z. Because of their high p_T values, muons from Z decay also present high trigger efficiency. Also, precision measurements on the $Z+n$ jets channels are possible thanks to the high signal/background ratio that can be obtained. The present work develops a strategy for the selection of a $Z+$ jets signal with good purity that mainly relies on information taken from data. This procedure was applied on the analyzed sample, developing a procedure to estimate the cross section of the $Z+n$ =1, 2, 3 jets channels. In chapter 5 the procedure is displayed entirely: in section 5.2 basic requirements for a signal event are made, imposing cuts on the kinematic variables of muons and jets. In section 5.3 the background subtraction method is explained and then performed on the data sample. Its results are shown in section 5.4, while section 5.5 shows that the procedure allows to evaluate the cross section of the considered $Z+$ jets processes. A parton-jet association strategy was considered in order to associate the partons involved in the hard process with the observed jets.
The analysis strategy presents several possible improvements:

- The sample can be extended to include QCD background processes and $b\bar{b}$ production processes.
- The sistematics uncertainties due to resolution and inefficiencies have yet to be evaluated.
- The entire analysis procedure can be applied with no particular difficulty on $Z \to e^+e^- + n$ jets processes.

The present thesis work provides a procedure for the measurement of $Z+$ jets cross section. Such procedure can be performed on the early data taken at CMS after the LHC startup.

Appendix A

Event selection

The analysis was performed within the CMSSW framework. The dataset on which the study was performed has been imported on the storage devices of INFN Napoli. The dateset has gone through a process of "Skimming" to reduce the dimension of the set on storage devices by discarding informations not relevant for the analysis. The script is realized in the CMSSW framework (the so-called "configuration file"). In CMSSW specific duties are devolved to sub-scripts (modules), which are then called out in the configuration file. Configuration file for the Skimming is reported:

```
 process SKIM = {
  include "FWCore/MessageLogger/data/MessageLogger.cfi"
  include "Configuration/EventContent/data/EventContent.cff"
  include "PhysicsTools/HepMCCandAlgos/data/genParticleCandidates2GenParticles.c
  include "SimGeneral/HepPDTESSource/data/pythiapdt.cfi"

  untracked PSet maxEvents = { untracked int32 input = -1 }

 source = PoolSource {
   untracked vstring fileNames = {
'/store/CSA07/2007/11/29/
CSA07-CSA07AllEvents-Tier0-A3-Chowder/0000/002198E8-CC9E-DC11-BDD6-00304855D4B8.

   }
 }

 module SKIM = PoolOutputModule {
  untracked string fileName =
```

```
  "rfio:/castor/cern.ch/user/o/oiorio/ZMuMuJetsSkimRecod.root"
  untracked vstring outputCommands = {
              "drop *",
              "keep *_zToMuMu_*_*",
              "keep *_muons_*_*",
              "keep *_trackerMuons_*_*",
              "keep *_genParticles_*_*",
              "keep *_leadingPartons_*_*",
              "keep *_iterativeCone5GenJetsNoNuBSM_*_*",
              "keep *_iterativeCone5CaloJets_*_*",
              "keep *_csaweightproducer_*_*",
          "keep *_genMetNoNuBSM_*_*",
              "keep recoCaloMETs_met_*_Rec1",
      "keep *_ctfWithMaterialTracks_*_*",
      "keep *_standAloneMuons__*",
      "keep *_zToMuMuMC_*_*",
        "keep *_selectedPartons_*_*",
        "keep *_selectedMuons_*_*",
              "keep *_selectedGenJets_*_*",
         "keep *_selectedCaloJets_*_*",
              "keep *_isolatedGenJets_*_*",
              "keep *_isolatedCaloJets_*_*"
   }
 untracked PSet SelectEvents = {
    vstring SelectEvents = {
     "muonsCount"
    }
  }


  }

   module zToMuMu = CandViewShallowCloneCombiner {
   string decay = "muons@+ muons@-"
   string cut = "mass > 5"
   bool filter = true
 }

module zToMuMuMC = CandViewRefSelector {
   InputTag src = genParticles
   string cut = "pdgId=23 & status=3 &
```

```
    numberOfDaughters>0 & abs(daughter(0).pdgId)=13"
    bool filter = true
  }

module selectedMuons = CandViewRefSelector {
    InputTag src = muons
    string cut = "pt > 15 & abs(eta)<3"
    bool filter = true
  }

  module selectedCaloJets = CandViewRefSelector {
    InputTag src = iterativeCone5CaloJets
    string cut = "pt > 30 & abs(eta)<3"
    bool filter = true
  }

  module selectedGenJets = CandViewRefSelector {
    InputTag src = iterativeCone5GenJetsNoNuBSM
    string cut = "pt > 30 & abs(eta)<3"
    bool filter = true
  }

module selectedPartons = CandViewRefSelector {
    InputTag src = leadingPartons
    string cut = "pt > 30 & abs(eta)<3"
    bool filter = true
  }

  module leadingPartons =  ZMuMuJetsLeadingPartonProducer {
    InputTag src = genParticles
  }

  module isolatedCaloJets = ZMuMuJetsIsolatedJetsProducer {
  InputTag muons = selectedMuons
  InputTag jets = selectedCaloJets
  double deltar = 0.3

}

  module isolatedGenJets = ZMuMuJetsIsolatedJetsProducer {
  InputTag muons = selectedMuons
```

```
 InputTag jets = selectedGenJets
 double deltar = 0.3

}

module generatorJetsMatch = ZMuMuJetsMatchedJetsProducer {
   InputTag partons = selectedPartons
   InputTag jets = isolatedGenJets
   string name = "selectedGenJets"
 }

 module calorimeterJetsMatch = ZMuMuJetsMatchedJetsProducer {
   InputTag partons = selectedPartons
   InputTag jets = isolatedCaloJets
   string name = "selectedCaloJets"
 }


 module csaweightproducer = CSA07EventWeightProducer {
    InputTag src = source

    # verbosity
    untracked bool talkToMe = false  #true

    # overall luminosity normalization  (in pb-1)
    double overallLumi = 10.
 }

  module printEventNumber = AsciiOutputModule { }

  module muonsFilter = CandViewCountFilter {
  InputTag src = muons
    uint32 minNumber = 2
  }

  path muonsCount = { muonsFilter  }

  path selection = {
  genParticles,
  zToMuMu,
  zToMuMuMC,
```

```
  leadingPartons,
  selectedPartons,
  selectedMuons,
  selectedGenJets,
  selectedCaloJets,
  isolatedCaloJets,
  isolatedGenJets,
  csaweightproducer
  }



  endpath out = { SKIM, printEventNumber }
}
```

Configuration file written to perform the kinematic cuts and to plot the distributions is reported here:

```
process ZMuMuJetsAnalysis = {

include "FWCore/MessageLogger/data/MessageLogger.cfi"
include "SimGeneral/HepPDTESSource/data/pythiapdt.cfi"



 source = PoolSource {
untracked vstring fileNames = {

'rfio:/castor/cern.ch/user/o/oiorio/skimZMuMuJets8NoMCuts.root'
    }
 }

replace PoolSource.fileNames = {

  'rfio:/castor/cern.ch/user/o/oiorio/skimZMuMuJets1NoMCuts.root',

}
```

```
untracked PSet options = {

  untracked bool wantSummary = true
}

service = TFileService {
    string fileName = "ZMuMuJetsHistograms_75_120.root"
}

 untracked PSet maxEvents = {
    untracked int32 input = -1
}


module muonCount = CandViewCountFilter {
  InputTag src = muons
  uint32 minNumber = 2
}

 module zToMuMu = CandViewShallowCloneCombiner {
   string decay = "selectedMuons@+ selectedMuons@-"
   string cut = "77.5 < mass < 121"
   bool filter = true
}

module selectedMuons = CandViewRefSelector {
   InputTag src = muons
   string cut = "pt > 5 & abs(eta) < 5"
   bool filter = true
 }

module selectedMuonsCut = CandViewRefSelector {
   InputTag src = muons
   string cut = "pt > 15 & abs(eta) < 5"
   bool filter = true
}


 module selectedCaloJets = CandViewRefSelector {
   InputTag src = iterativeCone5CaloJets
```

```
   string cut = "pt > 30 & abs(eta)<3"
   bool filter = true
 }

 module selectedGenJets = CandViewRefSelector {
   InputTag src = iterativeCone5GenJetsNoNuBSM
   string cut = "pt > 30 & abs(eta)<3"
   bool filter = true
 }

module selectedPartons = CandViewRefSelector {
   InputTag src = leadingPartons
   string cut = "pt > 30 & abs(eta)<3"
   bool filter = true
 }

 module zToMuMuMC = CandViewRefSelector {
   InputTag src = genParticles
   string cut = "pdgId=23 & status=3 &
   numberOfDaughters>0 & abs(daughter(0).pdgId)=13"
   bool filter = true
 }

  module leadingPartons =  ZMuMuJetsLeadingPartonProducer {
   InputTag src = genParticles
 }

 module generatorJetsMatch = ZMuMuJetsMatchedJetsProducer {
   InputTag partons = selectedPartons
   InputTag jets = isolatedGenJets
   string name = "selectedGenJets"
 }

 module calorimeterJetsMatch = ZMuMuJetsMatchedJetsProducer {
   InputTag partons = selectedPartons
   InputTag jets = isolatedCaloJets
   string name = "selectedCaloJets"
 }

 module isolatedCaloJets = ZMuMuJetsIsolatedJetsProducer {
 InputTag muons = selectedMuons
```

```
 InputTag jets = selectedCaloJets
 string name = "isolatedCaloJets"
  double deltar = 0.3

}

 module isolatedGenJets = ZMuMuJetsIsolatedJetsProducer {
 InputTag muons = selectedMuons
 InputTag jets = selectedGenJets
 string name = "isolatedGenJets"
 double deltar = 0.3

}

module moreThan0Jets = CandViewCountFilter {
  InputTag src = isolatedCaloJets
  uint32 minNumber = 1
}

module moreThan1Jets = CandViewCountFilter {
  InputTag src = isolatedCaloJets
  uint32 minNumber = 2
}

module moreThan2Jets = CandViewCountFilter {
  InputTag src = isolatedCaloJets
  uint32 minNumber = 3
}

module moreThan3Jets = CandViewCountFilter {
  InputTag src = isolatedCaloJets
  uint32 minNumber = 4
}

module moreThan4Jets = CandViewCountFilter {
  InputTag src = isolatedCaloJets
  uint32 minNumber = 5
}

module moreThan5Jets = CandViewCountFilter {
  InputTag src = isolatedCaloJets
```

```
  uint32 minNumber = 6
}

 module csaweightproducer = CSA07EventWeightProducer {
    InputTag src = source

    # verbosity
    untracked bool talkToMe = false  #true

    # overall luminosity normalization  (in pb-1)
    double overallLumi = 10.
 }

module allHistos = zMuMuJetsHistogrammer {
  bool hasglobalweight = true
  InputTag weight = csaweightproducer:weight
  InputTag partons = selectedPartons
  InputTag caloJets = isolatedCaloJets
  InputTag genJets = isolatedGenJets
  InputTag matchedCaloJets = calorimeterJetsMatch
  InputTag matchedGenJets = generatorJetsMatch
  InputTag muons = selectedMuons
  InputTag z = zToMuMu
  InputTag zMC = zToMuMuMC
}

module signalHistos =  zMuMuJetsHistogrammer {
  bool hasglobalweight = true
  InputTag weight = csaweightproducer:weight
  InputTag partons = selectedPartons
  InputTag caloJets = isolatedCaloJets
  InputTag genJets = isolatedGenJets
  InputTag matchedCaloJets = calorimeterJetsMatch
  InputTag matchedGenJets = generatorJetsMatch
  InputTag muons = selectedMuons
  InputTag z = zToMuMu
  InputTag zMC = zToMuMuMC
}

module backgroundHistos =  zMuMuJetsHistogrammer {
  bool hasglobalweight = true
```

```
  InputTag weight = csaweightproducer:weight
  InputTag partons = selectedPartons
  InputTag caloJets = isolatedCaloJets
  InputTag genJets = isolatedGenJets
  InputTag matchedCaloJets = calorimeterJetsMatch
  InputTag matchedGenJets = generatorJetsMatch
  InputTag muons = selectedMuons
  InputTag z = zToMuMu
  InputTag zMC = zToMuMuMC
}

module allHistos0Jet = zMuMuJetsHistogrammer {
  bool hasglobalweight = true
  InputTag weight = csaweightproducer:weight
  InputTag partons = selectedPartons
  InputTag caloJets = isolatedCaloJets
  InputTag genJets = isolatedGenJets
  InputTag matchedCaloJets = calorimeterJetsMatch
  InputTag matchedGenJets = generatorJetsMatch
  InputTag muons = selectedMuons
  InputTag z = zToMuMu
  InputTag zMC = zToMuMuMC
}

module signalHistos0Jet = zMuMuJetsHistogrammer {
  bool hasglobalweight = true
  InputTag weight = csaweightproducer:weight
  InputTag partons = selectedPartons
  InputTag caloJets = isolatedCaloJets
  InputTag genJets = isolatedGenJets
  InputTag matchedCaloJets = calorimeterJetsMatch
  InputTag matchedGenJets = generatorJetsMatch
  InputTag muons = selectedMuons
  InputTag z = zToMuMu
  InputTag zMC = zToMuMuMC
}

module backgroundHistos0Jet = zMuMuJetsHistogrammer {
  bool hasglobalweight = true
  InputTag weight = csaweightproducer:weight
  InputTag partons = selectedPartons
```

```
  InputTag caloJets = isolatedCaloJets
  InputTag genJets = isolatedGenJets
  InputTag matchedCaloJets = calorimeterJetsMatch
  InputTag matchedGenJets = generatorJetsMatch
  InputTag muons = selectedMuons
  InputTag z = zToMuMu
  InputTag zMC = zToMuMuMC
}


module allHistos1Jet = zMuMuJetsHistogrammer {
  bool hasglobalweight = true
  InputTag weight = csaweightproducer:weight
  InputTag partons = selectedPartons
  InputTag caloJets = isolatedCaloJets
  InputTag genJets = isolatedGenJets
  InputTag matchedCaloJets = calorimeterJetsMatch
  InputTag matchedGenJets = generatorJetsMatch
  InputTag muons = selectedMuons
  InputTag z = zToMuMu
  InputTag zMC = zToMuMuMC
}

module signalHistos1Jet = zMuMuJetsHistogrammer {
  bool hasglobalweight = true
  InputTag weight = csaweightproducer:weight
  InputTag partons = selectedPartons
  InputTag caloJets = isolatedCaloJets
  InputTag genJets = isolatedGenJets
  InputTag matchedCaloJets = calorimeterJetsMatch
  InputTag matchedGenJets = generatorJetsMatch
  InputTag muons = selectedMuons
  InputTag z = zToMuMu
  InputTag zMC = zToMuMuMC
}

module backgroundHistos1Jet = zMuMuJetsHistogrammer {
  bool hasglobalweight = true
  InputTag weight = csaweightproducer:weight
  InputTag partons = selectedPartons
  InputTag caloJets = isolatedCaloJets
```

```
  InputTag genJets = isolatedGenJets
  InputTag matchedCaloJets = calorimeterJetsMatch
  InputTag matchedGenJets = generatorJetsMatch
  InputTag muons = selectedMuons
  InputTag z = zToMuMu
  InputTag zMC = zToMuMuMC
}

module allHistos2Jets = zMuMuJetsHistogrammer {
  bool hasglobalweight = true
  InputTag weight = csaweightproducer:weight
  InputTag partons = selectedPartons
  InputTag caloJets = isolatedCaloJets
  InputTag genJets = isolatedGenJets
  InputTag matchedCaloJets = calorimeterJetsMatch
  InputTag matchedGenJets = generatorJetsMatch
  InputTag muons = selectedMuons
  InputTag z = zToMuMu
  InputTag zMC = zToMuMuMC
}

module signalHistos2Jets = zMuMuJetsHistogrammer {
  bool hasglobalweight = true
  InputTag weight = csaweightproducer:weight
  InputTag partons = selectedPartons
  InputTag caloJets = isolatedCaloJets
  InputTag genJets = isolatedGenJets
  InputTag matchedCaloJets = calorimeterJetsMatch
  InputTag matchedGenJets = generatorJetsMatch
  InputTag muons = selectedMuons
  InputTag z = zToMuMu
  InputTag zMC = zToMuMuMC
}

module backgroundHistos2Jets = zMuMuJetsHistogrammer {
  bool hasglobalweight = true
  InputTag weight = csaweightproducer:weight
  InputTag partons = selectedPartons
  InputTag caloJets = isolatedCaloJets
  InputTag genJets = isolatedGenJets
  InputTag matchedCaloJets = calorimeterJetsMatch
```

```
  InputTag matchedGenJets = generatorJetsMatch
  InputTag muons = selectedMuons
  InputTag z = zToMuMu
  InputTag zMC = zToMuMuMC
}

module allHistos3Jets = zMuMuJetsHistogrammer {
  bool hasglobalweight = true
  InputTag weight = csaweightproducer:weight
  InputTag partons = selectedPartons
  InputTag caloJets = isolatedCaloJets
  InputTag genJets = isolatedGenJets
  InputTag matchedCaloJets = calorimeterJetsMatch
  InputTag matchedGenJets = generatorJetsMatch
  InputTag muons = selectedMuons
  InputTag z = zToMuMu
  InputTag zMC = zToMuMuMC
}

module signalHistos3Jets = zMuMuJetsHistogrammer {
  bool hasglobalweight = true
  InputTag weight = csaweightproducer:weight
  InputTag partons = selectedPartons
  InputTag caloJets = isolatedCaloJets
  InputTag genJets = isolatedGenJets
  InputTag matchedCaloJets = calorimeterJetsMatch
  InputTag matchedGenJets = generatorJetsMatch
  InputTag muons = selectedMuons
  InputTag z = zToMuMu
  InputTag zMC = zToMuMuMC
}

module backgroundHistos3Jets = zMuMuJetsHistogrammer {
  bool hasglobalweight = true
  InputTag weight = csaweightproducer:weight
  InputTag partons = selectedPartons
  InputTag caloJets = isolatedCaloJets
  InputTag genJets = isolatedGenJets
  InputTag matchedCaloJets = calorimeterJetsMatch
  InputTag matchedGenJets = generatorJetsMatch
  InputTag muons = selectedMuons
```

```
  InputTag z = zToMuMu
  InputTag zMC = zToMuMuMC
}

module allHistos4Jets = zMuMuJetsHistogrammer {
  bool hasglobalweight = true
  InputTag weight = csaweightproducer:weight
  InputTag partons = selectedPartons
  InputTag caloJets = isolatedCaloJets
  InputTag genJets = isolatedGenJets
  InputTag matchedCaloJets = calorimeterJetsMatch
  InputTag matchedGenJets = generatorJetsMatch
  InputTag muons = selectedMuons
  InputTag z = zToMuMu
  InputTag zMC = zToMuMuMC
}

module signalHistos4Jets = zMuMuJetsHistogrammer {
  bool hasglobalweight = true
  InputTag weight = csaweightproducer:weight
  InputTag partons = selectedPartons
  InputTag caloJets = isolatedCaloJets
  InputTag genJets = isolatedGenJets
  InputTag matchedCaloJets = calorimeterJetsMatch
  InputTag matchedGenJets = generatorJetsMatch
  InputTag muons = selectedMuons
  InputTag z = zToMuMu
  InputTag zMC = zToMuMuMC
}

module backgroundHistos4Jets = zMuMuJetsHistogrammer {
  bool hasglobalweight = true
  InputTag weight = csaweightproducer:weight
  InputTag partons = selectedPartons
  InputTag caloJets = isolatedCaloJets
  InputTag genJets = isolatedGenJets
  InputTag matchedCaloJets = calorimeterJetsMatch
  InputTag matchedGenJets = generatorJetsMatch
  InputTag muons = selectedMuons
  InputTag z = zToMuMu
  InputTag zMC = zToMuMuMC
```

```
}

module allHistos5Jets = zMuMuJetsHistogrammer {
  bool hasglobalweight = true
  InputTag weight = csaweightproducer:weight
  InputTag partons = selectedPartons
  InputTag caloJets = isolatedCaloJets
  InputTag genJets = isolatedGenJets
  InputTag matchedCaloJets = calorimeterJetsMatch
  InputTag matchedGenJets = generatorJetsMatch
  InputTag muons = selectedMuons
  InputTag z = zToMuMu
  InputTag zMC = zToMuMuMC
}

module signalHistos5Jets = zMuMuJetsHistogrammer {
  bool hasglobalweight = true
  InputTag weight = csaweightproducer:weight
  InputTag partons = selectedPartons
  InputTag caloJets = isolatedCaloJets
  InputTag genJets = isolatedGenJets
  InputTag matchedCaloJets = calorimeterJetsMatch
  InputTag matchedGenJets = generatorJetsMatch
  InputTag muons = selectedMuons
  InputTag z = zToMuMu
  InputTag zMC = zToMuMuMC
}

module backgroundHistos5Jets = zMuMuJetsHistogrammer {
  bool hasglobalweight = true
  InputTag weight = csaweightproducer:weight
  InputTag partons = selectedPartons
  InputTag caloJets = isolatedCaloJets
  InputTag genJets = isolatedGenJets
  InputTag matchedCaloJets = calorimeterJetsMatch
  InputTag matchedGenJets = generatorJetsMatch
  InputTag muons = selectedMuons
  InputTag z = zToMuMu
  InputTag zMC = zToMuMuMC
}
```

```
module allHistosMoreThan5Jets = zMuMuJetsHistogrammer {
  bool hasglobalweight = true
  InputTag weight = csaweightproducer:weight
  InputTag partons = selectedPartons
  InputTag caloJets = isolatedCaloJets
  InputTag genJets = isolatedGenJets
  InputTag matchedCaloJets = calorimeterJetsMatch
  InputTag matchedGenJets = generatorJetsMatch
  InputTag muons = selectedMuons
  InputTag z = zToMuMu
  InputTag zMC = zToMuMuMC
}

module signalHistosMoreThan5Jets = zMuMuJetsHistogrammer {
  bool hasglobalweight = true
  InputTag weight = csaweightproducer:weight
  InputTag partons = selectedPartons
  InputTag caloJets = isolatedCaloJets
  InputTag matchedCaloJets = calorimeterJetsMatch
  InputTag matchedGenJets = generatorJetsMatch
  InputTag genJets = isolatedGenJets
  InputTag muons = selectedMuons
  InputTag z = zToMuMu
  InputTag zMC = zToMuMuMC
}

module backgroundHistosMoreThan5Jets = zMuMuJetsHistogrammer {
  bool hasglobalweight = true
  InputTag weight = csaweightproducer:weight
  InputTag partons = selectedPartons
  InputTag caloJets = isolatedCaloJets
  InputTag matchedCaloJets = calorimeterJetsMatch
  InputTag matchedGenJets = generatorJetsMatch
  InputTag genJets = isolatedGenJets
  InputTag muons = selectedMuons
  InputTag z = zToMuMu
  InputTag zMC = zToMuMuMC
}

sequence preselection = {
  muonCount,
```

```
  -selectedMuons,
  selectedMuonsCut,
  -leadingPartons,
  -selectedPartons,
  -selectedCaloJets,
  -selectedGenJets,
  -isolatedCaloJets,
  -isolatedGenJets,
  -generatorJetsMatch,
  -calorimeterJetsMatch,
  zToMuMu

}

 path allEntries = {
   preselection,
   -zToMuMuMC,
   allHistos
 }

 path signalEntries = {
   preselection,
   zToMuMuMC,
   signalHistos
 }

 path backgroundEntries = {
   preselection,
   !zToMuMuMC,
   backgroundHistos
 }

path allEntries0Jet = {
  preselection,
   !moreThan0Jets&

  -zToMuMuMC,
    allHistos0Jet
}

path signalEntries0Jet = {
```

```
  preselection,
   !moreThan0Jets&
    zToMuMuMC,
   signalHistos0Jet
}

path backgroundEntries0Jet = {
  preselection,
   !moreThan0Jets&
    !zToMuMuMC,
   backgroundHistos0Jet
}


 path allEntries1Jet = {
   preselection,
   moreThan0Jets&
   !moreThan1Jets&
   -zToMuMuMC,
    allHistos1Jet
 }

 path signalEntries1Jet = {
   preselection,
   moreThan0Jets&
   !moreThan1Jets&
   zToMuMuMC,
   signalHistos1Jet
 }

 path backgroundEntries1Jet = {
   preselection,
   moreThan0Jets&
   !moreThan1Jets&
   !zToMuMuMC,
   backgroundHistos1Jet
 }

path allEntries2Jets = {
   preselection,
   moreThan1Jets&
```

```
   !moreThan2Jets&
   -zToMuMuMC,
   allHistos2Jets
 }

 path signalEntries2Jets = {
   preselection,
   moreThan1Jets&
   !moreThan2Jets&
   zToMuMuMC,
   signalHistos2Jets
 }

 path backgroundEntries2Jets = {
   preselection,
   moreThan1Jets&
   !moreThan2Jets&
   !zToMuMuMC,
   backgroundHistos2Jets
 }

path allEntries3Jets = {
   preselection,
   moreThan2Jets&
   !moreThan3Jets&
   -zToMuMuMC,
   allHistos3Jets
 }

 path signalEntries3Jets = {
   preselection,
   moreThan2Jets&
   !moreThan3Jets&
   zToMuMuMC,
   signalHistos3Jets
 }

 path backgroundEntries3Jets = {
   preselection,
   moreThan2Jets&
   !moreThan3Jets&
```

```
   !zToMuMuMC ,
   backgroundHistos3Jets
 }

path allEntries4Jets = {
   preselection,
   moreThan3Jets&
   !moreThan4Jets&
   -zToMuMuMC,
   allHistos4Jets
 }

 path signalEntries4Jets = {
   preselection,
   moreThan3Jets&
   !moreThan4Jets&
   zToMuMuMC,
   signalHistos4Jets
 }

 path backgroundEntries4Jets = {
   preselection,
   moreThan3Jets&
   !moreThan4Jets&
   !zToMuMuMC ,
   backgroundHistos4Jets
 }

path allEntries5Jets = {
   preselection,
   moreThan4Jets&
   !moreThan5Jets&
   -zToMuMuMC,
   allHistos5Jets
 }

 path signalEntries5Jets = {
   preselection,
   moreThan4Jets&
   !moreThan5Jets&
   zToMuMuMC,
```

```
   signalHistos5Jets
 }

 path backgroundEntries5Jets = {
   preselection,
   moreThan4Jets&
   !moreThan5Jets&
   !zToMuMuMC,
   backgroundHistos5Jets
 }

path allEntriesMoreThan5Jets = {
   preselection,
   moreThan5Jets&
   -zToMuMuMC,
   allHistosMoreThan5Jets
 }

 path signalEntriesMoreThan5Jets = {
   preselection,
   moreThan5Jets&
   zToMuMuMC,
   signalHistosMoreThan5Jets
 }

 path backgroundEntriesMoreThan5Jets = {
   preselection,
   moreThan5Jets&
   !zToMuMuMC,
   backgroundHistosMoreThan5Jets
 }

}


# endpath o ={ out  }
}
```

Appendix B

Analysis modules

Some of the analysis modules used in the analysis have been developed specifically in the work of thesis. Those modules are reported here:

This module realizes the histograms for

```
#include "FWCore/Framework/interface/EDAnalyzer.h"
#include "FWCore/ParameterSet/interface/InputTag.h"
#include "DataFormats/Common/interface/Handle.h"
#include "FWCore/Framework/interface/Event.h"
#include "FWCore/ParameterSet/interface/ParameterSet.h"
#include "FWCore/ServiceRegistry/interface/Service.h"
#include "PhysicsTools/UtilAlgos/interface/TFileService.h"
#include "SimGeneral/HepPDTRecord/interface/PdtEntry.h"
#include "TH1.h"
#include "TH2.h"
#include "TLorentzVector.h"
#include "DataFormats/JetReco/interface/GenJet.h"
#include "DataFormats/JetReco/interface/CaloJet.h"
#include "DataFormats/JetReco/interface/CaloJetCollection.h"
#include "DataFormats/HepMCCandidate/interface/GenParticle.h"
#include "DataFormats/Candidate/interface/CompositeCandidate.h"
#include "DataFormats/MuonReco/interface/Muon.h"
#include "DataFormats/MuonReco/interface/MuonFwd.h"
#include "PhysicsTools/CandUtils/interface/AddFourMomenta.h"
#include "DataFormats/Math/interface/LorentzVector.h"
#include <iostream>
```

```
using namespace edm;
using namespace reco;
using namespace std;
using namespace math;

class zMuMuJetsHistogrammer : public EDAnalyzer {
  typedef vector<GenJet> GenJetCollection;
public:
 explicit zMuMuJetsHistogrammer( const ParameterSet & );
private:
  void analyze( const Event& , const EventSetup& );
  InputTag partons_, genJets_, caloJets_ ,
  z_ , muons_, zMC_,  matchedCaloJets_, matchedGenJets_ ;
   bool hasGlobalWeight_;
  InputTag csa07weight_;

  TH1D *partonsPt, *partonsEta, *partonsEnergy,
   *partonsPhi, *partonsId,  *partonsNumber , *partonsTotalPt ,
    *partonsTotalEnergy;
  TH1D *genJetsPt, *genJetsEta,
   *genJetsEnergy, *genJetsPhi, *genJetsTotalPt,
  *genJetsTotalEnergy, *genJetsNumber, *genJetsTotalPhi;
  TH1D *matchedGenJetsPt,
  *matchedGenJetsEta, *matchedGenJetsEnergy, *matchedGenJetsPhi,
   *matchedGenJetsTotalPt, *matchedGenJetsTotalEnergy,
   *matchedGenJetsNumber;
  TH1D *caloJetsPt, *caloJetsEta, *caloJetsEnergy,
  *caloJetsPhi, *caloJetsTotalPt, *caloJetsTotalEnergy,
   *caloJetsNumber, *caloJetsTotalPhi;
  TH1D *matchedCaloJetsPt, *matchedCaloJetsEta,
   *matchedCaloJetsEnergy, *matchedCaloJetsPhi,
    *matchedCaloJetsTotalPt, *matchedCaloJetsTotalEnergy,
    *matchedCaloJetsNumber;
  TH1D *muonsPt, *muonsEta, *muonsEnergy, *muonsPhi, *muonsMass ;
  TH1D *totalMuonsPt, *totalMuonsEta, *totalMuonsEnergy,
  *totalMuonsPhi, *totalMuonsMass;
  TH1D *zPt, *zEta, *zEnergy, *zPhi, *zMass, *zY;
  TH1D *zMCPt, *zMCEta, *zMCEnergy, *zMCPhi, *zMCMass, *zMCY;
  TH1D *caloJetsPhiMinusMuonsPhi,*genJetsPhiMinusMuonsPhi,
   *partonsPhiMinsuZPhi;
```

```
  TH2D *leadingPartonsVSCaloJets,
   *leadingPartonsVSGenJets,* genJetsVSCaloJets;



};

zMuMuJetsHistogrammer::zMuMuJetsHistogrammer(const ParameterSet & cfg)
{

  hasGlobalWeight_ = cfg.getParameter<bool>("hasglobalweight");
  if(hasGlobalWeight_==false)csa07weight_ =
  cfg.getParameter<InputTag>("weight");

  partons_=cfg.getParameter<InputTag>("partons");
  genJets_=cfg.getParameter<InputTag>("genJets");
  caloJets_=cfg.getParameter<InputTag>("caloJets");
  muons_=cfg.getParameter<InputTag>("muons");
  zMC_=cfg.getParameter<InputTag>("zMC");
  z_=cfg.getParameter<InputTag>("z");
  matchedCaloJets_=cfg.getParameter<InputTag>("matchedCaloJets");
  matchedGenJets_=cfg.getParameter<InputTag>("matchedGenJets");

  Service<TFileService> fs;

  genJetsPt = fs->make<TH1D>("genJetsPt","genJetsPt",100,0,400);
  genJetsEta = fs->make<TH1D>("genJetsEta","genJetsEta",100,-3,3);
  genJetsEnergy =
  fs->make<TH1D>("genJetsEnergy","genJetsEnergy",100,0,500);
  genJetsPhi =  fs->make<TH1D>("genJetsPhi","genJetsPhi",100,0,7);

  genJetsTotalPt =
  fs->make<TH1D>("genJetsTotalPt","genJetsTotalPt",100,0,400);
  genJetsTotalEnergy =
  fs->make<TH1D>("genJetsTotalEnergy","genJetsTotalEnergy",100,0,500);
  genJetsNumber =
  fs->make<TH1D>("genJetsNumber","genJetsNumber",10,0,10);
    genJetsTotalPhi =
  fs->make<TH1D>("genJetsTotalPhi","genJetsTotalPhi",100,0,7);
```

```
matchedGenJetsPt =
fs->make<TH1D>("matchedGenJetsPt","matchedGenJetsPt",100,0,400);
matchedGenJetsEta =
fs->make<TH1D>("matchedGenJetsEta","matchedGenJetsEta",100,-3,3);
matchedGenJetsEnergy =
fs->make<TH1D>("matchedGenJetsEnergy","matchedGenJetsEnergy",100,0,500);
matchedGenJetsPhi =
fs->make<TH1D>("matchedGenJetsPhi","matchedGenJetsPhi",100,0,7);

matchedGenJetsTotalPt =
fs->make<TH1D>("matchedGenJetsTotalPt","matchedGenJetsTotalPt",100,0,500);
matchedGenJetsTotalEnergy =
 fs->make<TH1D>("matchedGenJetsTotalEnergy",
"matchedGenJetsTotalEnergy",100,0,500);
matchedGenJetsNumber =
fs->make<TH1D>("matchedGenJetsNumber","matchedGenJetsNumber",10,0,10);

caloJetsPt =
fs->make<TH1D>("caloJetsPt","caloJetsPt",100,0,400);
caloJetsEta =
fs->make<TH1D>("caloJetsEta","caloJetsEta",100,-3,3);
caloJetsEnergy =
fs->make<TH1D>("caloJetsEnergy","caloJetsEnergy",100,0,500);
caloJetsPhi =
fs->make<TH1D>("caloJetsPhi","caloJetsPhi",100,0,7);

caloJetsTotalPt =
fs->make<TH1D>("caloJetsTotalPt","caloJetsTotalPt",100,0,400);
caloJetsTotalEnergy =
fs->make<TH1D>("caloJetsTotalEnergy","caloJetsTotalEnergy",100,0,500);
caloJetsNumber =
fs->make<TH1D>("caloJetsNumber","caloJetsNumber",10,0,10);
caloJetsTotalPhi =
fs->make<TH1D>("caloJetsTotalPhi","caloJetsTotalPhi",100,0,7);

matchedCaloJetsPt =
fs->make<TH1D>("matchedCaloJetsPt","matchedCaloJetsPt",100,0,400);
matchedCaloJetsEta =
fs->make<TH1D>("matchedCaloJetsEta","matchedCaloJetsEta",100,-3,3);
matchedCaloJetsEnergy =
fs->make<TH1D>("matchedCaloJetsEnergy","matchedCaloJetsEnergy",100,0,500);
```

```
matchedCaloJetsPhi =
fs->make<TH1D>("matchedCaloJetsPhi","matchedCaloJetsPhi",100,0,7);

matchedCaloJetsTotalPt =
fs->make<TH1D>("matchedCaloJetsTotalPt",
"matchedCaloJetsTotalPt",100,0,400);
matchedCaloJetsTotalEnergy =
fs->make<TH1D>("matchedCaloJetsTotalEnergy",
"matchedCaloJetsTotalEnergy",100,0,500);
matchedCaloJetsNumber =
fs->make<TH1D>("matchedCaloJetsNumber","matchedCaloJetsNumber",10,0,10);

partonsPt = fs->make<TH1D>("partonsPt","partonsPt",100,0,400);
partonsEta = fs->make<TH1D>("partonsEta","partonsEta",100,-3,3);
partonsEnergy = fs->make<TH1D>("partonsEnergy","partonsEnergy",100,0,500);
partonsPhi = fs->make<TH1D>("partonsPhi","partonsPhi",100,0,7);
partonsId = fs->make<TH1D>("partonsId","partonsId",35,-10,25);

partonsTotalPt =
fs->make<TH1D>("partonsTotalPt","partonsTotalPt",100,0,400);
partonsTotalEnergy =
 fs->make<TH1D>("partonsTotalEnergy","partonsTotalEnergy",100,0,500);
partonsNumber = fs->make<TH1D>("partonsNumber","partonsNumber",10,0,10);

muonsPt = fs->make<TH1D>("muonsPt","muonsPt",100,0,400);
muonsEta = fs->make<TH1D>("muonsEta","muonsEta",100,-3,3);
muonsEnergy = fs->make<TH1D>("muonsEnergy","muonsEnergy",100,0,500);
muonsPhi = fs->make<TH1D>("muonsPhi","muonsPhi",100,0,7);

totalMuonsPt = fs->make<TH1D>("totalMuonsPt","totalMuonsPt",100,0,400);
totalMuonsEta = fs->make<TH1D>("totalMuonsEta","totalMuonsEta",100,-3,3);
totalMuonsEnergy =
fs->make<TH1D>("totalMuonsEnergy","totalMuonsEnergy",100,0,500);
totalMuonsPhi = fs->make<TH1D>("totalMuonsPhi","totalMuonsPhi",100,0,7);
totalMuonsMass = fs->make<TH1D>("totalMuonsMass","totalMuonsMass",100,0,150);

zMass = fs->make<TH1D>("zMass","zMass",100,0,200);
zPt = fs->make<TH1D>("zPt","zPt",100,0,400);
zEta = fs->make<TH1D>("zEta","zEta",100,-3,3);
zEnergy = fs->make<TH1D>("zEnergy","zEnergy",100,0,500);
zPhi = fs->make<TH1D>("zPhi","zPhi",100,0,7);
```

```
  zY = fs->make<TH1D>("zRapidity","zRapidity",100,-7,7);

  zMCMass = fs->make<TH1D>("zMCMass","zMCMass",100,0,200);
  zMCPt = fs->make<TH1D>("zMCPt","zMCPt",100,0,400);
  zMCEta = fs->make<TH1D>("zMCEta","zMCEta",100,-3,3);
  zMCEnergy = fs->make<TH1D>("zMCEnergy","zMCEnergy",100,0,500);
  zMCPhi = fs->make<TH1D>("zMCPhi","zMCPhi",100,0,7);
  zMCY = fs->make<TH1D>("zMCRapidity","zMCRapidity",300,-7,7);



  leadingPartonsVSCaloJets =
  fs->make<TH2D>("leadingPartonsVSCaloJets",
  "leadingPartonsVSCaloJets",10,0,10,10,0,10);
  leadingPartonsVSGenJets =
   fs->make<TH2D>("leadingPartonsVSGenJets",
   "leadingPartonsVSGenJets",10,0,10,10,0,10);
  genJetsVSCaloJets=
  fs->make<TH2D>("genJetsVSCaloJets","genJetsVSCaloJets",10,0,10,10,0,10);

  }

void zMuMuJetsHistogrammer::analyze( const Event& evt, const EventSetup& evtstp)
{


  Handle<View<Candidate> > partons ;
  evt.getByLabel(partons_,partons);
  Handle< View<Candidate> > caloJets ;
  evt.getByLabel(caloJets_,caloJets);
  Handle< View<Candidate> > matchedCaloJets ;
  evt.getByLabel(matchedCaloJets_,matchedCaloJets);
  Handle< View<Candidate> > matchedGenJets ;
  evt.getByLabel(matchedGenJets_,matchedGenJets);
  Handle<View<Candidate> > genJets ;
  evt.getByLabel(genJets_,genJets);
  Handle<View<Candidate> > muons ;
  evt.getByLabel(muons_,muons);
  Handle<View<Candidate> > z ;
  evt.getByLabel(z_,z);
  Handle<View<Candidate> > zMC ;
```

```
  evt.getByLabel(zMC_,zMC);

  XYZTLorentzVector sum(0,0,0,0) ;

  double weight=1;
  if(hasGlobalWeight_==false){

    Handle<  double   > csaweight  ;
    evt.getByLabel(csa07weight_,csaweight);
    weight = (*csaweight);

}



  size_t nPartons = partons->size();
  size_t nCaloJets = caloJets->size();
  size_t nGenJets = genJets->size();

  /*if( n1 > 1  ){
    cout<<"  numero partoni  "<<n1<<endl;
    cout<<"  numero caloJets  "<<n2<<endl;
    cout<<"  numero genJets  "<<n3<<endl;
    }*/

  for(size_t i = 0; i < nPartons; i++ ){
    const Candidate & p = (*partons)[i];
    sum = sum + p.p4();
    partonsEta->Fill(p.eta(),weight);
    partonsPhi->Fill(p.phi(),weight);
    partonsEnergy->Fill(p.energy(),weight);
    partonsPt->Fill(p.pt(),weight);
    partonsId->Fill(p.pdgId(),weight);
  }

  partonsTotalPt->Fill(sum.pt(),weight);
  partonsTotalEnergy->Fill(sum.energy(),weight);
  partonsNumber->Fill(nPartons,weight);

  sum = XYZTLorentzVector(0,0,0,0);
  for(size_t i = 0; i < nGenJets; i++ ){
```

```
    const Candidate & p = (*genJets)[i];
    sum = sum + p.p4();
    genJetsPhi->Fill(p.phi(),weight);
    genJetsEta->Fill(p.eta(),weight);
    genJetsEnergy->Fill(p.energy(),weight);
    genJetsPt->Fill(p.pt(),weight);
  }
  genJetsTotalEnergy->Fill(sum.energy(),weight);
  genJetsTotalPt->Fill(sum.pt(),weight);
  genJetsNumber->Fill(nGenJets,weight);
  genJetsTotalPhi->Fill(sum.phi(),weight);

  sum = XYZTLorentzVector(0,0,0,0);
  size_t maxIndex = 0;
  for(size_t i = 0; i < nCaloJets; i++ ){
    const Candidate & p = (*caloJets)[i];
    sum = sum + p.p4();
    if(p.energy() > ((*caloJets)[maxIndex]).energy()) maxIndex = i;
    caloJetsEnergy->Fill(p.energy(),weight);
    caloJetsPt->Fill(p.pt(),weight);
    caloJetsEta->Fill(p.eta(),weight);
    caloJetsPhi->Fill( p.phi(),weight);
  }
  caloJetsTotalEnergy->Fill(sum.energy(),weight);
  caloJetsTotalPt->Fill(sum.pt(),weight);
  caloJetsNumber->Fill(nCaloJets, weight);
  caloJetsTotalPhi->Fill(sum.phi(),weight);

  sum = XYZTLorentzVector(0,0,0,0);
  for(size_t i = 0; i < matchedCaloJets->size(); i++ ){
    const Candidate & p = (*matchedCaloJets)[i];
    sum = sum + p.p4();
    matchedCaloJetsEnergy->Fill(p.energy(),weight);
    matchedCaloJetsPt->Fill(p.pt(),weight);
    matchedCaloJetsEta->Fill(p.eta(), weight);
    matchedCaloJetsPhi->Fill( p.phi(), weight);
  }
  matchedCaloJetsTotalEnergy->Fill(sum.energy(),weight);
  matchedCaloJetsTotalPt->Fill(sum.pt(),weight);
  matchedCaloJetsNumber->Fill(matchedCaloJets->size(),weight);
```

```
sum = XYZTLorentzVector(0,0,0,0);
for(size_t i = 0; i < matchedGenJets->size(); i++ ){
  const Candidate & p = (*matchedGenJets)[i];
  sum = sum + p.p4();
  matchedGenJetsEnergy->Fill(p.energy(),weight);
  matchedGenJetsPt->Fill(p.pt(),weight);
  matchedGenJetsEta->Fill(p.eta(),weight);
  matchedGenJetsPhi->Fill( p.phi(),weight);
}
matchedGenJetsTotalEnergy->Fill(sum.energy(),weight);
matchedGenJetsTotalPt->Fill(sum.pt(),weight);
matchedGenJetsNumber->Fill(matchedGenJets->size(),weight);

sum = XYZTLorentzVector(0,0,0,0);
for(size_t i = 0; i < muons->size(); i++ ){
  const Candidate & p = (*muons)[i];
  sum = sum + p.p4();
  muonsPt->Fill(p.pt(),weight);
  muonsEta->Fill(p.eta(),weight);
  muonsEta->Fill(p.eta(),weight);
  muonsPhi->Fill(p.phi(),weight);
}
totalMuonsPt->Fill(sum.pt(),weight);
totalMuonsMass->Fill(sum.mass(),weight);
totalMuonsEta->Fill(sum.eta(),weight);
totalMuonsPhi->Fill(sum.phi(),weight);


sum = XYZTLorentzVector(0,0,0,0);
for(size_t i = 0; i < zMC->size(); i++ ){
  const Candidate & p = (*zMC)[i];
  sum = sum + p.p4();
  zMCMass->Fill(p.mass(),weight);
  zMCPt->Fill(p.pt(),weight);
  zMCY->Fill(p.y(),weight);
  zMCPhi->Fill(p.phi(),weight);
  zMCPhi->Fill(p.eta(),weight);
}

for(size_t i = 0; i < z->size(); i++ ){
  const Candidate & p = (*z)[i];
```

```
   sum = sum + p.p4();
   zMass->Fill(p.mass(),weight);
   zPt->Fill(p.pt(),weight);
   zY->Fill(p.y(),weight);
   zPhi->Fill(p.phi(),weight);
   zEta->Fill(p.eta(),weight);
 }



 leadingPartonsVSCaloJets->Fill(nPartons,nCaloJets);
 leadingPartonsVSGenJets->Fill(nPartons,nGenJets);
 genJetsVSCaloJets->Fill(nGenJets,nCaloJets);

}







#include "FWCore/Framework/interface/MakerMacros.h"
DEFINE_FWK_MODULE(zMuMuJetsHistogrammer);
```

Module for parton selection:

```
//This module selects the GenParticles of status 3 that are qwarks and gluons
//wich have no status 3 daughters.
//and produces a vector of reco::GenParticle
//
//
//
//
//Author: Alberto Orso Maria Iorio



#include "FWCore/Framework/interface/EDProducer.h"
#include "FWCore/ParameterSet/interface/InputTag.h"
```

```
#include "FWCore/ParameterSet/interface/ParameterSet.h"
#include "DataFormats/HepMCCandidate/interface/GenParticle.h"
#include "FWCore/Framework/interface/Event.h"

using namespace edm;
using namespace reco;
using namespace std;

class ZMuMuJetsLeadingPartonProducer : public EDProducer {
public:
  ZMuMuJetsLeadingPartonProducer(const ParameterSet&);
private:
  void produce(Event&, const EventSetup&);
  InputTag src_;
};

ZMuMuJetsLeadingPartonProducer::ZMuMuJetsLeadingPartonProducer(const ParameterSe
  src_(cfg.getParameter<InputTag>("src")) {
  produces<GenParticleCollection>().setBranchAlias("leadingPartons");
}

void ZMuMuJetsLeadingPartonProducer::produce(Event& evt, const EventSetup&) {
  Handle<GenParticleCollection> genParticles;
  evt.getByLabel(src_ ,genParticles);
  auto_ptr<GenParticleCollection> partons( new GenParticleCollection );
  for(size_t i = 0; i < genParticles->size(); i++ ) {
    const GenParticle & p = (*genParticles)[i];
    int status = p.status();
    if(status  < 3) continue;
    int id = abs(p.pdgId());
    if(id > 6 && id != 21 ) continue;
    size_t nDaughters = p.numberOfDaughters();
    //if(nDaughters < 1) continue;
    //size_t nMothers = p.numberOfMothers();
    //if(nMothers < 1) continue;
    bool ok1 = true;
    bool ok2 = true;
    for (size_t ds = 0; ds < nDaughters; ds++) {
      if(p.daughter(ds)->status()==3) {
ok1 = false; break;
      }
```

```
      //size_t nDaughterDaughters = p.daughter(ds)->numberOfDaughters();
      //      for(size_t k = 0; k < nDaughterDaughters && ok2 == false; k++){
      // int dauId = p.daughter(ds)->daughter(k)->pdgId();
      // if(dauId == 92) ok2 = true;
      //}
    }
    if (ok1 && ok2) partons->push_back((*genParticles)[i]);
    // if (p.pdgId()==23) cout <<"  c'e' una zeta   "<<endl;

  }
  evt.put(partons);
}

#include "FWCore/Framework/interface/MakerMacros.h"
DEFINE_FWK_MODULE(ZMuMuJetsLeadingPartonProducer);
```

This module is realized to isolate jets from muons and is based on an angular algorithm:

```
//This module isolates the jets collection objects from the muon collection obje
//requiring that the distance in the eta-phi plane is greater than deltar
//producing a reco::CandidateBaseRefVector
//
//
//(It actually works for any container of candidates because of the CandidateVie
//
//Author: Alberto Orso Maria Iorio

#include "DataFormats/HepMCCandidate/interface/GenParticle.h"
#include "DataFormats/JetReco/interface/CaloJet.h"
#include "DataFormats/JetReco/interface/CaloJetCollection.h"
#include "FWCore/Framework/interface/EDProducer.h"
#include "FWCore/ParameterSet/interface/InputTag.h"
#include "FWCore/Framework/interface/Event.h"
#include "PhysicsTools/Utilities/interface/deltaR.h"
#include "FWCore/ParameterSet/interface/ParameterSet.h"

using namespace edm;
using namespace reco;
using namespace std;
```

```
class ZMuMuJetsIsolatedJetsProducer : public EDProducer{
public:
  ZMuMuJetsIsolatedJetsProducer(const ParameterSet & cfg);
  void produce(Event & evt,const EventSetup & evtsetup);
private:
  InputTag jets_, muons_;
  string name_;
 double deltar_;
};

ZMuMuJetsIsolatedJetsProducer::ZMuMuJetsIsolatedJetsProducer(const ParameterSet
  jets_ = cfg.getParameter<InputTag  >("jets");
  muons_ = cfg.getParameter<InputTag  >("muons");
  deltar_ = cfg.getParameter<double  >("deltar");
  name_ = cfg.getParameter<string>("name");
 produces< CandidateBaseRefVector  >().setBranchAlias(name_);

}


void ZMuMuJetsIsolatedJetsProducer::produce(Event & evt,const EventSetup& evtset
  Handle<View<Candidate >  > jets;
  evt.getByLabel(jets_, jets);
  Handle<View<Candidate >  > muons;
  evt.getByLabel(muons_, muons);

  double deltamin=deltar_;

   auto_ptr< CandidateBaseRefVector  > IsolatedJets( new CandidateBaseRefVector


  for(size_t i = 0 ; i < jets->size() ; i++ ){
    const Candidate & jet = (*jets)[i];
    bool isolated = true;
    for(size_t k = 0; k < muons->size(); k++){
      const Candidate & mu = (*muons)[k];
      double d = deltaR(mu, jet);
      if(d<deltamin)
{isolated=false;
break;}
```

```
    }
    if(isolated == true){
       IsolatedJets->push_back(CandidateBaseRef(jets,i));
     }
  }
  evt.put(IsolatedJets);
}


#include "FWCore/Framework/interface/MakerMacros.h"
DEFINE_FWK_MODULE(ZMuMuJetsIsolatedJetsProducer);
```

Acknowledgements

I would like to thank all the people that accompanied me through the journey that led to this work. First of all I want to thank professor Sciacca for the great chance he granted me, and for all the teachings and advices he gave me during those years which boosted even more my love for physics. I want to thank dr. Luca Lista who introduced me to the world of CMS for patiently guiding me through the challenges I had to face during the work of thesis, and for all the support he gave me in this endeavor. I want to also give a special thank to dr. Francesco Fabozzi for the help he provided me during the most crucial times of the work with great humanity and competence. I thank dr. Pierluigi Paolucci and dr. Davide Piccolo who warmly welcomed me in the CMS Napoli group. I want to thank professor Chiefari who watched over me with great professionalism and care. Finally, I want to thank all the people, my friends and dear ones, that have been close to me and that sustained me in such an important moment of my life.

Bibliography

[1] Weyl,Zeitshrift Physik,56 (1929)

[2] S.Glashow,Nucl.Phys.22 (1961) 579.

[3] A.Salam, Elementary particle Theory, Ed. N. Svarholm (1968).

[4] S.Weinberg, Phys. Rev. Lett. 19 (1967) 1264.

[5] P.Higgs, Phys. Rev. Lett. 13, 508 (1964)

[6] F.Halzen-A.D.Martin, Quarks and Leptons, an introductory course in modern particle physics, J.Wiley Sons (1968).

[7] I.J.R. Aitchison, A.J.G. Hey, Gauge Theory in Particle Physics (Vol 1), Institute of Physics Publishing, Bristol and Philadelphia.

[8] I.J.R. Aitchison, A.J.G. Hey, Gauge Theory in Particle Physics (Vol 2), Institute of Physics Publishing, Bristol and Philadelphia.

[9] . Wiley and Sons (1984)

[10] .H. Perkins, Introduction for High Energy Physics, IV ed (2000)

[11] The UA1 Collaboration, G. Arnison et al., Phys. Lett. B122 (1983). The UA1 Collaboration, G. Arnison et al., Phys. Lett. B126 (1983).

[12] D.A. Bromley, Gauge Theory of Weak Interactions. Springer. (2000)

[13] N. Cabibbo, Phys.Rev.Lett. 10,531 (1963)

[14] M. Kobayashi and Maskawa, Prog. Theor Phys. 49,652(1973)

[15] P.W. Higgs, Phys. Lett. 12,132 (1968)

[16] S. Dawson, the Standard Model intermediate Higgs Boson, in the prospective on Higgs Physics II, Ed. Gordon L.Kane, World Scientific (1997)

[17] D. J. Gross, F. Wilczek, Ultraviolet behavior of non-abeilan gauge theoreies, Phys. Rev. Letters, 30 1343-1346 (1973)

[18] H. D. Politzer, Reliable perturbative results for strong interactions, Phys. Rev. Letters 30 1346-1349 (1973)

[19] S.D. Drell and T.M. Yan, Phys. Rev. Lett. 25 (1970) 316; Ann. Phys. (N.Y.) 66 (1971) 578

[20] Greiner, Walter; Schfer, Andreas (1994). Quantum Chromodynamics. Springer. ISBN 0-387-57103-5.

[21] The Large Hadron Collider, homepage: http://lhc.web.cern.ch/lhc/

[22] CERN, http://www.cern.ch/

[23] LEP Experiments, http://greybook.cern.ch/

[24] The Compact Muon Solenoid, homepage: http://cms.cern.ch/

[25] A Toroidal LHC Apparatus, homepage: http://atlas.ch/

[26] A Large Ion Collider Experiment, homepage: http://aliceinfo.cern.ch/

[27] The Large Hadron Collider beauty experiment, homepage: http://lhcb.web.cern.ch/lhcb/

[28] CMS Collaboration, "The Compact Muon Solenoid, Technical Proposal", CERN/LHCC 94-38 LHCC/P1

[29] CMS Collaboration, CMS Physics Technical Design Report, Volum 1: Detector Performance and Software, CERN/LHCC, IOP Publishing, Febbraio 2006.

[30] CMS Collaboration, CMS Physics Technical Design Report, Volum 2: Physics Performance, CERN/LHCC, IOP Publishing, Giugno 2007.

[31] CMS Collaboration, "CMS Tracker Project, Technical Design Report", CERN/LHCC 98-6 CMS TDR 5

[32] CMS Collaboration, "Addendum to the CMS Tracker Project, Technical Design Report", CERN/LHCC 2000-016 CMS TDR 5 Addendum 1

[33] CMS Collaboration, "The Electromagnetic Calorimeter Project, Technical Design Report", CERN/LHCC 97-33 CMS TDR 4

[34] CMS Collaboration, "The Hadron Calorimeter Project, Technical Design Report", CERN/LHCC 97-31 CMS TDR 2

[35] CMS Collaboration, "The Muon Project" TDR CERN/LHCC 98-06 (1998)

[36] CMS Collaboration, "The Trigger and Data Acquisition Project Volume I - The Level-1 Trigger, Technical Design Report", CERN/LHCC 2000-016 CMS TDR 6.1

[37] CMS Collaboration, "The TriDAS Project Volume II - Data Acquisition and High- Level Trigger, Technical Design Report", CERN/LHCC 2000-016 CMS TDR 6.2

[38] .Giannotti, Collider Physics: LHC, CERN-open-2000-293

[39] R.N.Cahn e S.Dawson, Phys. Lett. B136 (1984) 196.

[40] S.Abdullin et al., Light Higgs Boson Signal at LHC in the Reactions $pp\gamma\gamma + jet$ and $pp \rightarrow \gamma\gamma +$ lepton, Phys. Lett., B431 (1998).

[41] Aldaya M., Arce P.Caballero J. de La Cruz B., Garcia-Abia P., Hernandez J.M., Josa M. and Ruiz E. 2006 Discovery potential and search strategy for the Standard Model Higgs boson in the $H \rightarrow ZZ \rightarrow 4\mu$ decay channel using a mass-independent analysis CMS Note2006/106.

[42] M.Lindner, Z. Phys C 31 295 (1986); G. Altarelli, Proc of LHC Workshop, Aachen, ed by G. Jarlskog and D. Rein (1990) CERN 90-10

[43] T. Hambye and K. Riesselmann, Phys. Rev. D 55 7255 (1997)

[44] Fermi National Accelerator Laboratory, http://www-bdnew.fnal.gov/tevatron/

[45] Search for the Standard Model Higgs Boson at LEP CERN-EP-2003-011

[46] F.A. Berends et al., Z Physics at LEP1, CERN Report 89-08 (1989)

[47] Tevatron Electroweak Working Group, Combination of CDF and D0 Resutls on the Top-Quark Mass, hep-ex/0507091

[48] I.J.R. Aitchison, "Supersymmetry and the MSSM: An Elementary Introduction", hepph/ 0505105; M. Drees, "Introduction to Supersymmetry", hep-ph/9611409; S.P. Martin, "A Supersymmetry Primer", hep-ph/9709356

[49] Ramdall L. e Sundrum R. 1999 A large mass hierarcy from a small extra dimension Phys. Rev. Lett. 83 3370-3373

[50] Leike A.1999 The phenomenology of extra neutral gauge bosons, Phys. Rept. 317 143-250

[51] Cvetic M. e Langacker P. 1996 New gauge bosons from string models, Mod.Phys.Lett. A 11 1247-1262

[52] Hill C.T. e Simmons E.H. 2003 Strong dynamics and electroweak simmetry breaking, Phys.Rept. 381 235-402

[53] Han T., Logan H., McElrath B. e Wang L-T 2003 Phenomenology of the little Higgs Model, Phys. Rev. D 67 095004

[54] Lane K.D. 2000 Technicolor 2000, Preprint hep-ph/0007304

[55] PYTHIA home page: http://www.thep.lu.se/ torbjorn/Pythia.html

[56] GEANT4 home page: http://wwwasd.web.cern.ch/wwwasd/geant4/geant4.html

[57] SHERPA home page: http://www.sherpa-mc.de/

[58] HERWIG home page: http://hepwww.rl.ac.uk/theory/seymour/herwig/

[59] ALPGEN home page: http://mlm.home.cern.ch/mlm/alpgen/

[60] CMSSW home page: http://cmssw.cvs.cern.ch/cgi-bin/cmssw.cgi/CMSSW/

[61] S.Baffioni et al., Electron reconstruction in CMS

[62] R. FrÄuhwirth, Application of Kalman Filtering to Track and Vertex Fitting, Nucl. Instrum. and Methods A262 (1987) 444

[63] Muon pog home page: https://twiki.cern.ch/twiki/bin/view/CMS/MuonPOG

[64] S.V. Chekanov, Jet algorithms: A mini review, arXiv:hep-ph/0211298

[65] G.C. Blazey et al., Run II jet physics, arXiv:hep-ex/0005012

[66] J.M. Butterworth, J.P. Couchman, B.E. Cox e B.M.Waugh, KtJet: A C++ implementation of the K(T) clustering algorithm, Comput. Physi. Commun. 153 (2003) 85-96

[67] S.D. Ellis and D.E.Soper, Successive combination jet algorithm fo hadron collisions, Phys. Rev. D48 (1993) 31603166, arXiv:hep-ph/9305266.doi:10.1103/PhysRevD.48.3160

[68] . Pierini, M.Spiropulu, Study of V + jets in bins of boson PT and jet multiplicity for 2007 1 $fb^{-}1$ Monte Carlo production at CMS CMS note IN2007_031.

[69] CSA07 home page: https://twiki.cern.ch/twiki/bin/view/CMS/CSA07

[70] .L. Mangano, M. Moretti and R. Pittau, Nucl. Phys. B632 (2002) 343, hep-ph/0108069

[71] ROOT home page: http://root.cern.ch/

[72] An Introduction to Error Analysis, The Study of Uncertainties in Physical Measurements, Second Edition (2000)

[73] PDG (Particle Data Group): http://pdg.lbl.gov.